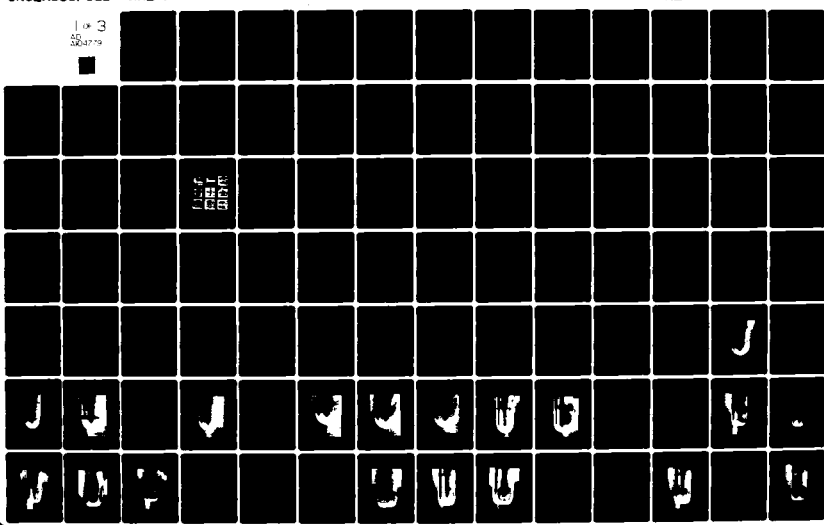


AD-A104 779

PENNSYLVANIA STATE UNIV UNIVERSITY PARK APPLIED RESE--ETC F/G 20/4
OBSERVATIONS OF THE EFFECTS OF BOUNDARY LAYER AND NUCLEI ON CAV--ETC(U)
FEB 81 J A CARROLL N00024-79-C-6043
ARL/PSU/TM-81-60 NL

UNCLASSIFIED

1 of 3
AD-A104 779



AD A104779

LEVEL

6

OBSERVATIONS OF THE EFFECTS OF BOUNDARY LAYER
AND NUCLEI ON CAVITATION OF AXISYMMETRIC BODIES .

(10) J. A. Carroll

(11) 13 Feb 81

(12) 13 Feb 81

(14) FRL/PSU/711-

Technical Memorandum

File No. 81-60

13 February 1981

Contract No. N00024-79-C-6043

Copy No. 17



The Pennsylvania State University
APPLIED RESEARCH LABORATORY
Post Office Box 30
State College, PA 16801

Approved for Public Release
Distribution Unlimited

NAVY DEPARTMENT

NAVAL SEA SYSTEMS COMMAND

DTIC FILE COPY

391001

81

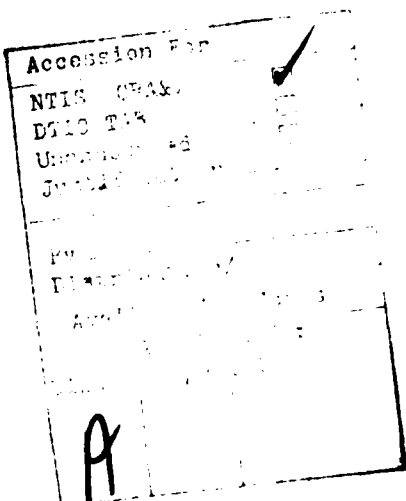
71

SECURITY CLASSIFICATION OF THIS PAGE (When Data Entered)

REPORT DOCUMENTATION PAGE		READ INSTRUCTIONS BEFORE COMPLETING FORM
1. REPORT NUMBER 81-60	2. GOVT ACCESSION NO. <i>AD-A104 4779</i>	3. RECIPIENT'S CATALOG NUMBER
4. TITLE (and Subtitle) OBSERVATIONS OF THE EFFECTS OF BOUNDARY LAYER AND NUCLEI ON CAVITATION OF AXISYMMETRIC BODIES		5. TYPE OF REPORT & PERIOD COVERED Technical Memorandum
7. AUTHOR(s) J. A. Carroll		6. PERFORMING ORG. REPORT NUMBER
9. PERFORMING ORGANIZATION NAME AND ADDRESS Applied Research Laboratory Post Office Box 30 State College, PA 16801		10. PROGRAM ELEMENT, PROJECT, TASK AREA & WORK UNIT NUMBERS
11. CONTROLLING OFFICE NAME AND ADDRESS Naval Sea Systems Command Department of the Navy Washington, DC 20362		12. REPORT DATE 13 February 1981
14. MONITORING AGENCY NAME & ADDRESS (if different from Controlling Office)		13. NUMBER OF PAGES 218
		15. SECURITY CLASS. (of this report) UNCLASSIFIED
		15a. DECLASSIFICATION/DOWNGRADING SCHEDULE
16. DISTRIBUTION STATEMENT (of this Report) Approved for Public Release. Distribution Unlimited. Per NAVSEA - March 13, 1981.		
17. DISTRIBUTION STATEMENT (of the abstract entered in Block 20, if different from Report)		
18. SUPPLEMENTARY NOTES		
19. KEY WORDS (Continue on reverse side if necessary and identify by block number) thesis, boundary layer, nuclei, cavitation, axisymmetric		
20. ABSTRACT (Continue on reverse side if necessary and identify by block number) An investigation of limited cavitation was conducted on three different axisymmetric models. Test models included a hemispherical nose, a Schiebe nose, and a David Taylor Naval Ship Research and Development Center (DTNSRDC) nose. All models had a 2.0-in. diameter. Theoretical pressure distribution calculations and laminar boundary layer growth calculations were performed for the above models which were subsequently tested and also for a 1.5-caliber ogive nose, a 1.0-caliber ogive nose, and an International Towing Tank		

20. Conference (ITTC) nose to serve as supplementary information. The test models were chosen in accordance with their boundary layer flow characteristics. Laminar boundary layer separation was predicted to occur on the hemispherical nose for all test velocities. Calculations for the Schiebe nose indicated that laminar boundary layer separation does not occur and, therefore, this model exhibits an attached boundary layer for all velocities. Laminar separation was predicted for the DTNSRDC nose; however, this model has a relatively low critical Reynolds number. As a result, the DTNSRDC nose exhibits laminar separation at low velocities and an attached boundary layer at high velocities.

Cavitation tests were performed at two different air contents for each model. Several different types of limited cavitation were observed. A procedure of recording the cavitation tests on audio-visual recording tape for subsequent analysis was used and proved to be extremely helpful. Common characteristics were observed in the cavitation behavior of the different models for variations in free stream velocity, air content and boundary layer status. Limited cavitation data are presented along with detailed descriptions of the observed cavitation types. Photographs of the different cavitation types are also included. Additional tests were performed to obtain measured values of mean and fluctuating pressures on a 2.0-in. diameter hemispherical nose. Mean pressure measurements carried out in the region of boundary layer reattachment were supportive to the discussion of bubble-ring cavitation. Transient cavitation observed on all models appears to be closely associated with the nuclei characteristics of the testing facility. Both band and bubble-ring cavitation are controlled by the presence of laminar boundary layer separation. Characteristics of fixed-patch cavitation, as observed on the Schiebe and DTNSRDC noses, suggest that it may be controlled by surface roughness, although relatively little is known about this type of cavitation.



ABSTRACT

An investigation of limited cavitation was conducted on three different axisymmetric models. Test models included a hemispherical nose, a Schiebe nose, and a David Taylor Naval Ship Research and Development Center (DTNSRDC) nose. All models had a 2.0-in. diameter. Theoretical pressure distribution calculations and laminar boundary layer growth calculations were performed for the above models which were subsequently tested and also for a 1.5-caliber ogive nose, a 1.0-caliber ogive nose, and an International Towing Tank Conference (ITTC) nose to serve as supplementary information. The test models were chosen in accordance with their boundary layer flow characteristics. Laminar boundary layer separation was predicted to occur on the hemispherical nose for all test velocities. Calculations for the Schiebe nose indicated that laminar boundary layer separation does not occur and, therefore, this model exhibits an attached boundary layer for all velocities. Laminar separation was predicted for the DTNSRDC nose; however, this model has a relatively low critical Reynolds number. As a result, the DTNSRDC nose exhibits laminar separation at low velocities and an attached boundary layer at high velocities.

Cavitation tests were performed at two different air contents for each model. Several different types of limited cavitation were observed. A procedure of recording the cavitation tests on audio-visual recording tape for subsequent analysis was used and proved to be extremely helpful. Common characteristics were observed in the cavitation behavior of the different models for variations in free stream velocity, air content and boundary layer status.

Limited cavitation data are presented along with detailed descriptions of the observed cavitation types. Photographs of the different cavitation types are also included. Additional tests were performed to obtain measured values of mean and fluctuating pressures on a 2.0-in. diameter hemispherical nose. Mean pressure results were helpful in attempting to understand band cavitation. Fluctuating pressure measurements carried out in the region of boundary layer reattachment were supportive to the discussion of bubble-ring cavitation. Transient cavitation observed on all models appears to be closely associated with the nuclei characteristics of the testing facility. Both band and bubble-ring cavitation are controlled by the presence of laminar boundary layer separation. Characteristics of fixed-patch cavitation, as observed on the Schiebe and DTNSRDC noses, suggest that it may be controlled by surface roughness, although relatively little is known about this type of cavitation.

TABLE OF CONTENTS

	<u>Page</u>
ABSTRACT	iii
LIST OF TABLES	viii
LIST OF FIGURES	x
LIST OF SYMBOLS	xv
ACKNOWLEDGMENTS	xix
 Chapter	
1. INTRODUCTION	1
1.1 Background Information	1
1.2 Previous Investigations	5
1.3 Objectives of this Investigation	11
2. EXPERIMENTAL METHODS	14
2.1 Test Models	14
2.2 Test Facility	18
2.3 Experimental Procedure	19
3. THEORETICAL FLOW CALCULATIONS	22
4. OBSERVATIONS OF LIMITED CAVITATION ON AXISYMMETRIC MODELS	36
4.1 General Descriptions of Limited Cavitation Types	36
4.1.1 Transient cavitation	36
4.1.2 Attached cavitation	37
4.2 Presentation of Results from Cavitation Observations	43
4.2.1 Hemispherical nose	43
4.2.1.1 Transient cavitation	43
4.2.1.2 Attached cavitation	47
4.2.1.3 Effect of a boundary layer trip on cavitation characteristics	52
4.2.2 Schiebe nose	58
4.2.2.1 Transient cavitation	58
4.2.2.2 Attached cavitation	65
4.2.3 DTNSRDC nose	67
4.2.3.1 Transient cavitation	67
4.2.3.2 Attached cavitation	71
5. DISCUSSION OF CAVITATION OBSERVATIONS	77
5.1 Travelling Cavitation	77
5.1.1 Characteristics	78
5.1.2 Estimates for free stream nuclei size	79

Chapter		<u>Page</u>
5.1.3	Theoretical modelling of travelling cavitation	84
5.1.4	Travelling-bubble and travelling-patch cavitation	86
5.2	Attached Cavitation	88
5.2.1	Band cavitation	88
5.2.1.1	Characteristics of band cavitation.	90
5.2.1.2	Scaling of σ_g for band cavitation .	91
5.2.1.3	Effects of air content on band cavitation	94
5.2.1.4	Bubble-ring cavitation	94
5.2.1.5	Bubble-ring and band cavitation .	96
5.2.1.6	Occurrence of bubble-ring cavitation	98
5.2.2	Fixed-patch cavitation	101
5.2.2.1	Characteristics of fixed-patch cavitation	101
5.2.2.2	Scaling problem of fixed-patch cavitation	104
5.2.2.3	Hypothetical development of fixed-patch cavitation	106
5.2.3	Developed cavitation	109
6.	PRESENTATION AND DISCUSSION OF MEAN PRESSURE MEASUREMENTS ON A 2.0-IN. DIAMETER HEMISPHERICAL NOSE	110
6.1	Introduction	110
6.2	Experimental Setup Procedure	113
6.3	Results	117
6.4	Discussion of Results	117
7.	PRESENTATION AND DISCUSSION OF FLUCTUATING PRESSURE MEASUREMENTS IN THE REATTACHMENT REGION OF A 2.0-IN. DIAMETER HEMISPHERICAL NOSE	125
7.1	Introduction	125
7.2	Equipment and Procedure	128
7.3	Results of Fluctuating Pressure Measurements	133
7.4	Discussion	137
8.	SUMMARY, CONCLUSIONS, AND RECOMMENDATIONS FOR FUTURE STUDIES	149
8.1	Summary	149
8.2	Conclusions	152
8.3	Recommendations for Future Studies	158
REFERENCES	160
APPENDIX A.	DISCUSSION OF EXPERIMENTAL ERROR IN MEASUREMENTS	163
	Velocity Measurements	163
	Pressure Coefficients	164
	Cavitation Number	167

	<u>Page</u>
APPENDIX B. CALIBRATION PROCEDURE FOR A CAVITY-MOUNTED DYNAMIC PRESSURE TRANSDUCER	169
APPENDIX C. PROCEDURE FOR REDUCTION OF FLUCTUATING PRESSURE DATA	175
APPENDIX D. DATA TABULATIONS	179

LIST OF TABLES

<u>Table</u>		<u>Page</u>
1	Coordinates of Schiebe Nose. Taken from reference [17]	17
2	Pressure Tap Locations on a 2.0-in. Diameter Hemispherical Nose	114
3	Summary of Cavitation Observations	157
4	Douglas Neumann Pressure Distribution Model: Hemispherical Nose	180
5	Douglas Neumann Pressure Distribution Model: Schiebe Nose	182
6	Douglas Neumann Pressure Distribution Model: DTNSRDC Nose	184
7	Measured Pressure Distribution Model: 2.0-in. Diameter Hemispherical Nose $U_{\infty} = 20.0$ fps	185
8	Measured Pressure Distribution Model: 2.0-in. Diameter Hemispherical Nose $U_{\infty} = 30.0$ fps	186
9	Measured Pressure Distribution Model: 2.0-in. Diameter Hemispherical Nose $U_{\infty} = 40.0$ fps	187
10	Measured Pressure Distribution Model: 2.0-in. Diameter Hemispherical Nose $U_{\infty} = 50.0$ fps	188
11	Measured Pressure Distribution Model: 2.0-in. Diameter Hemispherical Nose $U_{\infty} = 60.0$ fps	189
12	Measured Pressure Distribution Model: 2.0-in. Diameter Hemispherical Nose $U_{\infty} = 70.0$ fps	190
13	Measured Pressure Distribution Model: 2.0-in. Diameter Hemispherical Nose With Boundary Layer Trip $U_{\infty} = 30.0$ fps	191

<u>Table</u>		<u>Page</u>
14	Measured Pressure Distribution Model: 2.0-in. Diameter Hemispherical Nose With Boundary Layer Trip $U_{\infty} = 40.0 \text{ fps}$	192
15	Limited Cavitation Data Hemispherical Nose ($\alpha = 7.8 \text{ ppm}$, Temp. = 79°F)	193
16	Limited Cavitation Data Hemispherical Nose ($\alpha = 11.0 \text{ ppm}$, Temp. = 79°F)	194
17	Limited Cavitation Data DTNSRDC Nose ($\alpha = 3.0 \text{ ppm}$, Temp. = 79°F)	195
18	Limited Cavitation Data DTNSRDC Nose ($\alpha = 8.0 \text{ ppm}$, Temp. = 79°F)	197
19	Limited Cavitation Data Schiebe Nose ($\alpha = 3.0 \text{ ppm}$, Temp. = 78°F)	199
20	Limited Cavitation Data Schiebe Nose ($\alpha = 9.0 \text{ ppm}$, Temp. = 78°F)	200

LIST OF FIGURES

<u>Figure</u>		<u>Page</u>
1	Comparison of cavitation inception results for a Swedish headform from several worldwide facilities sponsored by the International Towing Tank Conference. Taken from Figure 2 of reference [13]	8
2	Photographs of various types of cavitation observed on the ITTC nose in different testing facilities. Taken from Figure 3 of reference [13]	9
3	Geometric details of axisymmetric test models	15
4	Douglas Neumann pressure distribution for a 2.0-in. diameter hemispherical nose in a 12.0-in. diameter tunnel and in a free stream	23
5	Douglas Neumann pressure distribution for a 2.0-in. diameter Schiebe nose in a 12.0-in. diameter tunnel and in a free stream	24
6	Douglas Neumann pressure distribution for a 2.0-in. diameter DTNSRDC nose in a 12.0-in. diameter tunnel and in a free stream	25
7	Development of laminar boundary layer along a 2.0-in. diameter hemispherical nose	27
8	Development of laminar boundary layer along a 2.0-in. diameter Schiebe nose	28
9	Development of laminar boundary layer along a 2.0-in. diameter DTNSRDC nose	29
10	Douglas Neumann pressure distribution for a 2.0-in. diameter, 1.5-caliber ogive nose in a 12.0-in. diameter tunnel and in a free stream	30
11	Douglas Neumann pressure distribution for a 2.0-in. diameter, 1.0-caliber ogive nose in a 12.0-in. diameter tunnel and in a free stream	31
12	Douglas Neumann pressure distribution for a 2.0-in. diameter ITTC nose in a 12.0-in. diameter tunnel and in a free stream	32
13	Development of laminar boundary layer along a 2.0-in. diameter, 1.5-caliber ogive nose	33

<u>Figure</u>		<u>Page</u>
14	Development of laminar boundary layer along a 2.0-in. diameter, 1.0-caliber ogive nose	34
15	Development of laminar boundary layer along a 2.0-in. diameter ITTC nose	35
16	Sketch of travelling-bubble cavitation on an arbitrary axisymmetric nose	38
17	Sketch of travelling-patch cavitation on an arbitrary axisymmetric nose	39
18	Sketch of band cavitation on an arbitrary axisymmetric nose	41
19	Sketch of fixed-patch cavitation on an arbitrary axisymmetric nose	42
20	Sketch of developed cavitation on an arbitrary axisymmetric nose	43
21	Limited cavitation data versus U_∞ for various types of cavitation on a 2.0-in. diameter [∞] hemispherical nose for two values of air content	45
22	Photograph of travelling-bubble cavitation on the hemispherical nose	46
23	Photograph of bubble-ring cavitation on the hemispherical nose	48
24	Photograph of band cavitation on the hemispherical nose .	49
25	Photograph showing bubble-ring cavitation and band cavitation on the hemispherical nose	51
26	Sequence of photographs illustrating the elimination of band cavitation by the presence of travelling bubbles on the hemispherical nose.	
	(a) Band cavitation with traces of travelling-bubble cavitation	53
	(b) Band cavitation with increasing amount of travelling-bubble cavitation	54
	(c) Advanced travelling-bubble cavitation. Band cavitation has been eliminated	55
27	Photograph of travelling-bubble cavitation on the tripped hemispherical nose. Laminar boundary layer separation has been eliminated	56

<u>Figure</u>		<u>Page</u>
28	Photograph illustrating the effect of a boundary layer trip on the cavitation characteristics of a hemispherical nose	57
29	Limited cavitation data versus U_{∞} for various types of cavitation on a 2.0-in. diameter Schiebe nose for two values of air content	59
30	Photograph of two types of transient cavitation on the Schiebe nose	60
31	Photograph of a travelling bubble with small lateral tails observed on the Schiebe nose	61
32	Photograph of a travelling bubble with large lateral tails which appear to merge together (lower center) on the Schiebe nose	62
33	Photograph of fixed-patch cavitation (three cavities) on the Schiebe nose	63
34	Photograph of developed cavitation on the Schiebe nose. .	64
35	Photograph of travelling-bubble cavitation on the DTNSRDC nose	68
36	Photograph of a travelling bubble with lateral tails on the DTNSRCC nose	69
37	Photograph of two types of transient cavitation on the DTNSRDC nose	70
38	Limited cavitation data versus U_{∞} for various types of cavitation on a 2.0-in. diameter DTNSRDC nose for two values of air content	72
39	Photograph of band cavitation on the DTNSRDC nose	73
40	Photograph of fixed-patch cavitation (four cavities) on the DTNSRDC nose	75
41	Photograph of developed cavitation of the DTNSRDC nose. .	76
42	Calculated values of R_{max} versus U_{∞} at conditions of limited transient cavitation from several investigations.	83
43	Sketches suggesting the development of travelling-patch cavitation	89

<u>Figure</u>		<u>Page</u>
44	Comparison of limited band cavitation data with $-C_p$ (theoretical and measured) and $-C_{p_t}$ (measured)	92
45	Effect of temperature of σ_d for bubble-ring cavitation on a 2.0-in. diameter hemispherical nose	97
46	Sketch suggesting the effect of thickness of a separation region on the surface pressure distribution	100
47	Sketches illustrating the hypothetical development of fixed-patch cavitation	108
48	Photograph of instrumented 2.0-in. diameter hemispherical nose used for mean pressure measurements	116
49	Measured pressure distribution over a 2.0-in. diameter hemispherical nose for several free stream velocities . .	118
50	Comparison of measured pressure distributions for a 2.0-in. diameter hemispherical nose with and without a boundary layer trip	119
51	Comparison of measured pressure distributions for a 2.0-in. diameter hemispherical nose with and without a boundary layer trip	120
52	Sketch defining important features of a typical measured pressure distribution for a hemispherical nose	122
53	Measured locations of boundary layer transition and reattachment on a 2.0-in. diameter hemispherical nose for variation in free stream velocity	123
54	Photograph of instrumented 2.0-in. diameter hemispherical nose used for fluctuating pressure measurements	129
55	Installation details of a cavity-mounted pressure transducer in a 2.0-in. diameter hemispherical nose . . .	130
56	Levels of normalized rms pressure fluctuations on a 2.0-in. diameter hemispherical nose as a function of Strouhal number for several values of free stream velocity (measured at $x/D = 0.575$)	134
57	Levels of normalized rms pressure fluctuations on a 2.0-in. diameter hemispherical nose as a function of Strouhal number for several values of free stream velocity (measured at $x/D = 0.550$)	135

<u>Figure</u>		<u>Page</u>
58	Levels of normalized rms pressure fluctuations on a 2.0-in. diameter hemispherical nose as a function of Strouhal number for several values of free stream velocity (measured at $x/D = 0.525$)	136
59	Maximum normalized rms pressure fluctuation levels plotted against frequency for three different velocities on a 2.0-in. diameter hemispherical nose	138
60	Maximum normalized rms pressure fluctuation levels plotted against Strouhal number for three different velocities on a 2.0-in. diameter hemispherical nose	139
61	Maximum normalized rms pressure fluctuation levels versus Strouhal number for a tripped and a nontripped 2.0-in. diameter hemispherical nose (measured at $x/D = 0.550$) . .	140
62	Maximum normalized rms pressure fluctuation levels versus Strouhal number for a tripped and a nontripped 2.0-in. diameter hemispherical nose (measured at $x/D = 0.525$) . .	141
63	Sketch illustrating lower and higher frequency contributions to the turbulent energy of transition and reattachment on a 2.0-in. diameter hemispherical nose	142
64	Variation in peak values of normalized maximum rms pressure fluctuations with velocity for higher and lower frequency energy peaks	144
65	Comparison of measured peak frequencies of transitional wave energy with calculated Tollmien-Schlichting frequencies for several free stream velocities	146
66	Sketch illustrating two types of pressure transducer mounting configurations used for calibration purposes . .	171
67	Comparison of energy spectra for cavity-mounted and flush-mounted pressure transducer configurations	172
68	Plot of calibration results which was used to correct for the effect of cavity resonance	174

LIST OF SYMBOLS

<u>Symbol</u>	<u>Definition</u>
c	sonic speed
C_p	pressure coefficient
C_p'	instantaneous pressure coefficient
C_{p_B}	pressure coefficient on an arbitrary smooth body
$C_{p(B)}$	pressure coefficient calculated with blockage effects
$C_{p_{min}}$	minimum pressure coefficient
$C_{p(U-B)}$	pressure coefficient calculated for unblocked flow
$C_{p'_r}$	instantaneous pressure coefficient at location of boundary layer reattachment
C_{p_S}	pressure coefficient at location of boundary layer separation
C_{p_t}	pressure coefficient at location of boundary layer transition
$C_p(t)$	pressure coefficient as a function of time
$C_{p_t \text{meas}}$	measured pressure coefficient at location of transition
d	duct diameter
dB_v	decibel defined by $20 \log v$ ($v = \text{volts}$)
D	body diameter
f_H	Helmholtz frequency
f_{\max}	upper frequency limit
k	Thwaites parameter defined by $\frac{\theta^2}{v} \frac{dU}{dx}$
K	a constant
L	Length of separation bubble
L_d	duct length

<u>Symbol</u>	<u>Definition</u>
m	transducer sensitivity
P'	fluctuating pressure
P_G	pressure of noncondensable gas
P_L	local pressure
P_{atm}	atmospheric pressure
P_{min}	minimum pressure
P'_r	pressure fluctuation at location of reattachment
P'_{rms}	rms fluctuating pressure
P'_{rmsMAX}	maximum rms fluctuating pressure
P'_t	pressure fluctuation at location of transition
P_v	vapor pressure
P_∞	free stream pressure (also surrounding pressure in nonflowing system)
r	duct radius
R	bubble radius
\dot{R}, \ddot{R}	bubble wall velocity, acceleration
R_{crit}	critical bubble radius
Re_D	Reynolds number defined by $\frac{U_\infty D}{\nu}$
$Re_{D_{crit}}$	critical Reynolds number for condition in which position of separation and transition coincide
Re_S	Reynolds number based on streamwise distance (S)
Re_δ	Reynolds number based on boundary layer thickness (δ)
Re_{δ^*}	Reynolds number based on displacement thickness (δ)
Re_θ	Reynolds number based on momentum thickness (θ)
R_f	final bubble radius
R_i	initial bubble radius

<u>Symbol</u>	<u>Definition</u>
R_{\max}	largest bubble radius for which cavitation does not occur
$R_0 \text{crit}$	radius associated with bubbles which produce limited transient cavitation
S	streamwise distance
S_d	standard deviation
\bar{S}_d	relative standard deviation
S_t	Strouhal number defined by $\frac{fD}{U_\infty}$ (f = characteristic frequency)
T_R	temperature at bubble wall
U_L	local velocity
U_∞	free stream velocity
V	cavity volume
x	axial distance
$\frac{x}{D}$	nondimensionalized axial distance
$\frac{x}{D} _{C_p \min}$	nondimensionalized location of $C_p \min$
$\left(\frac{x}{D} \right)_S$	nondimensionalized location of boundary layer separation
$\left(\frac{x}{D} \right)_R$	nondimensionalized location of boundary layer reattachment
$\left(\frac{x}{D} \right)_t$	nondimensionalized location of boundary layer transition
y	body coordinate
α	dissolved air content in parts per million (ppm)
γ	surface tension
δ	boundary layer thickness
δ^*	displacement thickness
ϵ	transducer error

<u>Symbol</u>	<u>Definition</u>
μ	absolute viscosity
ν	kinematic viscosity
ρ	density
ρ_L	liquid density
σ	cavitation number
σ_d	desinent cavitation number
σ_i	incipient cavitation number
σ_l	limited cavitation number
σ_R	cavitation number for an isolated roughness on a flat plate
σ'	cavitation number associated with turbulent pressure fluctuations
$\phi_0(f)$	raw data (dB) plotted against frequency
$\phi_1(f)$	cavity resonance correction factor (dB) plotted against frequency
$\phi_2(f)$	frequency response of charge amplifier (dB)
ϕ_3	calibration constant (dB)
$\phi(f)_{\text{known}}$	signal from known receiver (dB)
$\phi(f)_{\text{unknown}}$	signal from unknown receiver (dB)
$\phi(f)$	corrected data (dB) plotted against frequency

ACKNOWLEDGMENTS

There are many individuals whose help and advice during this investigation are deeply appreciated. The author regrets being unable to personally acknowledge all the people who were helpful to this program.

First and most sincere thanks are extended to Dr. J. William Holl, who as thesis adviser provided guidance and encouragement throughout the course of this research program. Special thanks are also extended to Drs. Michael L. Billet and Gerald C. Lauchle for frequently offering their valuable suggestions and assistance.

The author wishes to extend his thanks to the following Applied Research Laboratory personnel: Robert F. Davis and the computer services personnel for their help with the many theoretical calculations and computer graphics; the editorial personnel who prepared the figures; the drafting personnel, including J. Verne Coontz, George M. Sayers, and others for their help in designing the models; the machine shop personnel, including Robert M. Dillon, Fred W. Hall, Gary R. McClintic, David W. Richards, and others for their help in model fabrication; James H. Rishell, George B. Gurney, and others for their help with experimental equipment; the tunnel operators, Charles R. Hammond and Blair W. Henninger, for their valuable assistance; David R. Stinebring, who assisted with the photography; and undergraduate assistant Michael G. Hill, who was very helpful during the experimental portion of the program.

The author gratefully acknowledges the financial support for this program provided by the Naval Sea Systems Command Code SEA-63R-31 and the Exploratory and Foundational Research Program of the Applied Research Laboratory at The Pennsylvania State University.

CHAPTER 1

INTRODUCTION

1.1 Background Information

"Cavitation" is the general term given to vapor-filled voids which form in a flowing liquid in response to low, dynamically induced pressures. The event of cavitation is of particular interest to the fluids engineer because of its detrimental effects on the operation of hydrodynamic devices. Most notable effects include losses in efficiency, increased noise and vibration, and erosion of the structure. It is, therefore, within the engineer's best interests to understand the mechanisms involved in the process of cavitation inception. The study of cavitation dates back approximately one hundred years to the work of Reynolds [1,2], who apparently described this phenomenon in connection with ship propellers. (These references were obtained from reference [3].) Innumerable investigations have since been carried out involving cavitation in various fluid dynamic applications. Much has been learned about the causes of cavitation and the consequences of its formation. There are still, however, many unsolved problems in the study of cavitation, particularly in the prediction of cavitation inception.

An important parameter in the field of cavitation is the cavitation number, σ , defined by

$$\sigma = \frac{P_{\infty} - P_v}{\frac{1}{2} \rho U_{\infty}^2} , \quad (1)$$

where P_{∞} and U_{∞} are free stream pressure and velocity, respectively;

P_v is the liquid vapor pressure; and ρ is the liquid density. Both P_v and ρ correspond to the bulk temperature of the liquid. This parameter is used to indicate the degree of cavitation development for a particular flow. Generally, high values of σ denote a noncavitating condition, whereas low values indicate an advanced state of cavitation. A state of cavitation development which is of particular interest occurs at the point of transition between cavitating and noncavitating flow. This state describes limited cavitation and is designated by the limited cavitation number, σ_l . The state of limited cavitation is very often used as the reference point when investigating the cavitation characteristics of a particular body. There are two ways to attain limited cavitation. Inception, defined by σ_i , corresponds to the first appearance of cavitation as σ is lowered. Desinence, obtained by raising σ , corresponds to the disappearance of cavitation and is defined by σ_d . Normally, tests are performed such that σ is changed by raising and lowering the tunnel pressure while keeping the free stream velocity constant. Occasionally, differences between σ_i and σ_d have been noted. This hysteresis effect generally gives values of σ_i which are lower than σ_d . Hysteresis is normally studied in terms of delay time. The tunnel pressure is quickly set to a prescribed value which is lower than the desinence pressure. The time lapse until the onset of cavitation is known as the delay time. A more thorough discussion of the topic is presented in references [4] and [5].

Three specific regimes of cavitation are noted as follows:

1. Vaporous cavitation occurs as the result of a phase change from a liquid to a gas. It is marked by the unbounded growth

of bubbles in a liquid where the pressure is less than the vapor pressure of the liquid.

2. Gaseous cavitation results from the mass transport of a non-condensable gas out of liquid solution. This can only occur if the liquid is oversaturated. Time scales for diffusion are relatively large and, therefore, bubble growth by gaseous diffusion is much slower than vaporous growth. Gaseous cavitation can occur at pressures greater than or less than the vapor pressure.
3. Pseudo cavitation is marked by bubble growth according to the pressure-volume relationship of the equation of state. Bubble size varies as the cube root of the ratio of initial to final pressures. Pseudo cavitation, like gaseous, can occur at pressures greater or less than the liquid vapor pressure.

It is not uncommon to have more than one cavitation regime occurring simultaneously. It is, therefore, important to be able to distinguish between the different regimes. Of the three regimes, vaporous cavitation displays the most dramatic characteristics. Because of its violent growth and collapse, it is generally distinguishable from gaseous and pseudo cavitation. The present investigation is primarily concerned with vaporous cavitation.

Another important parameter in the field of cavitation is the pressure coefficient, C_p , defined by

$$C_p = \frac{P_L - P_\infty}{\frac{1}{2} \rho U_\infty^2} \quad (2)$$

where P_L is the local static pressure and P_∞ and U_∞ are free stream static pressure and velocity. The minimum pressure, P_{\min} , on a body corresponds to the minimum pressure coefficient where

$$C_{P_{\min}} = \frac{P_{\min} - P_\infty}{\frac{1}{2}\rho U_\infty^2} . \quad (3)$$

It is often assumed that cavitation inception occurs when the minimum pressure on a body equals the liquid vapor pressure. This gives

$$C_{P_{\min}} = \frac{P_v - P_\infty}{\frac{1}{2}\rho U_\infty^2} \quad (4)$$

or

$$\sigma_i = - C_{P_{\min}} . \quad (5)$$

This is the classical theory for limited cavitation. It should be pointed out that in this theory several factors are assumed negligible; they include surface tension, turbulent pressure fluctuations, noncondensable gas diffusion, and others.

The classical theory of limited cavitation is found to have several shortcomings, particularly for variations in velocity, model size, and liquid properties. These deviations from the classical theory are termed scale effects and are the subject of a large portion of present-day cavitation research. An interesting presentation and discussion of observed scale effects are given in reference [6].

The following are several important factors which are responsible for observed scale effects on limited cavitation:

- 1) noncondensable gas diffusion,
- 2) model size,
- 3) turbulent pressure fluctuations,
- 4) surface roughness,
- 5) velocity, and
- 6) liquid properties.

A brief discussion of these factors is given in reference [7].

It is believed that the actual process of cavitation inception is made possible by the presence of cavitation nuclei in the liquid. Theoretical calculations predict that pure water can withstand tensions of the order of thousands of atmospheres. That such large tensions are not obtainable experimentally is attributed to weak spots in the water. These weak spots or cavitation nuclei are the subjects of many theoretical and experimental investigations. Several of these investigations are summarized by Holl [7].

1.2 Previous Investigations

Much has been learned about cavitation inception as the result of several investigations of cavitation on axisymmetric noses. In 1952, Kermeen [8] presented the results of his observations of cavitation on several different-sized hemispherical noses. Scale effects on limited cavitation were observed for both model-size and velocity variations. Two types of incipient cavitation were reported on all of the hemispheres, namely, clear, steady, attached cavitation and small transient bubbles. Extremely small bubbles were also observed just upstream of the band of small transient bubbles which were believed at that time to be within an attached boundary layer.

The results of limited cavitation tests on several different-sized hemispherical and 1.5-caliber ogive noses were reported in a joint study by Parkin and Holl [9] in 1953. The two test facilities used were the 14-in. High-Speed Water Tunnel located at the Hydrodynamics Laboratory of the California Institute of Technology (CIT) and the 48-in. water tunnel at the Applied Research Laboratory of The Pennsylvania State University (ARL/PSU). It should be mentioned that the CIT facility has a resorber, whereas the ARL/PSU facility does not. Much of the CIT data for the hemispherical noses were taken from Kermeen's work [8]. With the exception of small models at low velocities, the cavitation number (indicating desinence) was shown to systematically increase for both free stream velocity and body size. It was also observed that, for the most part, σ_d was less than $|C_{p_{min}}|$. Further analysis showed that σ_d was not a unique function of Reynolds number. For a constant value of Re_D , σ_d was observed to decrease for increasing model size. It was believed at that time that this size effect was a result of different available bubble growth times corresponding to different model sizes. Subsequent investigations, however, have suggested that viscous effects may be important. No explanation was given for the trend in σ_D with velocity. The measurements of σ_D between the two facilities showed good agreement. No significant effects were reported for air content.

The work of Parkin and Kermeen [10], in 1953, marked the first investigation of boundary layer influence on the inception of cavitation on streamlined axisymmetric models. Experiments performed on 2.0-in. hemispherical noses were motivated by the cavitation observations of Kermeen [8] on the same model. The boundary layer over the model was

assumed to be attached as per the results of Rouse and McNow [11]. From photographs and high speed motion pictures taken during inception, several conclusions were drawn relating microscopic bubble growth within the attached boundary layer to the processes of cavitation inception. Actual tensions were also measured on the hemisphere for conditions of incipient cavitation. These tensions were shown to decrease and even disappear with the appearance of a clear, attached cavity around the model.

Several years later, in 1966, Lindgren and Johnsson [12] presented the results of a comparative study of cavitation observations on a standard axisymmetric body, which had been reported by several different research facilities located worldwide. The study was organized by the International Towing Tank Conference (ITTC) to determine how well cavitation inception data compared for the same model shape when tested in different facilities. The model chosen was the Swedish head-form (ITTC standard headform). No restrictions were placed on the experimental procedure or the model diameter. The cavitation results are presented in Figure 1. It is apparent that the data show very little correlation in either magnitude or velocity trends for the different facilities. Photographs of observed cavitation on the ITTC standard headform from several of the different test facilities are presented in Figure 2 (Gates [13]). Three types of cavitation are shown in Figure 2, namely, "band" type in frames 4, 5, and 9, "spot" type in frame 6, and "travelling-bubble" type in frames 1, 2, 3, 7, and 8.

Flow visualization studies on axisymmetric bodies in 1973, by Arakeri [14] and Arakeri and Acosta [15], were extremely helpful in

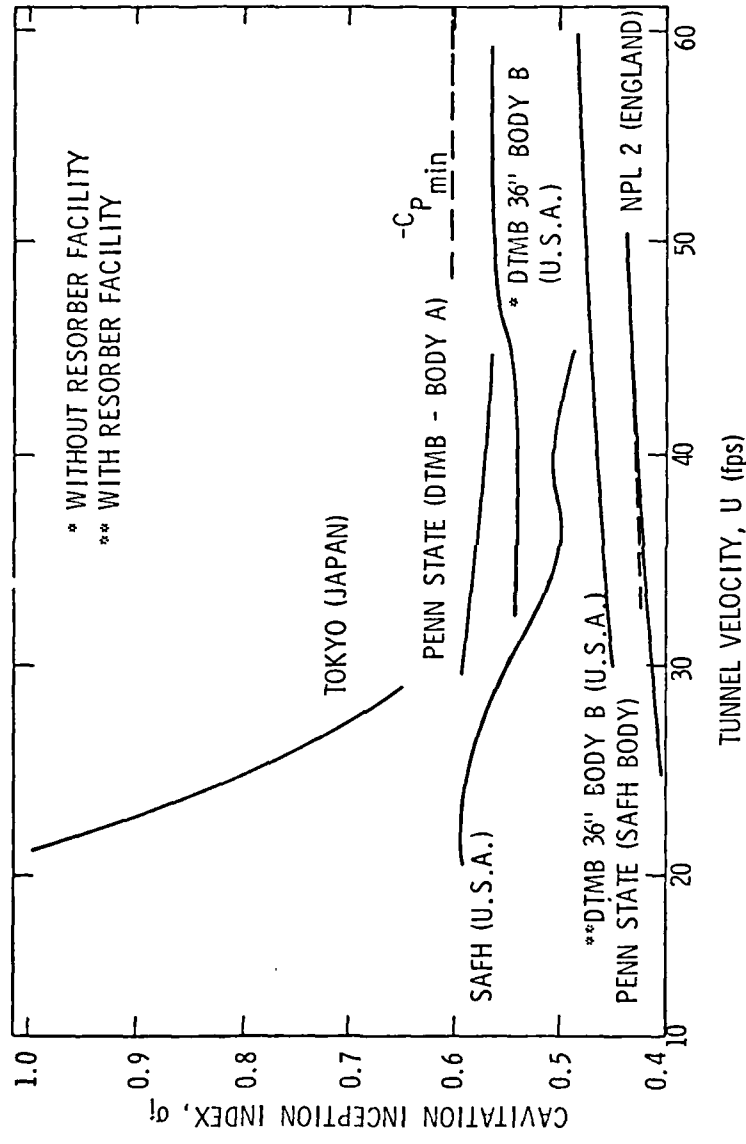


Figure 1. Comparison of cavitation inception results for a Swedish headform from several worldwide facilities sponsored by the International Towing Tank Conference. Taken from Figure 2 of reference [13].

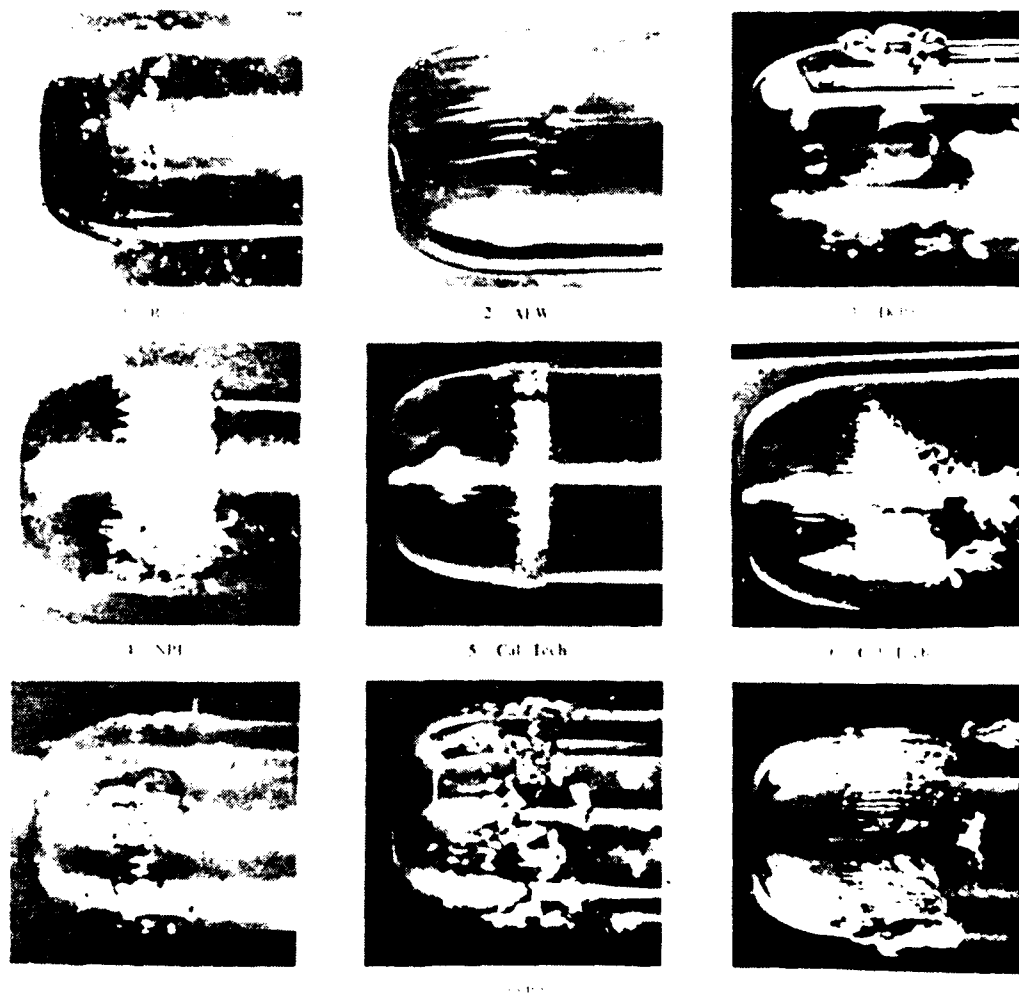


Figure 2. Photographs of various types of cavitation observed on the ITTC nose in different testing facilities. Taken from Figure 3 of reference [13].

obtaining a better knowledge of the cavitation inception process. Using the Schlieren technique for flow visualization, Arakeri and Acosta showed that laminar boundary layer separation occurs on both the hemispherical nose and ITTC nose for Reynolds numbers much higher than previously believed. They also showed that certain types of cavitation are controlled by the presence of laminar boundary layer separation. Their observations helped to bring about a resurgence of research activity in the field of cavitation inception on axisymmetric bodies.

A follow-up study was performed by Arakeri and Acosta [16] in 1976 on cavitation inception as it is influenced by laminar boundary layer separation. Results showed conclusively that the elimination of separation, by a trip or natural transition, had a pronounced effect on the cavitation inception characteristics of certain axisymmetric bodies. The results suggest that differences in cavitation observations from one water tunnel facility to another may be dependent upon variations in the free stream turbulence levels of the respective facilities.

In a similar investigation in 1976, Van der Meulen [17] studied and compared cavitation inception on a hemispherical nose and a Schiebe nose. The minimum pressure coefficients for these bodies were similar; however, the hemispherical nose experiences laminar separation, whereas the Schiebe nose does not. A method was devised to eliminate boundary layer separation on the hemispherical nose by the injection of a polymer into the boundary layer. Flow visualization was achieved by holographic photography. Results showed that the elimination of laminar separation by polymer injection on the hemispherical nose produced a significant change in the appearance of cavitation on this model. Without polymer

injection, cavitation appeared as "travelling bubbles" on the Schiebe nose and as "sheet" cavitation on the hemispherical nose. Polymer injection and the resultant elimination of laminar separation on the hemispherical nose produced cavitation which more closely resembled that for the Schiebe nose.

Most recently, in 1977, Gates [13] investigated the effects of environmental factors on the inception of cavitation on axisymmetric bodies. A Schlieren flow visualization technique similar to that used by Arakeri [14] provided information on the boundary layer status, i.e., separated or attached. Gates' results showed that laminar boundary layer separation on axisymmetric models may be eliminated by increasing the free stream turbulence or by injecting polymer into the boundary layer. Elimination of laminar separation produced a large reduction in the incipient cavitation number and a change from band cavitation to somewhat distorted band and travelling-bubble cavitation. He also observed the removal of laminar separation and band cavitation by the presence of a large number of free stream bubbles. Band cavitation showed no effect due to variation of the nuclei population. It is believed that the nuclei population within the separation region is different from the population in the free stream. If laminar separation is removed, travelling-bubble cavitation results. Travelling-bubble cavitation appears to be closely associated with the free stream nuclei population.

1.3 Objectives of this Investigation

It is apparent from the results of previous investigations that several notably different types of cavitation have been observed on

axisymmetric models. The occurrence of various types of cavitation suggests that numerous scaling laws may exist. These scaling laws may be associated with properties of the test facility, e.g., turbulence level, nuclei population, etc., and/or properties of the model, e.g., $C_P \text{min}$, boundary layer characteristics, and so forth. To the author's knowledge, however, no attempt has been made to study systematically each cavitation type individually and to define the various mechanisms involved. Such information would be very helpful in comparative cavitation studies, particularly when different test facilities are used. The objectives of this investigation include documentation of the various types of cavitation occurring on axisymmetric models and identification of the corresponding flow states. The effects of air content and water temperature will also be discussed.

Cavitation inception and desinence tests were performed on three different axisymmetric models in the present investigation. The models, all 2.0-in. in diameter, include a hemispherical nose, a Schiebe nose, and a DTNSRDC nose. All tests were recorded on audiovisual tape for playback at normal speed, slow motion, or single-frame viewing. This recording procedure was particularly valuable in studying the transient types of cavitation. Cavitation tests were performed at two different air contents over a velocity range of typically 30.0 to 70.0 fps. Limited cavitation data corresponding to each different type of cavitation were subsequently obtained from the recorded tapes. Documentation of the various observed cavitation types includes:

- 1) detailed written descriptions;
- 2) limited cavitation data;

- 3) indication of flow state, i.e., separated or attached boundary layer; and
- 4) photographs.

An attempt was made to define the underlying mechanisms responsible for each of the different cavitation types and their characteristics. In addition, the conditions are given for which these types of cavitation have been observed. Two additional tests were performed on the hemispherical nose, namely, the measurement of mean and fluctuating pressures. Mean pressure measurements were made to determine the effect of laminar boundary layer separation on the pressure distribution as a function of Reynolds number. Also, fluctuating pressure measurements were made in the region of boundary layer reattachment. The results of these measurements are referred to in the discussion of separation-controlled cavitation observed on the hemispherical nose.

CHAPTER 2

EXPERIMENTAL METHODS

2.1 Test Models

In the early stages of this investigation, several axisymmetric models were considered for the test program. These models included the following:

- 1) hemispherical nose,
- 2) 1.5-caliber ogive nose,
- 3) 1.0-caliber ogive nose,
- 4) DTNSRDC nose,
- 5) ITTC nose, and
- 6) Schiebe nose.

The models consisted of a machined nose section followed by a short, cylindrical afterbody. All six models, along with a streamlined mounting strut, were designed and machined at the onset of the investigation. The 2.0-in. diameter models were made of stainless steel. Nose contours are defined in Figures 3(a) through 3(e). The contour of the Schiebe nose, Figure 3(e), is one of a family of shapes analytically defined by placing a disk-shaped source distribution normal to a free stream. For details, refer to reference [18]. Coordinates for the Schiebe nose are taken from reference [17] and are tabulated in Table 1.

Contour inspections of the models were made by comparing a magnified trace of each model's contour with the appropriate ideal curve generated on a computer. Errors in the contours were determined by calculating the normal distance from the ideal curve to the magnified trace.

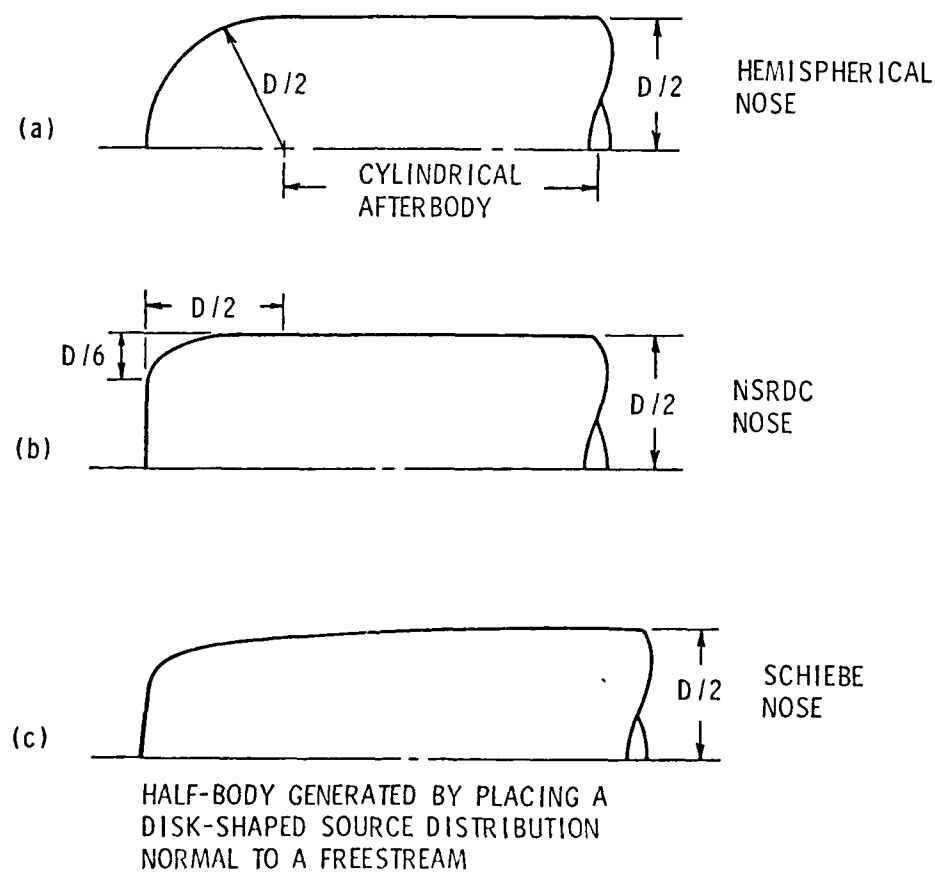


Figure 3. Geometric details of axisymmetric test models.

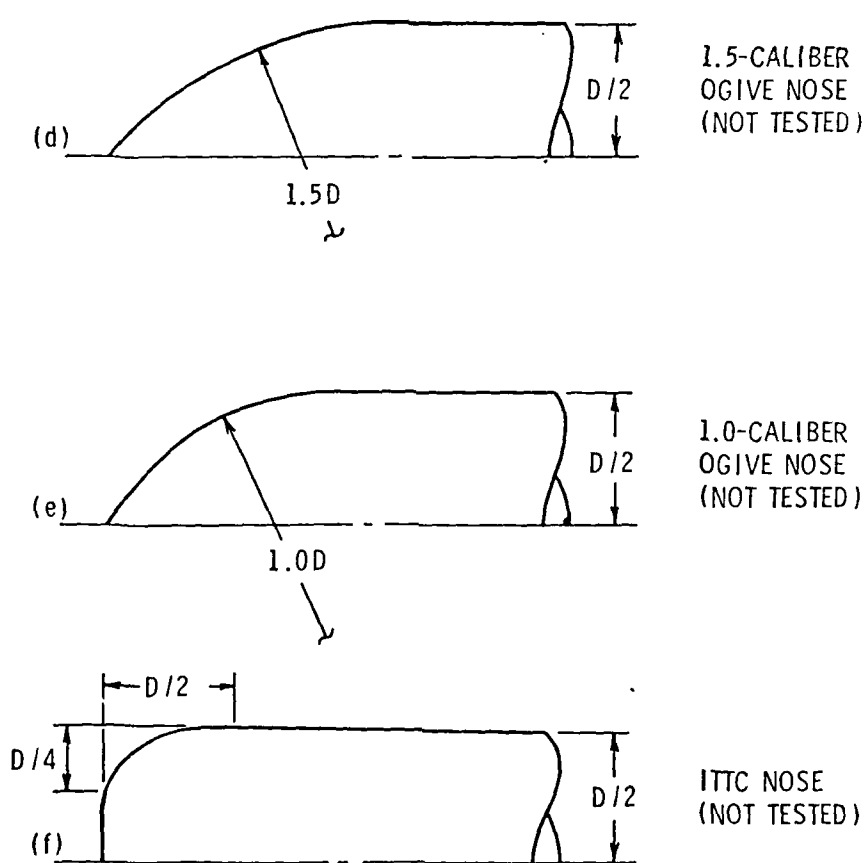


Figure 3 (Continued). Geometric details of axisymmetric test models.

Table 1. Coordinates of Schiebe Nose.
Taken from reference [17].

Axial Coordinate Over Diameter	Body Coordinate Over Diameter
$\frac{X}{D}$	$\frac{Y}{D}$
0.000	0.0000
0.000	0.0180
0.005	0.1451
0.010	0.1995
0.020	0.2654
0.030	0.3037
0.040	0.3264
0.050	0.3407
0.060	0.3511
0.070	0.3594
0.080	0.3665
0.090	0.3727
0.100	0.3784
0.120	0.3882
0.150	0.4003
0.200	0.4163
0.250	0.4286
0.300	0.4385
0.400	0.4532
0.500	0.4636
0.600	0.4710
0.700	0.4766
0.800	0.4808
1.000	0.4865
1.200	0.4901
1.400	0.4925
1.600	0.4941
2.000	0.4961
2.200	0.4968
2.400	0.4973

Results indicated that, generally, the model contours did not deviate from the ideal curves by more than 0.2 percent of the body diameter.

It was decided that the experimental program should be limited to three models, namely, the hemispherical nose, the Schiebe nose, and the DTNSRDC nose. These models were chosen on the basis of their particular flow characteristics. The hemispherical nose is predicted to experience laminar boundary layer separation over the entire test range. The critical Reynolds number, $Re_{D_{crit}}$, for this body is given as 5×10^6 [15], which corresponds to a free stream velocity of 300 fps for a 2.0-in. diameter body. Therefore, under normal conditions, laminar separation occurs on a 2.0-in. diameter hemispherical nose for all test velocities. The Schiebe nose, according to laminar boundary layer calculations, does not separate, which indicates that a fully attached boundary layer occurs on this body for all test velocities. The DTNSRDC nose is reported [16] to have a critical Reynolds number of 5×10^5 which, for a 2.0-in. model, corresponds to a free stream velocity of 30.0 fps. Laminar boundary layer calculations indicate that separation occurs on this model. Therefore, for free stream velocities of less than about 30.0 fps, laminar boundary layer separation occurs and, for higher velocities, a fully attached boundary layer is present.

2.2 Test Facility

All experimental work was performed in the 12-in. water tunnel located in the Garfield Thomas Water Tunnel Building of the Applied Research Laboratory at The Pennsylvania State University. A complete description of this facility is presented by Lehman [19]. The tunnel,

which is of the recirculating type, can attain test section velocities in excess of 70.0 fps. The pressurization system provides automatic control of the tunnel test section pressure over the range of 2.0-to-40.0 psia. Tunnel flow passes through a 9-to-1 contraction ratio nozzle just before entering the test section. A honeycomb, 4.0-in. deep with 1/8-in. cells, is located in the plenum section to reduce free stream turbulence. The turbulence intensity in the test section was measured to be less than 0.5 percent.

Test models were mounted in the test section on a strut-mounted afterbody assembly. Alignment of the mounting assembly was done by trial and error. True alignment was assumed when cavitation inception was observed to occur uniformly around the hemispherical headform.

2.3 Experimental Procedure

Cavitation tests were performed on the hemispherical nose, the Schiebe nose, and the DTNSRDC nose for two different air contents. Data were taken for free stream velocities ranging typically from 30.0 to 70.0 fps. All cavitation tests were recorded on audio-visual tape for later analysis. Photographs were also taken of the various forms of observed cavitation.

Free stream velocity was determined from the measured pressure drop, ΔP , through the nozzle just upstream of the test section. Absolute tunnel centerline pressure, P_∞ , and ΔP were both measured with Bell and Howell differential-type pressure transducers. The corresponding output voltages were displayed on separate digital voltmeters. A static calibration was performed for each pressure

transducer prior to testing. Both transducers proved to be linear within their respective pressure ranges.

Recording the cavitation tests required that pressure and velocity information be recorded simultaneously with the cavitation occurrences on the test body. This was done by positioning the two voltmeters on the far side of the tunnel so that the digital displays were visible through the rear test section window above and below the model.

Lighting for the model was provided by a strobe light positioned above the test section. The strobe light frequency was set to match the framing rate of the video recorder (about 60.0 flashes per sec).

During the course of each test, additional information, including water temperature, atmospheric pressure, and the time was recorded verbally; occasionally descriptive comments relative to the cavitation events were also recorded.

Each cavitation test was preceded by a measurement of the total air content in parts per million on a mole basis (ppm) of the water with a Van Slyke apparatus. To lower the air content, tunnel water was bypassed through an external deaeration system. Raising the air content was achieved by venting the tunnel to the atmosphere. Once the desired air content was achieved, the tunnel velocity was set at 70.0 fps and the pressure at 30.0 psia for a few minutes to let the system reach a state of equilibrium. At this point, the test was ready to begin. For convenience, the following sequence will be defined as a run: at a constant free stream velocity, the static pressure is slowly lowered until sufficient cavitation is observed; the pressure is then slowly raised until all cavitation is gone; a run is then considered

complete. For each test velocity, the audio-visual recorder was turned on and three runs were performed. All tests were carried out in the same fashion, starting at a velocity of 70.0 fps and proceeding to lower velocities, generally, in increments of 10.0 fps. The air content was measured at the end of each test and averaged with the value measured prior to the test. Cavitation tests for the three models were all carried out in this manner. Cavitation data were then taken from the tapes. Calling cavitation from tapes proved to be more reliable, since the recorded action could be slowed down, stopped, and repeated. The tapes were also very helpful in studying each model's cavitation characteristics.

Still photographs were taken of the different types of cavitation on all three models. A Nikkormat 35-mm camera was used with Kodak Plus-X Pan film. Two strobe lights positioned outside of the test section on the side and above the model provided sufficient light. Several large Fresnel lenses were used to focus the light on the model. All still photography was done after the cavitation tests were complete.

CHAPTER 3

THEORETICAL FLOW CALCULATIONS

Pressure distributions and laminar boundary layer calculations were performed for all of the axisymmetric models mentioned previously. Pressure distributions were calculated using the two-dimensional Douglas-Neumann program for both blocked and unblocked cases. Laminar boundary layer calculations employed the Thwaites approximate method for obtaining the momentum thickness, θ . A Pohlhausen velocity profile was assumed in the determination of displacement thickness, δ^* , and boundary layer thickness, δ . Calculations were performed at incremental streamwise stations along each body up to the position of laminar boundary layer separation. For nonseparating bodies, the calculations were arbitrarily terminated. Laminar boundary layer separation was assumed to occur when the parameter k , defined by $(\theta^2/v)(dU/dS)$, reached a value of -0.09.

Plots of theoretical pressure coefficient, C_p , versus nondimensionalized axial distance, x/D , are presented in Figures 4, 5, and 6 for the hemispherical nose, the DTNSRDC nose, and Schiebe nose, respectively. Two curves are shown on each plot. The dashed curve represents the pressure distribution with blockage effects as determined for a 2.0-in. diameter model in a 12.0-in. diameter tunnel. The solid curve shows the pressure distribution calculated for the model in free stream conditions.

Results of laminar boundary layer calculations are presented as curves of $Re_\delta/\sqrt{Re_D}$, $Re_{\delta^*}/\sqrt{Re_D}$, $Re_\theta/\sqrt{Re_D}$, and Re_S/Re_D as a function of the nondimensionalized axial distance, x/D . These curves are presented

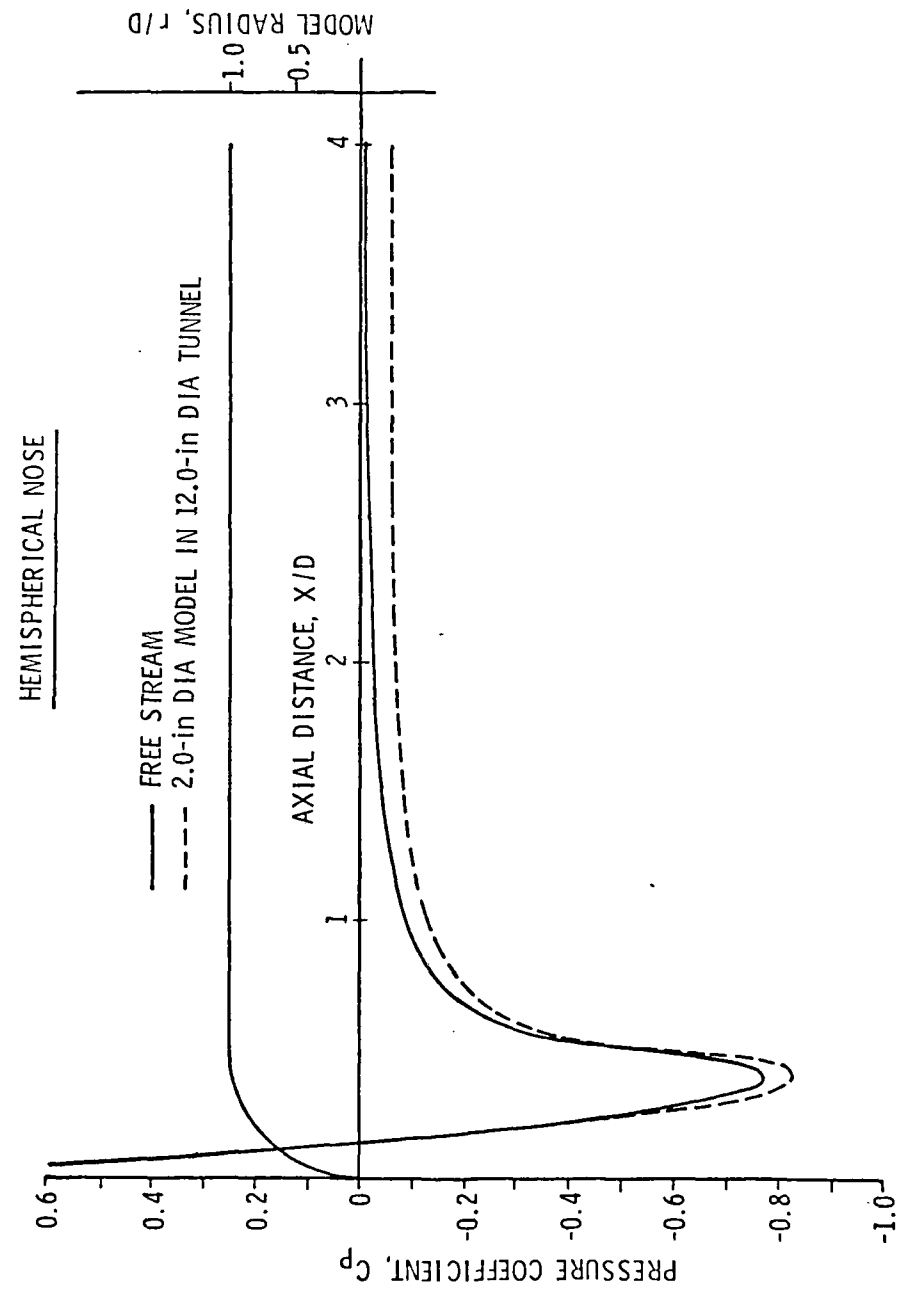


Figure 4. Douglas Neumann pressure distribution for a 2.0-in. diameter hemispherical nose in a 12.0-in. diameter tunnel and in a free stream.

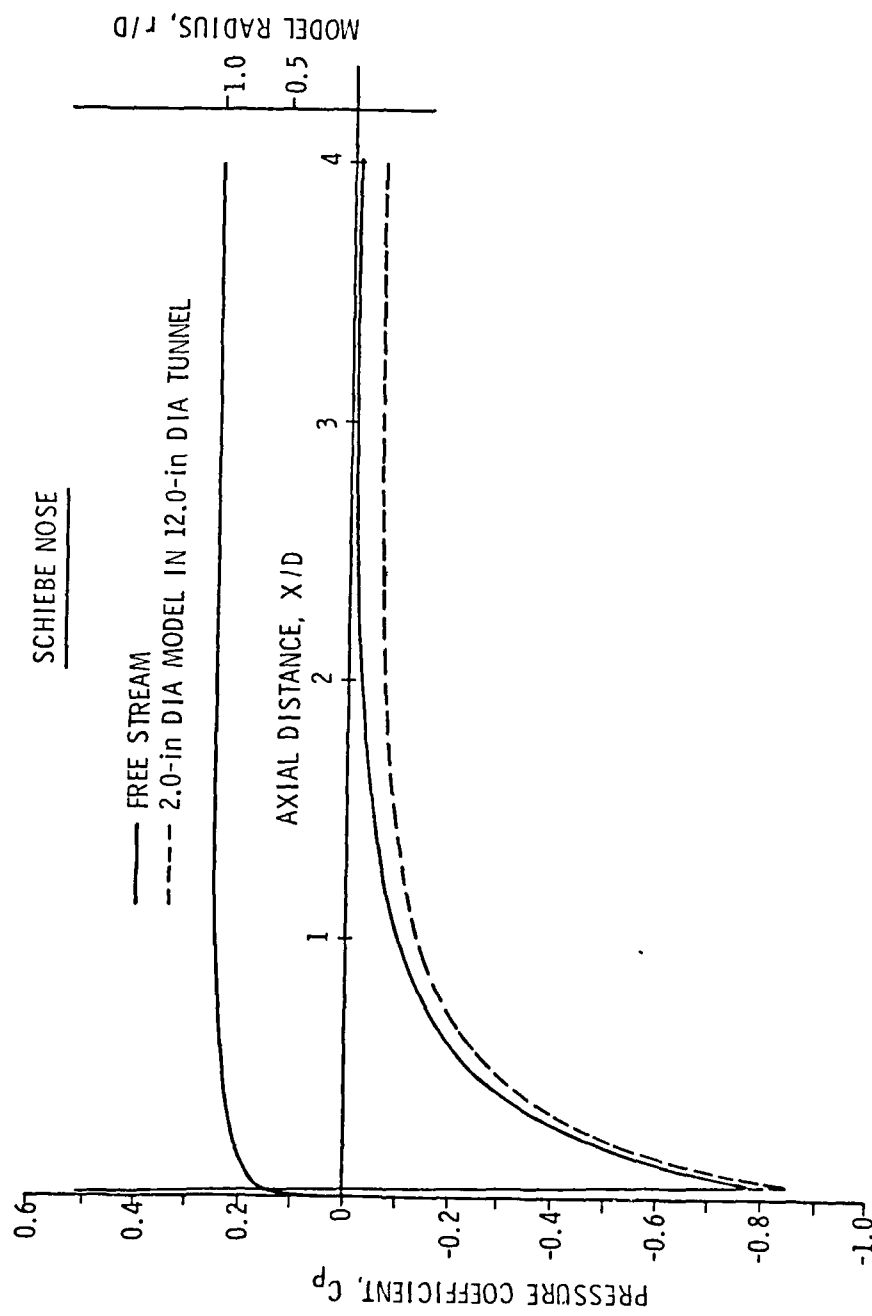


Figure 5. Douglas Neumann pressure distribution for a 2.0-in. diameter Schiebe nose in a 12.0-in. diameter tunnel and in a free stream.

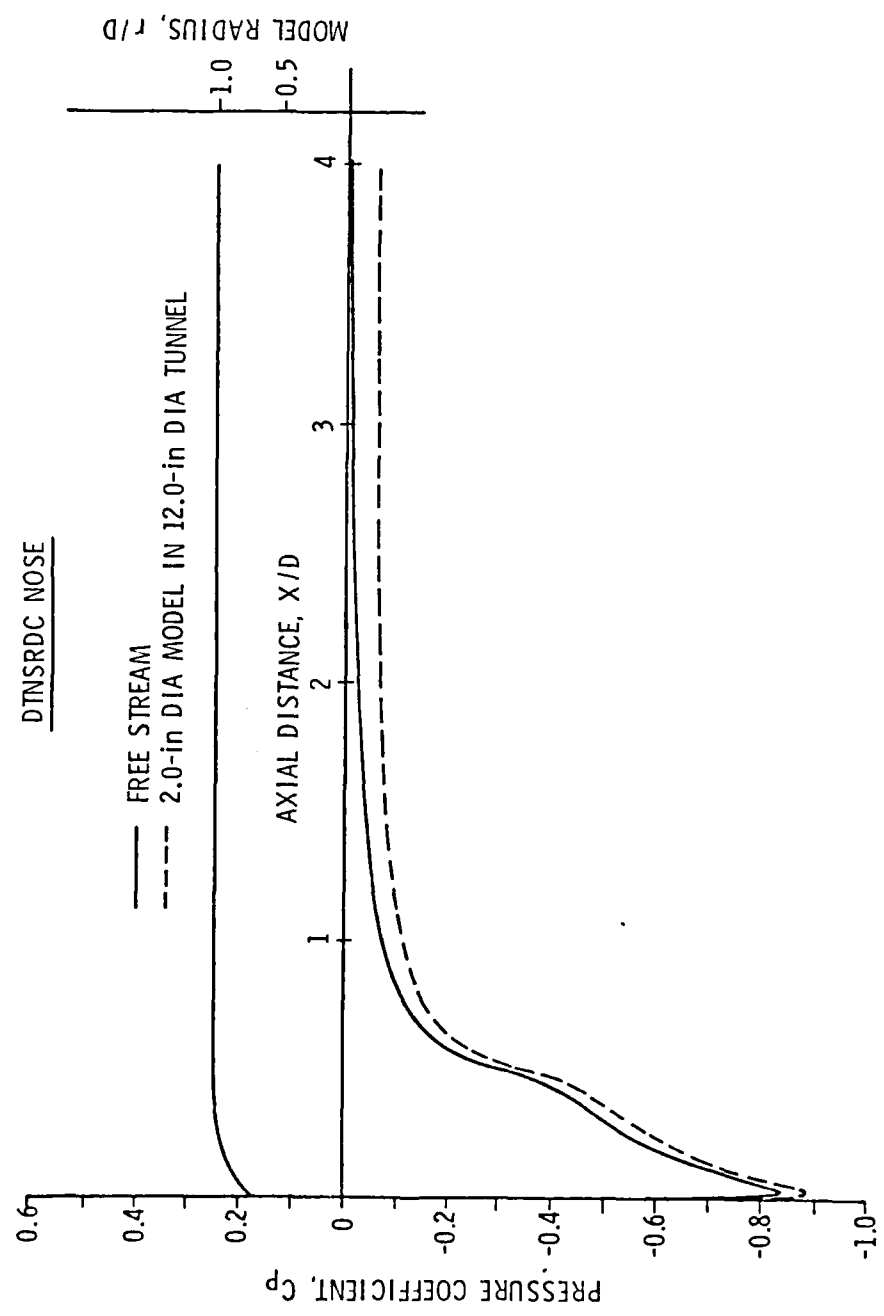


Figure 6. Douglas Neumann pressure distribution for a 2.0-in. diameter DTNSRDC nose in a 12.0-in. diameter tunnel and in a free stream.

for the hemispherical nose, the DTNSRDC nose, and the Schiebe nose in Figures 7, 8, and 9, respectively. Curves for both hemispherical and DTNSRDC noses are terminated at the theoretically predicted location of laminar boundary layer separation. The corresponding values of x/D are 0.462 and 0.485, respectively. Calculations for the Schiebe nose were carried out to an x/D of about 0.475. It is important to note that these results only hold for attached laminar boundary layers.

It was mentioned previously that pressure distributions and boundary layer calculations were also performed for a 1.5-caliber ogive nose, a 1.0-caliber ogive nose, and an ITTC nose. These results are presented for additional information. Pressure distributions are shown in Figures 10, 11, and 12 and boundary layer results are shown in Figures 13, 14, and 15.

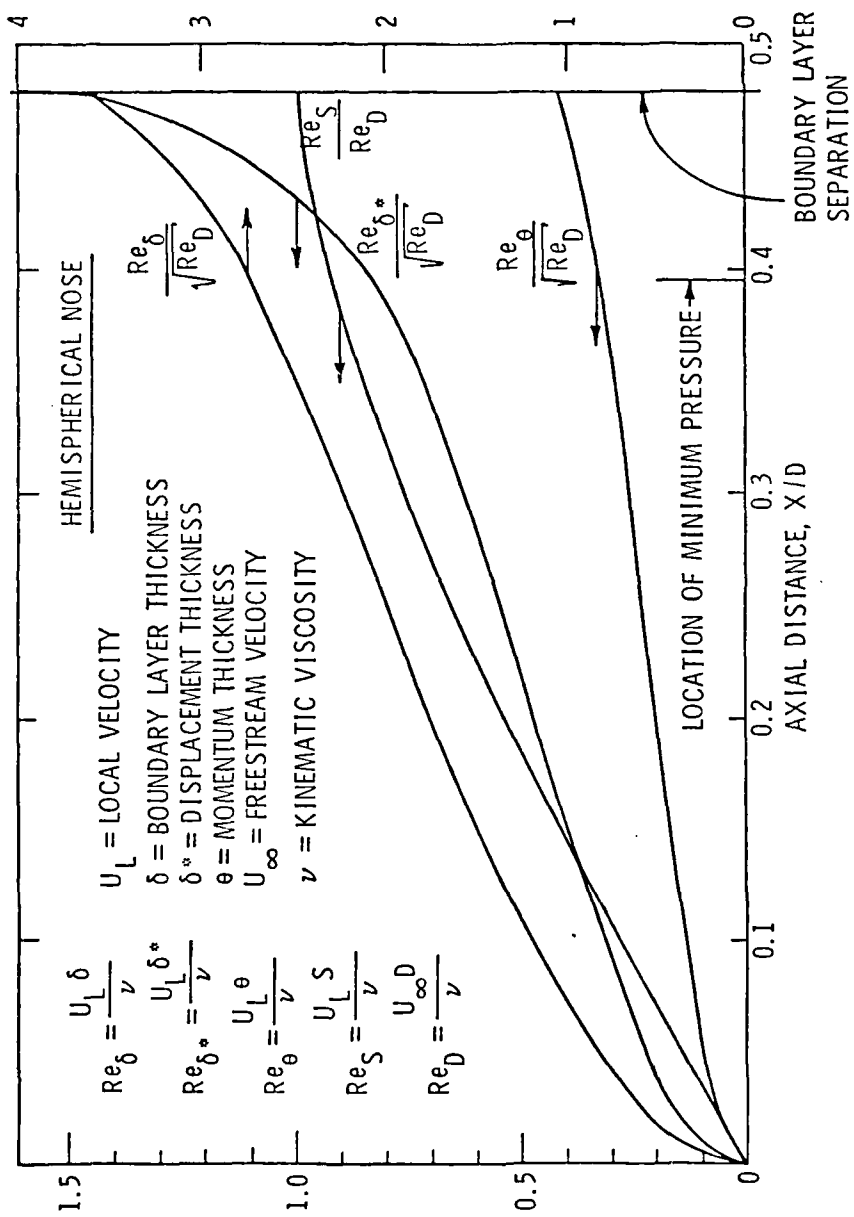


Figure 7. Development of laminar boundary layer along a 2.0-in diameter hemispherical nose.

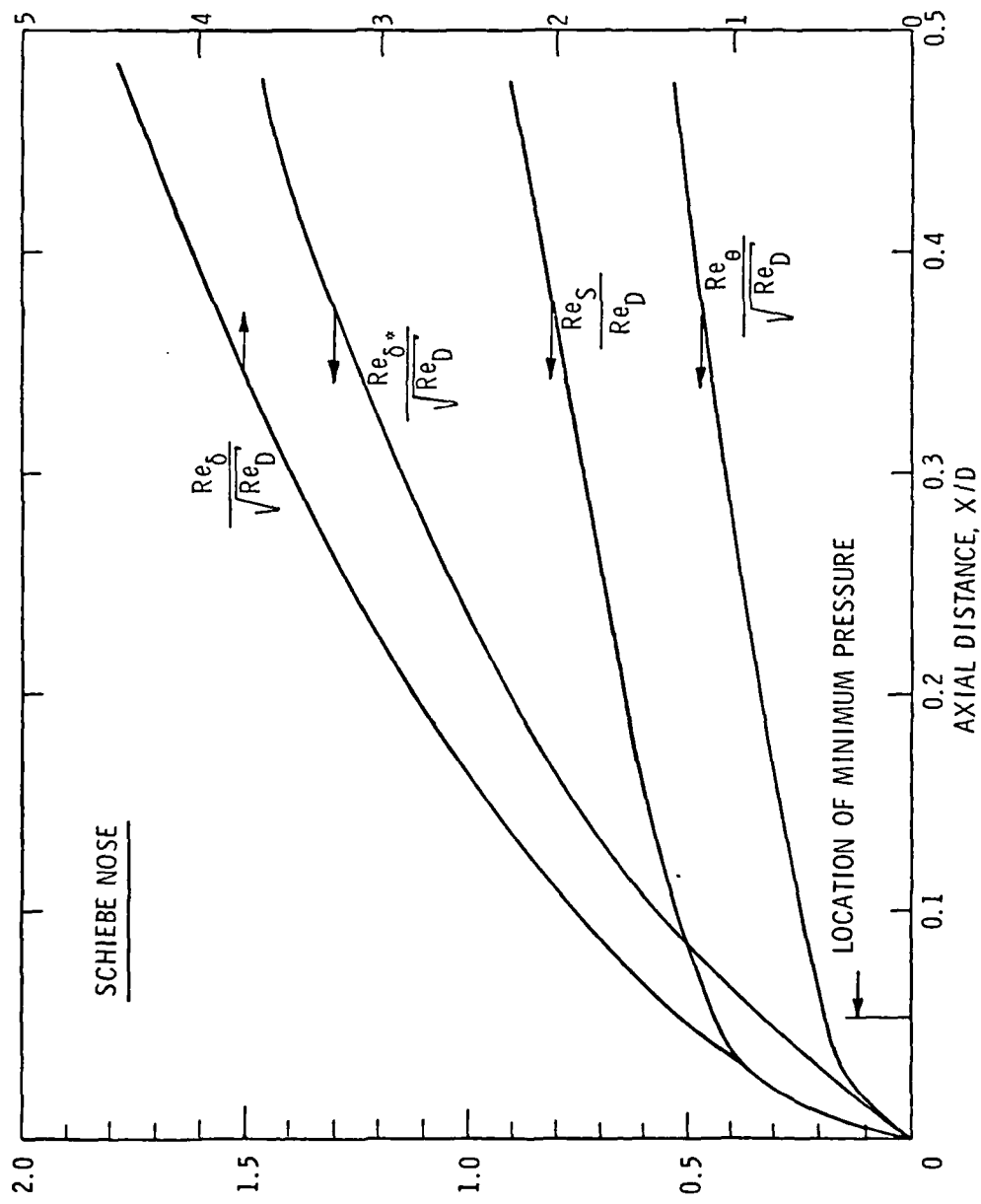


Figure 8. Development of laminar boundary layer along a 2.0-in. diameter Schiebe nose.

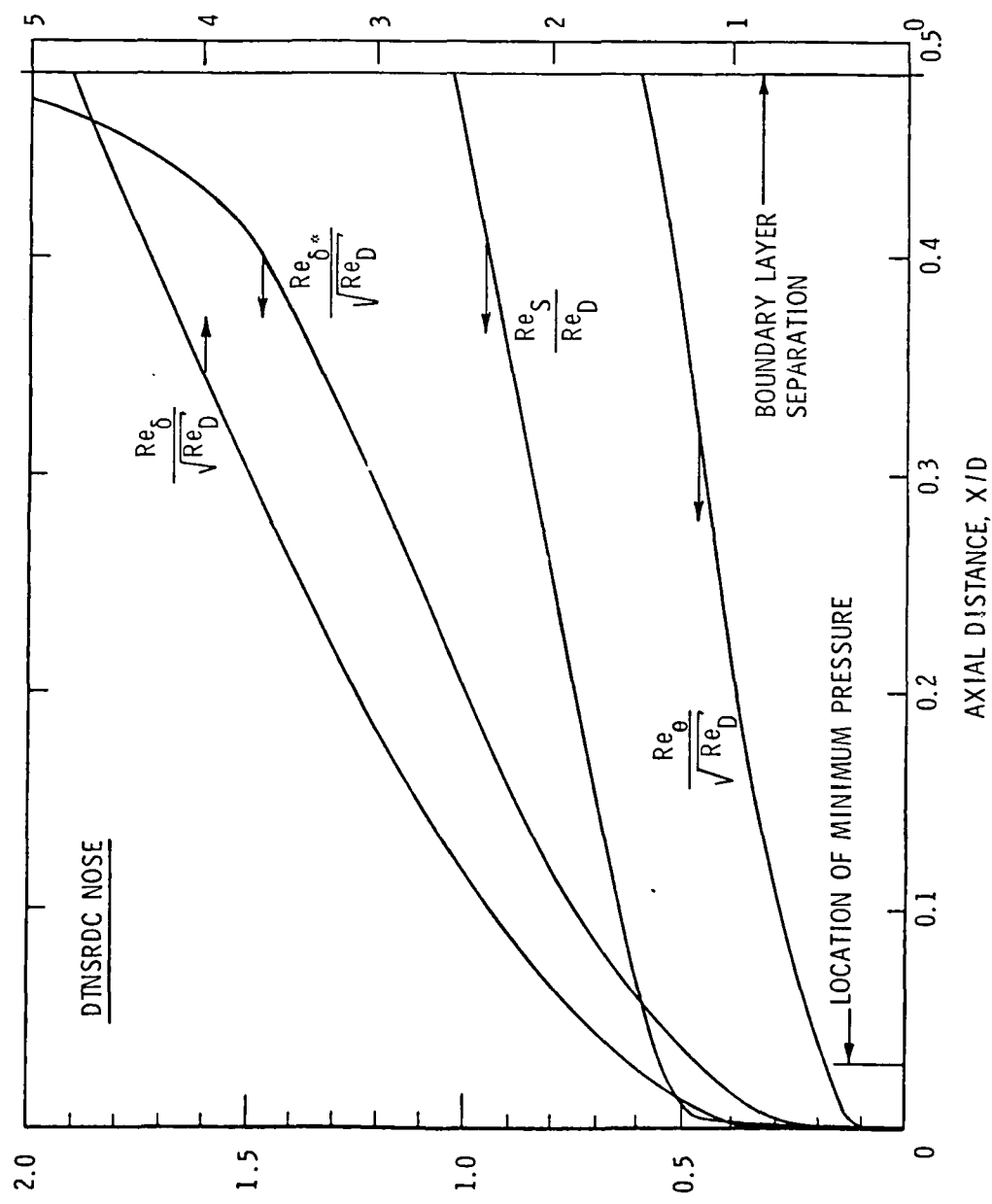


Figure 9. Development of laminar boundary layer along a 2.0-in. diameter DTNSRDC nose.

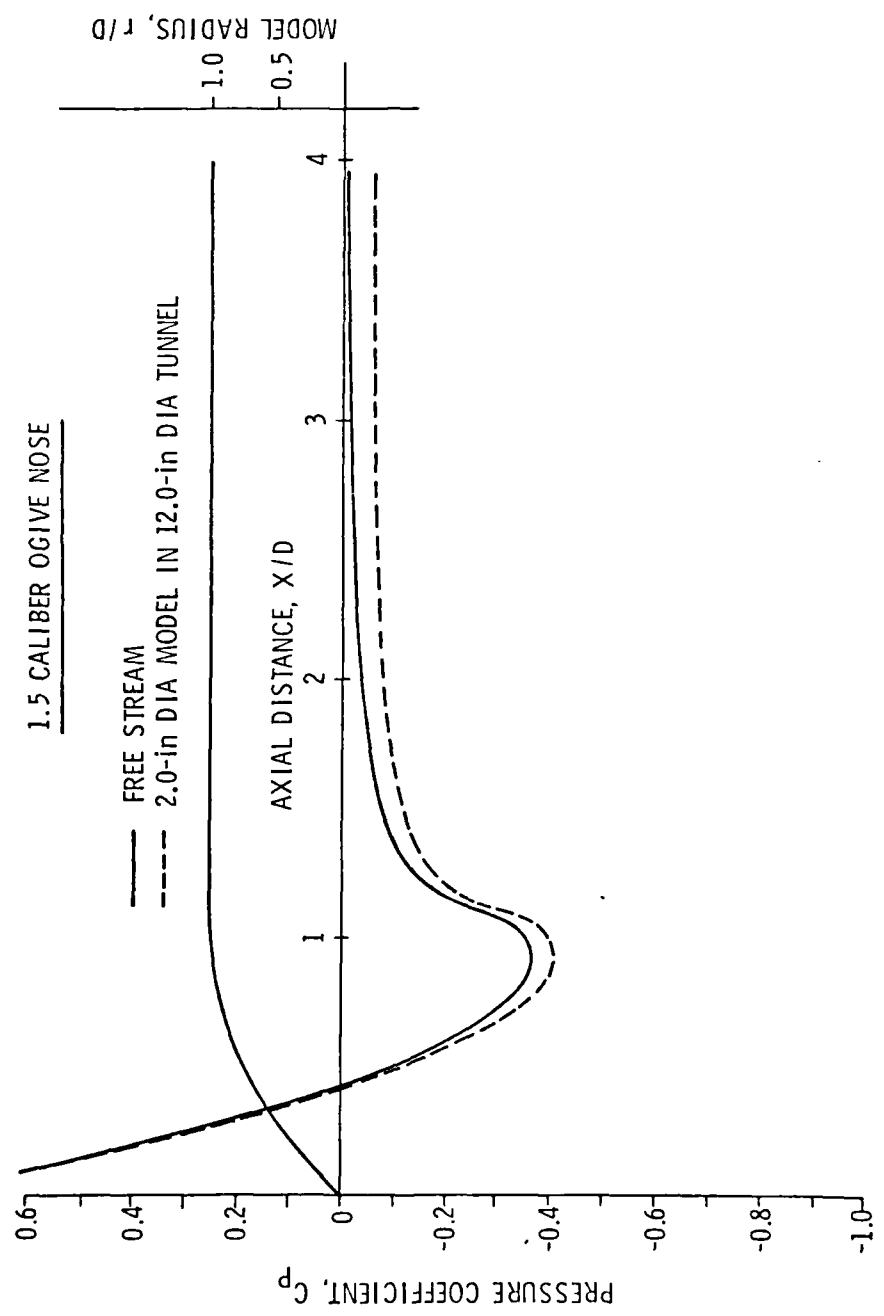


Figure 10. Douglas Neumann pressure distribution for a 2.0-in. diameter, 1.5-caliber ogive nose in a 12.0-in. diameter tunnel and in a free stream.

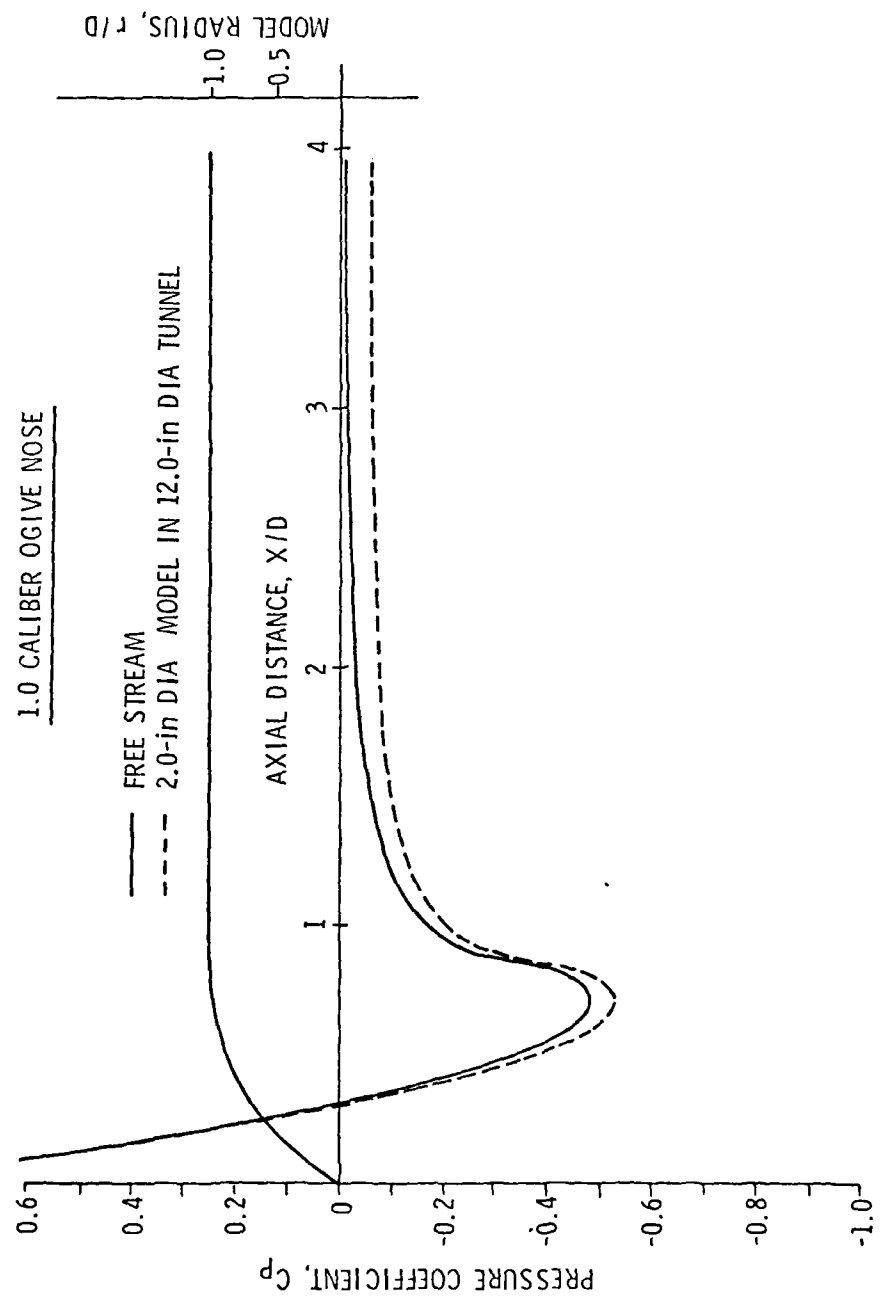


Figure 11. Douglas Neumann pressure distribution for a 2.0-in. diameter, 1.0-caliber ogive nose in a 12.0-in. diameter tunnel and in a free stream.

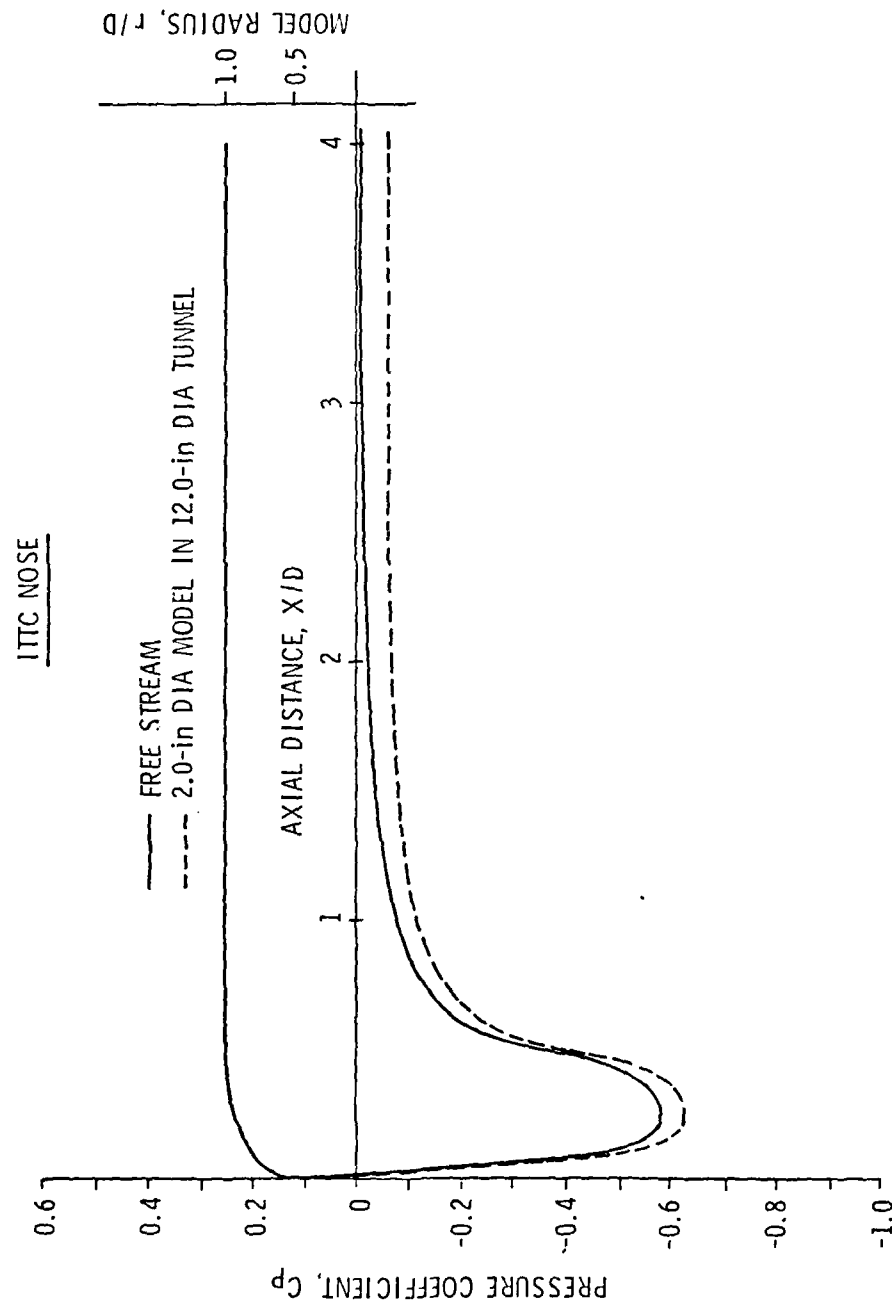


Figure 12. Douglas Neumann pressure distribution for a 2.0-in. diameter ITTC nose in a 12.0-in. diameter tunnel and in a free stream.

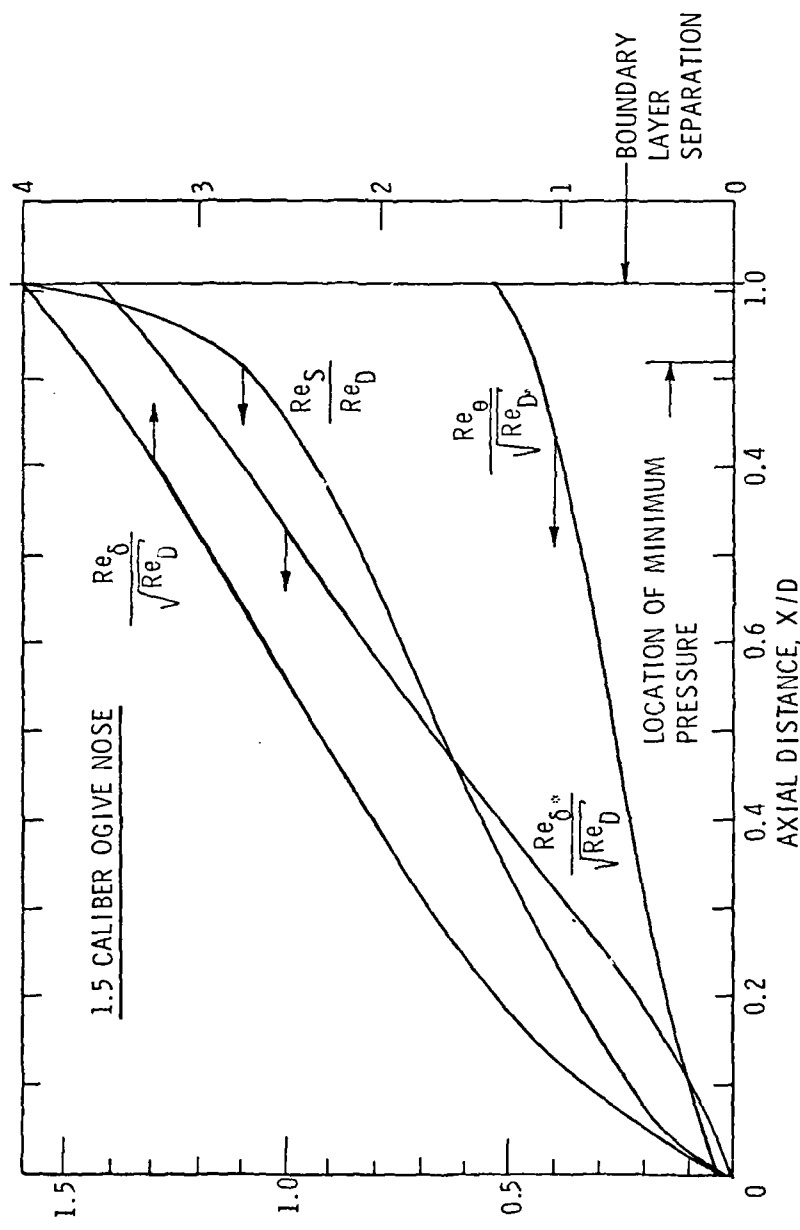


Figure 13. Development of laminar boundary layer along a 2.0-in. diameter, 1.5-caliber ogive nose.

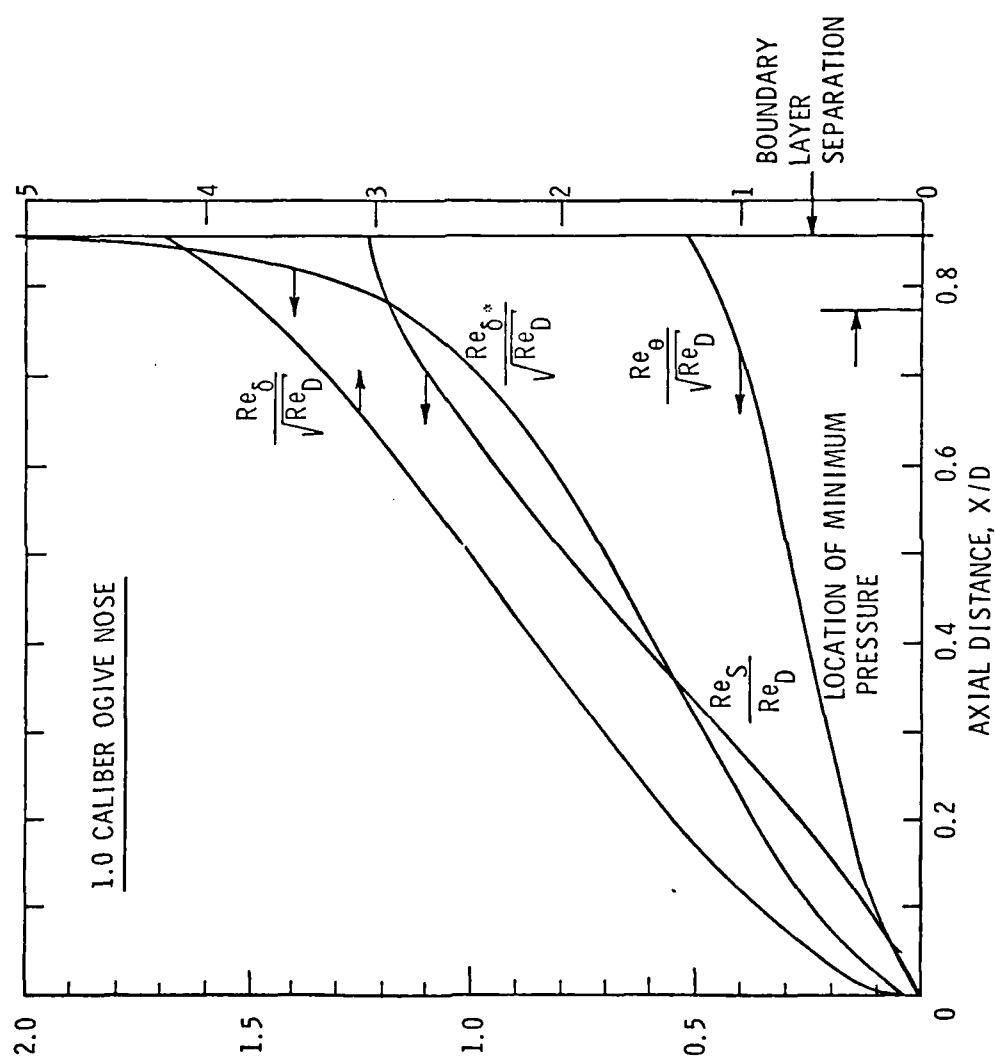


Figure 14. Development of laminar boundary layer along a 2.0-in. diameter, 1.0-caliber ogive nose.

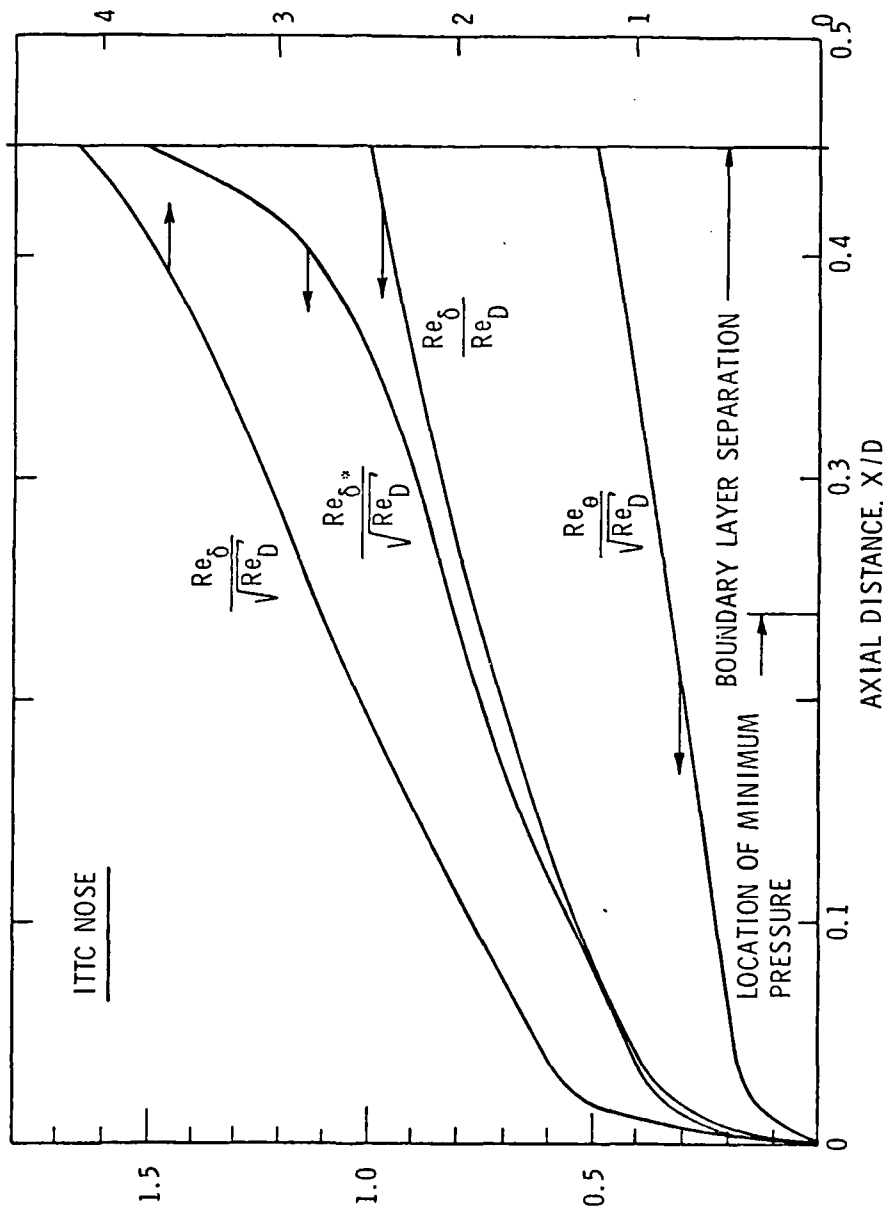


Figure 15. Development of laminar boundary layer along a 2.0-in. diameter ITTC nose.

CHAPTER 4

OBSERVATIONS OF LIMITED CAVITATION ON AXISYMMETRIC MODELS

4.1 General Descriptions of Limited Cavitation Types

Several forms of cavitation were observed on the three different models tested in this investigation. However, not all cavitation types were seen on all three models. The types observed in the present investigation are classified under two general categories, namely, transient and attached cavitation. Transient cavitation is characterized by cavities which grow and collapse very rapidly. This type of cavitation does not appear to be attached in any way to the model. Because of its short life, transient cavitation is very difficult to observe with the unaided eye under normal lighting conditions. The cavities generally appear as blurred streaks giving no indication of actual shape. Only with the aid of a strobe light is it possible to observe and photograph this form of cavitation. On the other hand, attached cavitation usually occurs as a quasi-steady cavity which appears fixed to the body and is readily observable with the unaided eye under normal lighting conditions.

The various types of cavitation observed in the present investigation are categorized and defined in the following two sections. The complete results of cavitation tests on the three axisymmetric models are presented in Section 4.2.

4.1.1 Transient cavitation. Three types of transient cavitation have been observed, namely, travelling-bubble cavitation, travelling-patch cavitation, and bubble-ring cavitation. Travelling-bubble

cavitation is so named because it appears in the form of nearly spherical cavities which rapidly grow and collapse as they travel with the flow through the low pressure region of a hydrodynamic body. A sketch illustrating the general appearance of travelling-bubble cavitation on an arbitrary headform is presented in Figure 16.

Travelling-patch cavitation differs from travelling-bubble cavitation mostly by its appearance, which is similar to that of a seashell inverted over the surface of the model. Like travelling-bubble cavitation, travelling-patch cavitation appears as randomly occurring cavities in the low pressure regions of hydrodynamic bodies. A sketch showing the details of travelling-patch cavitation on an arbitrary headform is presented in Figure 17.

Bubble-ring cavitation was observed only on the hemispherical nose in this investigation and is described in further detail in Section 4.2.1. This form of cavitation appears to be a very specialized type of cavitation for, not only does it depend upon the presence of laminar separation, but also it must depend on other factors since it has been observed on only two bodies, namely, the hemispherical and the 1/8-caliber ogive noses.

4.1.2 Attached cavitation. Three distinct forms of attached cavitation were noted. They are:

- 1) band cavitation,
- 2) fixed-patch cavitation, and
- 3) developed cavitation.

Band cavitation occurs on bodies which normally exhibit laminar boundary layer separation in noncavitating flow. The cavity generally develops

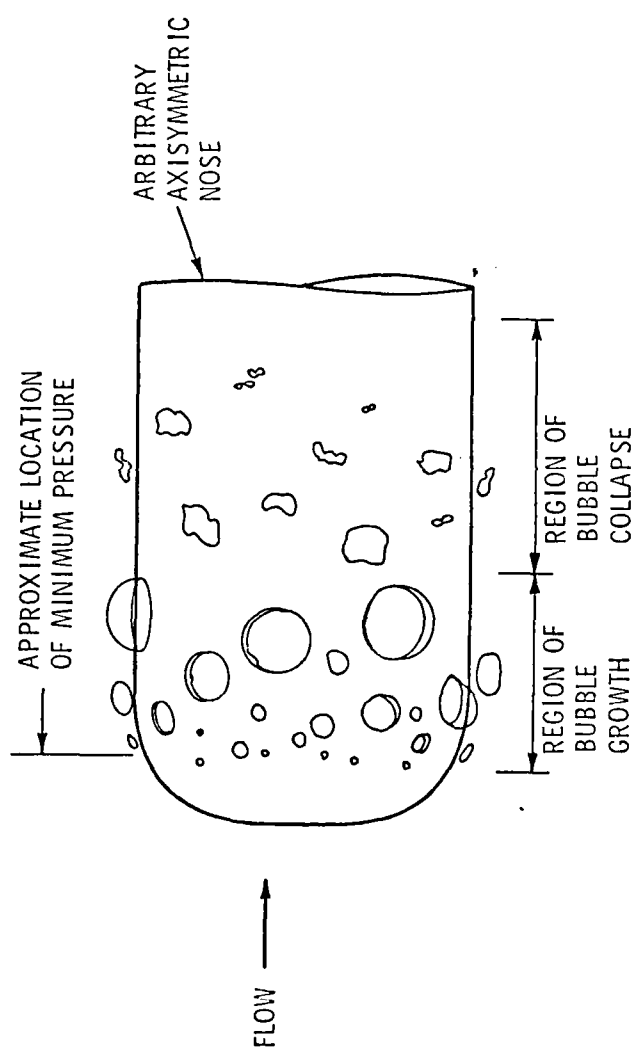


Figure 16. Sketch of travelling-bubble cavitation on an arbitrary axisymmetric nose.

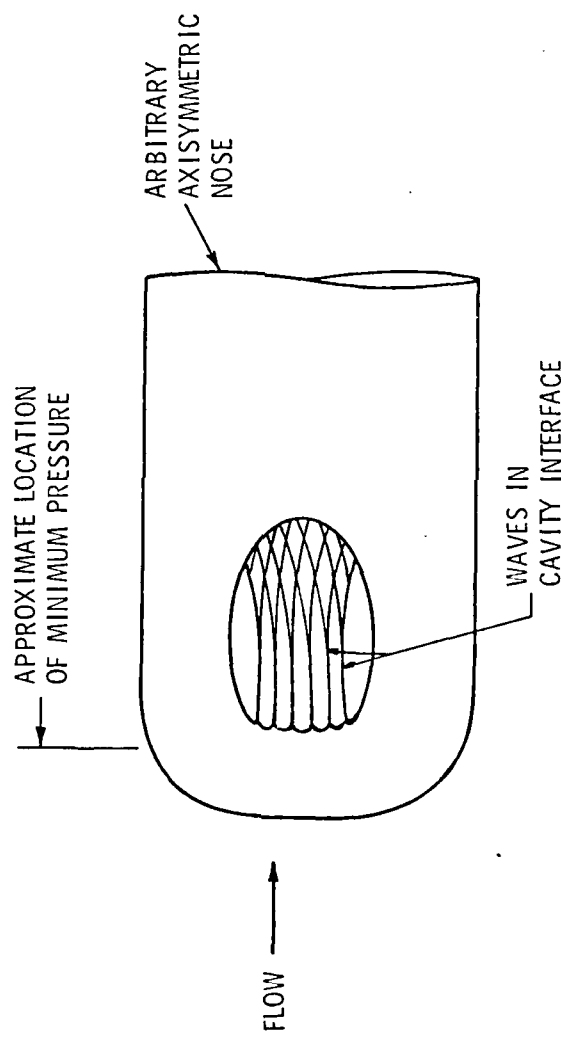


Figure 17. Sketch of travelling-patch cavitation on an arbitrary axisymmetric nose.

uniformly about the body a short distance downstream from the minimum pressure point. The cavity leading edge is located very near to the site of laminar boundary layer separation. The front portion of band cavitation generally appears to be transparent and divided into sections by thin liquid partitions running parallel with the flow. These walls continually shift within the cavity. Just downstream of the clear-walled portion, the cavity surface becomes wavy and breaks up into myriads of frothy bubbles. A sketch of typical band cavitation as it appears on an arbitrary headform is presented in Figure 18.

Fixed-patch cavities are similar in appearance to the cavities described in travelling-patch cavitation. A fixed-patch, however, appears to be attached to the model surface at one or more points on the upstream end of the cavity. From the attachment point(s), the cavity fans out symmetrically in the downstream direction and terminates in a myriad of frothy bubbles which trail off downstream. The front portion of the cavity close to the vertex is transparent as with band cavitation. The downstream portion of the cavity appears to be translucent with wave patterns in the cavity surface. A sketch illustrating the details of fixed-patch cavitation on an arbitrary headform is presented in Figure 19.

Developed cavitation is different from the other forms of attached cavitation because of its relatively large size. The presence of a developed cavity on a hydrodynamic body significantly changes the noncavitating flow characteristics. The leading edge of the cavity is generally located near the site of minimum pressure about the body. The length of a developed cavity at inception or desinence may vary

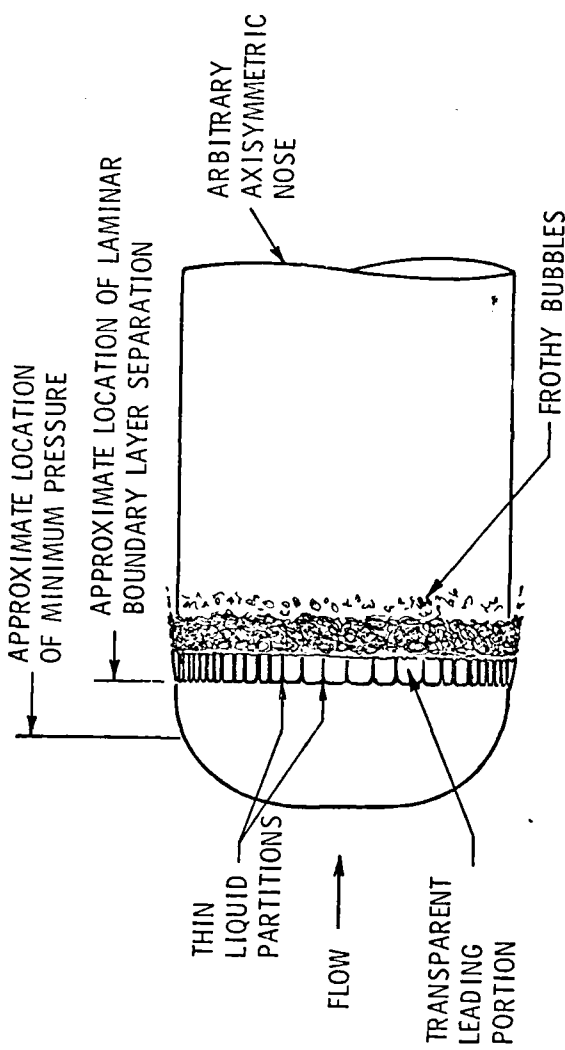


Figure 18. Sketch of band cavitation on an arbitrary axisymmetric nose.

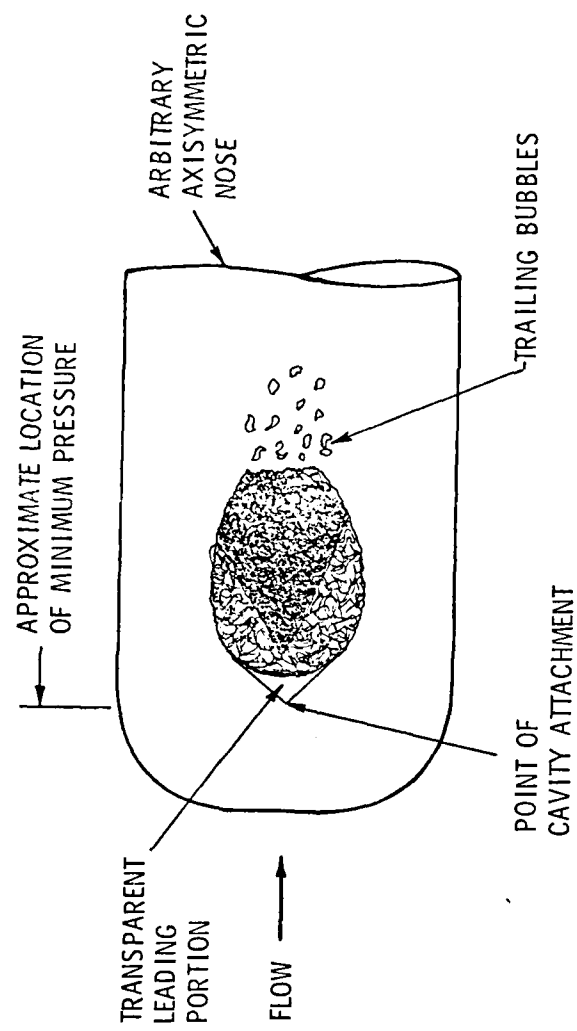


Figure 19. Sketch of fixed-patch cavitation on an arbitrary axisymmetric nose.

from one to several body diameters. A sketch of a typical developed cavity on an arbitrary headform is presented in Figure 20.

4.2 Presentation of Results from Cavitation Observations

4.2.1 Hemispherical nose. Three types of cavitation were observed on the hemispherical nose. Transient cavitation in the forms of travelling-bubble and bubble-ring cavitation and attached cavitation in the form of band cavitation were noted for varying values of free stream velocity, air content, and cavitation number.

4.2.1.1 Transient cavitation. Travelling-bubble cavitation on the hemispherical nose occurred at the lower free stream velocities of 20.0 to 50.0 fps. The rate of cavitation occurrences increased significantly as the velocity was decreased. The number and size of free stream bubbles in the test section also increased as the velocity and static pressure of the tunnel were lowered. Desinent cavitation data are presented in Figure 21 for total air contents of 7.8 and 11.0 ppm. Preliminary tests showed that hysteresis effects on travelling-bubble cavitation were not significant. It is apparent from these plots that travelling-bubble cavitation is quite sensitive to total air content. It is interesting to note that the desinent cavitation number, σ_d , shows a definite decreasing trend with an increase in free stream velocity. This form of cavitation is accompanied by distinct snapping sounds which are apparently caused by the individual cavities collapsing once they enter regions of higher pressure. A photograph of travelling-bubble cavitation on a hemispherical nose is presented in Figure 22. Here, the free stream velocity is 30 fps, the

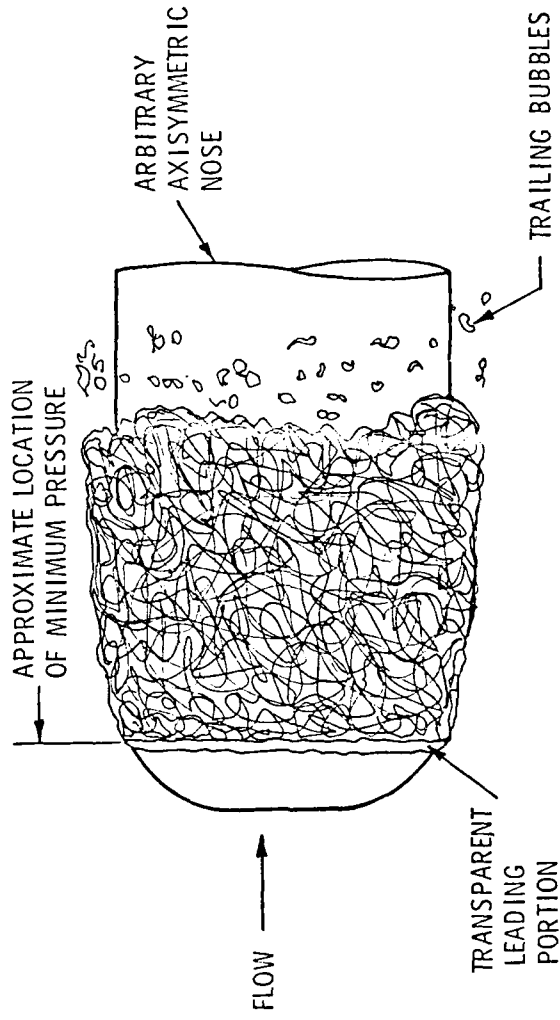


Figure 20. Sketch of developed cavitation on an arbitrary axisymmetric nose.

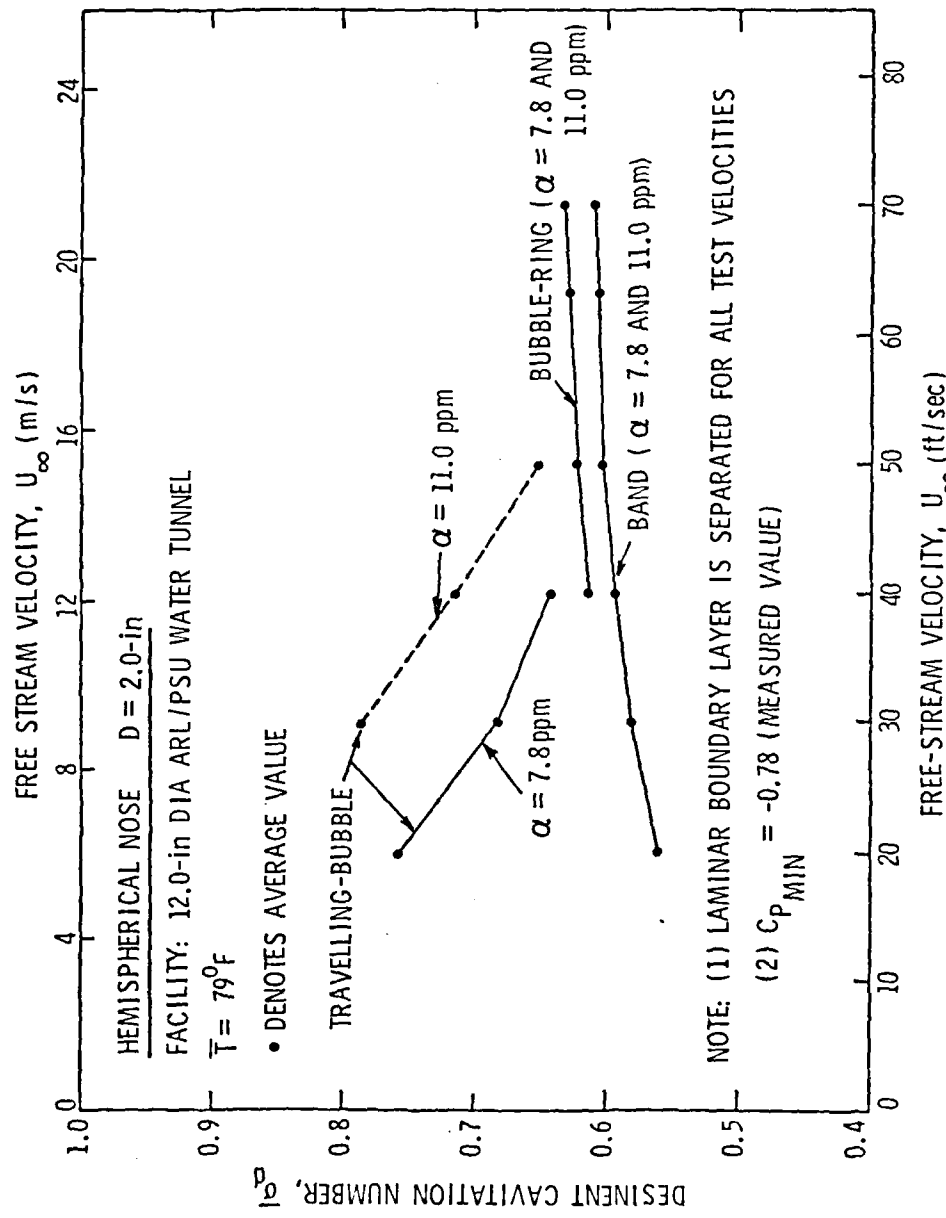


Figure 21. Limited cavitation data versus U_{∞} for various types of cavitation on a 2.0-in. diameter hemispherical nose for two values of air content.



Figure 22. Photograph of travelling-bubble cavitation on the hemispherical nose. Laminar boundary layer separation is present. ($U_{\infty} = 30.0$ fps, $\sigma = 0.577$, $\alpha = 9.2$ ppm)

cavitation number is 0.577, and the air content is 9.2 ppm. Several travelling bubbles can be seen very near to the model surface.

A second type of transient cavitation observed on the hemispherical nose is bubble-ring cavitation. Bubble-ring cavitation generally occurs at higher free stream velocities (40.0 to 70.0 fps). It appears as macroscopic, irregularly shaped bubbles which rapidly appear and disappear within a very narrow region around the headform in the vicinity of boundary layer reattachment. Under normal lighting, this type of cavitation appears as a fuzzy ring fixed on the model. A photograph of bubble-ring cavitation on the hemispherical nose is presented in Figure 23 for a free stream velocity of 60.0 fps, a cavitation number of 0.626, and an air content of 9.5 ppm. Desinent cavitation data for bubble-ring cavitation are also presented in Figure 21 for air contents of 7.8 and 11.0 ppm. Variation in air content from 7.8 to 11.0 ppm showed very little effect on desinent cavitation numbers. For very low air contents (less than 4.0 ppm), however, bubble-ring cavitation was not observed. A slight increasing trend in σ_d for increasing free stream velocity was noted.

4.2.1.2 Attached cavitation. Attached cavitation occurred on the hemispherical nose in the form of well-defined band cavitation. Generally, band cavitation is the only type of attached cavitation observed on the hemispherical nose except for occasional fixed-patch cavitation attributed to dirt on the model surface. A photograph of band cavitation on a hemispherical nose is presented in Figure 24. The free stream velocity is 60.0 fps, the cavitation number is 0.61, and the air content is 9.2 ppm. Typical desinent cavitation data for



Figure 23. Photograph of bubble-ring cavitation on the hemispherical nose. Laminar boundary layer separation is present. ($U_{\infty} = 60.0$ fps, $\sigma = 0.626$, $c_i = 9.2$ ppm)

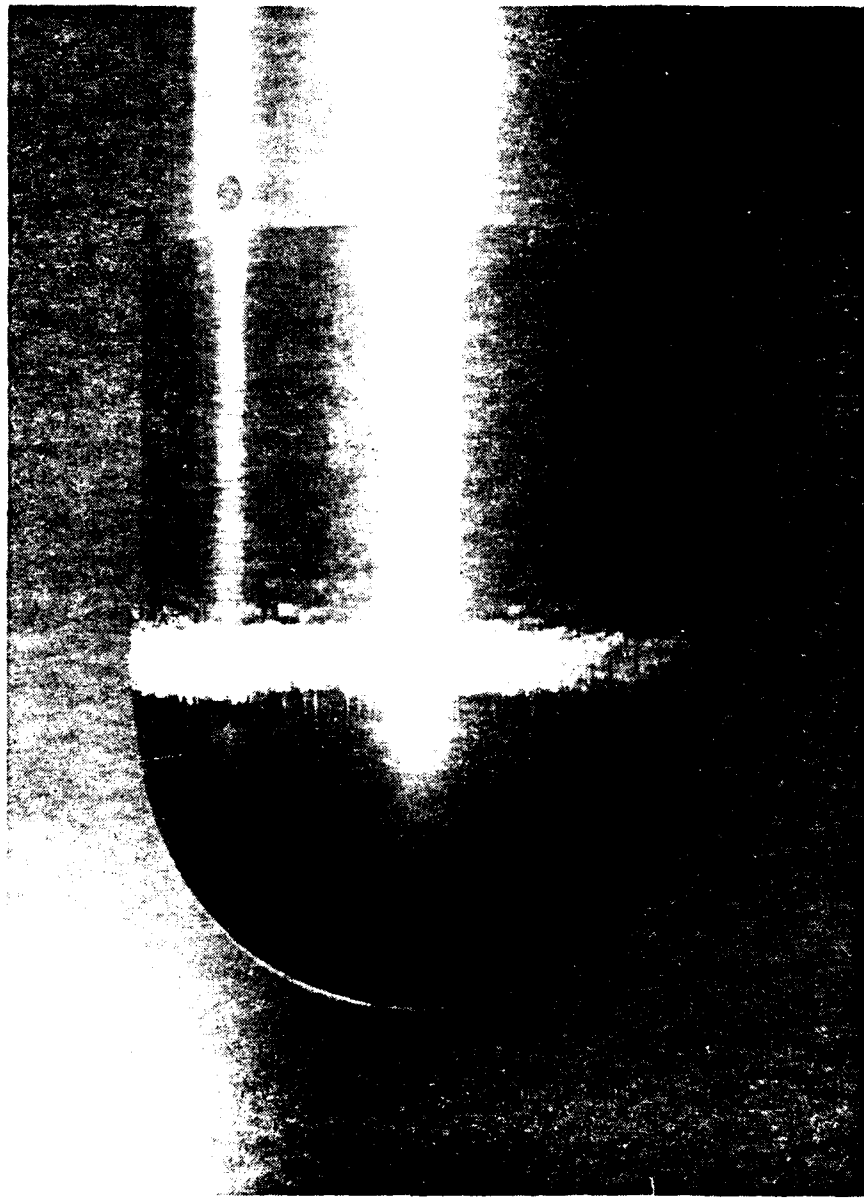


Figure 24. Photograph of band cavitation on the hemispherical nose. Laminar boundary layer separation is present. ($U_{\infty} = 60.0$ fps, $\sigma = 0.610$, $\alpha = 9.2$ ppm)

band cavitation are presented in Figure 21 for air contents of 7.8 and 11.0 ppm. A very slight increase is observed in σ_d with increase in velocity. The trends in σ_d with free stream velocity for both band cavitation and bubble-ring cavitation are nearly identical. Desinent cavitation numbers for band cavitation appear to be nearly insensitive to air content. Hysteresis effects on band cavitation are considered to be insignificant for normal values of air content. At low air content, however, particularly when bubble-ring cavitation has been suppressed, hysteresis on band cavitation becomes quite evident.

Limited bubble-ring cavitation occurs at cavitation numbers slightly higher than for limited band cavitation. When bubble-ring cavitation is initially established around the headform, a slight lowering of pressure will cause a gradual transformation from bubble-ring cavitation into band cavitation. A photograph showing this transformation is presented in Figure 25. Here, the upper portion of the model has band cavitation and the lower portion has bubble-ring cavitation. The sequence of events observed for transforming bubble-ring cavitation into band cavitation in an inception test is the reverse of that observed in a desinence test. The initial presence of bubble-ring cavitation during a run assures the gradual development of band cavitation. On the other hand, if no bubble-ring cavitation occurs first, then band cavitation may either develop gradually or suddenly as a well-developed cavity. This often occurs for low values of air content.

Band cavitation is also influenced by the presence of travelling-bubble cavitation. If a large number of bubbles pass over the nose

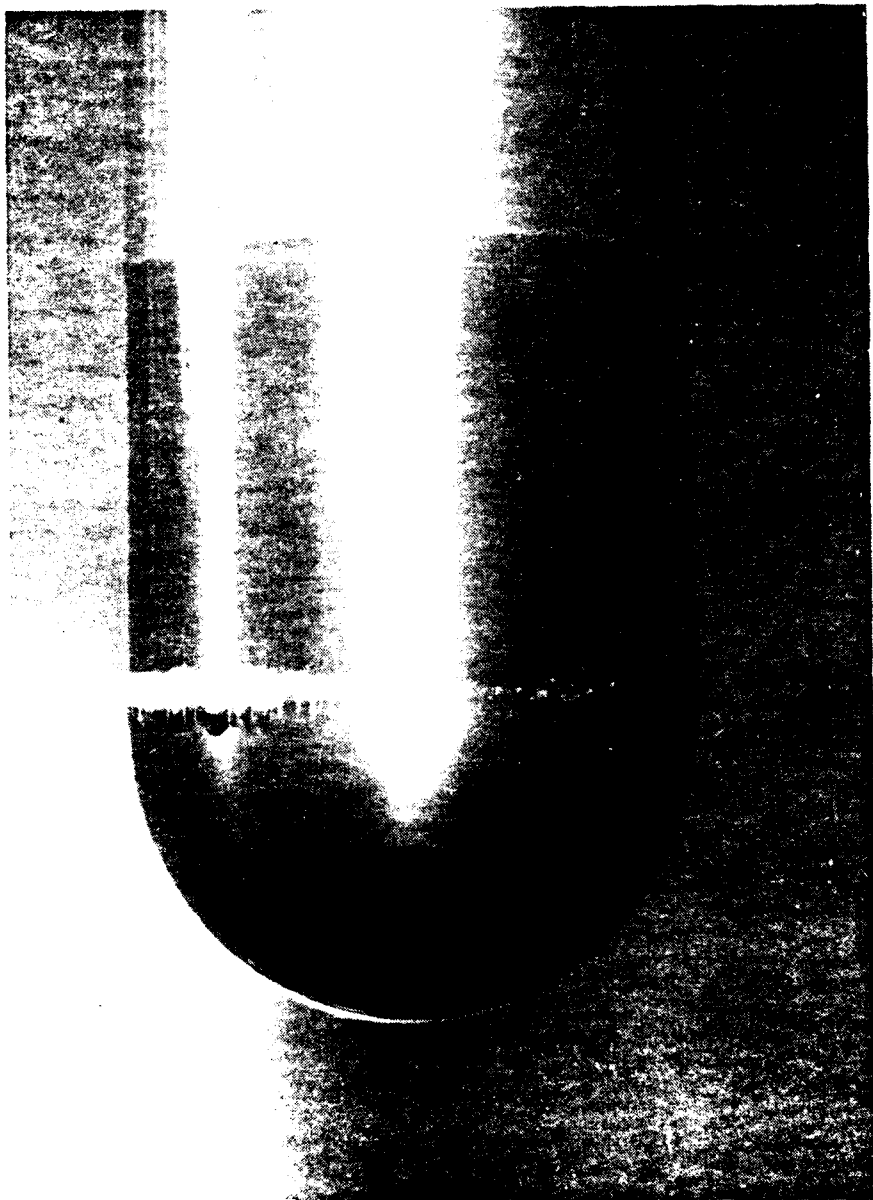


Figure 25. Photograph showing bubble-ring cavitation and band cavitation on the hemispherical nose. ($U_{in} = 60.0$ fps, $\sigma = 0.615$, $\alpha = 9.2$ ppm)

when band cavitation is present, the band has been observed to vanish and only travelling-bubble cavitation is left. Three photographs showing this sequence of events are presented in Figures 26(a), (b), and (c). Figure 26(a) shows an increase in the number of travelling bubbles. The third photograph, Figure 26(c), taken at a slightly lower pressure, shows that band cavitation has been eliminated and only myriads of travelling bubbles are left. This sequence was taken at a free stream velocity of 30 fps.

4.2.1.3 Effect of a boundary layer trip on cavitation characteristics. As shown previously by Arakeri and Acosta [16], the placement of a boundary layer trip on the hemispherical nose resulted in a drastic change in the cavitation characteristics of this body. By placing a thin (0.007-in.) wax trip on the model at about 30° from stagnation, the boundary layer was energized enough to prevent laminar boundary layer separation. The trip was effective for free stream velocities of about 35.0 fps and higher. With separation fully eliminated, neither bubble-ring cavitation nor band cavitation was observed on the model. Transient cavitation, mostly in the form of travelling bubbles, was the only form of cavitation observed on the fully tripped hemispherical nose. Figure 27 shows some large travelling bubbles sweeping over a fully tripped hemispherical model at the relatively low cavitation number of 0.266. The free stream velocity is 40.0 fps, and the air content is 4.0 ppm. To emphasize the effectiveness of tripping the boundary layer, the lower half portion of the trip was removed from the model. The result is shown in Figure 28. Here a large band cavity is observed on the bottom half of the model



Figure 26. Sequence of photographs illustrating the elimination of band cavitation by the presence of travelling-bubbles on the hemispherical nose.
(a) Band cavitation with traces of travelling bubble cavitation.
($U_{\infty} = 30.0$ fps, $\sigma = 0.46$, $\alpha = 9.0$ ppm)



Figure 26 (b). Band cavitation with increasing amount of travelling-bubble cavitation.
($U_{\infty} = 30.0$ fps, $\sigma = 0.46$, $\alpha = 9.0$ ppm)



Figure 26 (c). Advanced travelling-bubble cavitation. Band cavitation has been eliminated. ($U_{\infty} = 30.0$ fps, $\sigma = 0.32$, $\alpha = 9.0$ ppm)

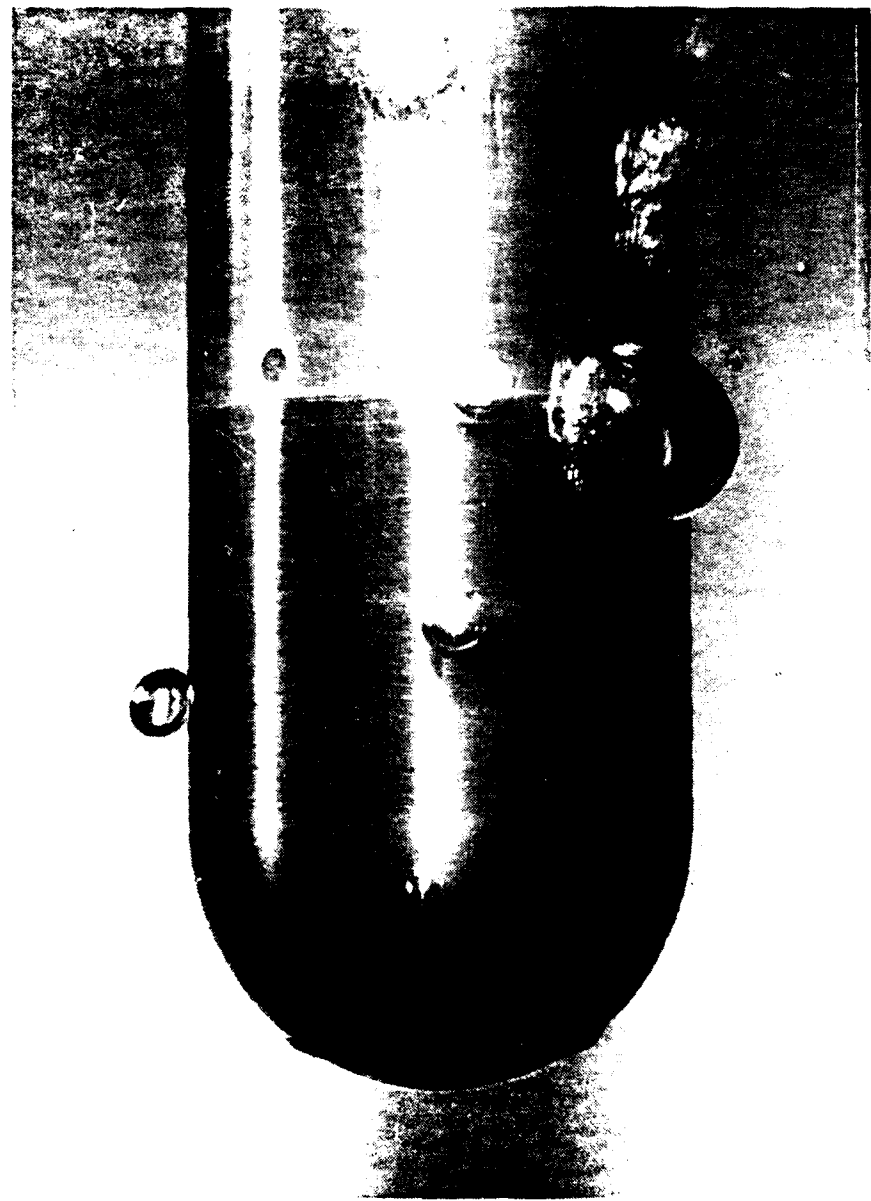


Figure 27. Photograph of travelling-bubble cavitation on the tripped hemispherical nose.
Laminar boundary layer separation has been eliminated. ($U_{\infty} = 40.0$ fps,
 $\sigma = 0.266$, $\alpha = 4.0$ ppm)



Figure 28. Photograph illustrating the effect of a boundary layer trip on the cavitation characteristics of a hemispherical nose. Only the upper portion of the nose is tripped. ($U_{\infty} = 60.0$ fps, $\sigma = 0.382$, $\alpha = 4.0$ ppm)

where the boundary layer is not tripped and presumably separating. On the upper tripped portion of the model, no cavitation is seen whatsoever. Occasionally, travelling bubbles appeared on the upper portion of the model, but no attached cavities were observed. The free stream velocity is 60.0 fps, the cavitation number is 0.382, and the air content is 4.0 ppm. Limited cavitation data were not obtained for the tripped hemispherical nose. However, it is strongly suspected that, with the trip, limited cavitation data would exhibit the same trends as transient cavitation on a body whose cavitation characteristics are not governed by laminar boundary layer separation.

4.2.2 Schiebe nose. Four different types of cavitation were observed on the Schiebe nose. Two distinctly different forms of transient cavitation were noted, namely, travelling-bubble cavitation and travelling-patch cavitation. Attached cavitation appeared in the form of fixed-patch cavitation and the extreme case of developed cavitation. Cavitation number data are presented in Figure 29, and photographs are shown in Figures 30 to 34.

4.2.2.1 Transient cavitation. Both transient forms of cavitation (travelling-bubble and travelling-patch cavitation) generally appeared simultaneously on this model. It was noted, however, that travelling-patch cavitation appeared to be predominant at high velocities. At low velocities, travelling bubbles were much more numerous. Both types are significantly affected by air content and increase in abundance with increased air content. Figure 30 shows a photograph of a travelling-bubble and a travelling-patch cavitation occurring simultaneously on the Schiebe nose. The free stream

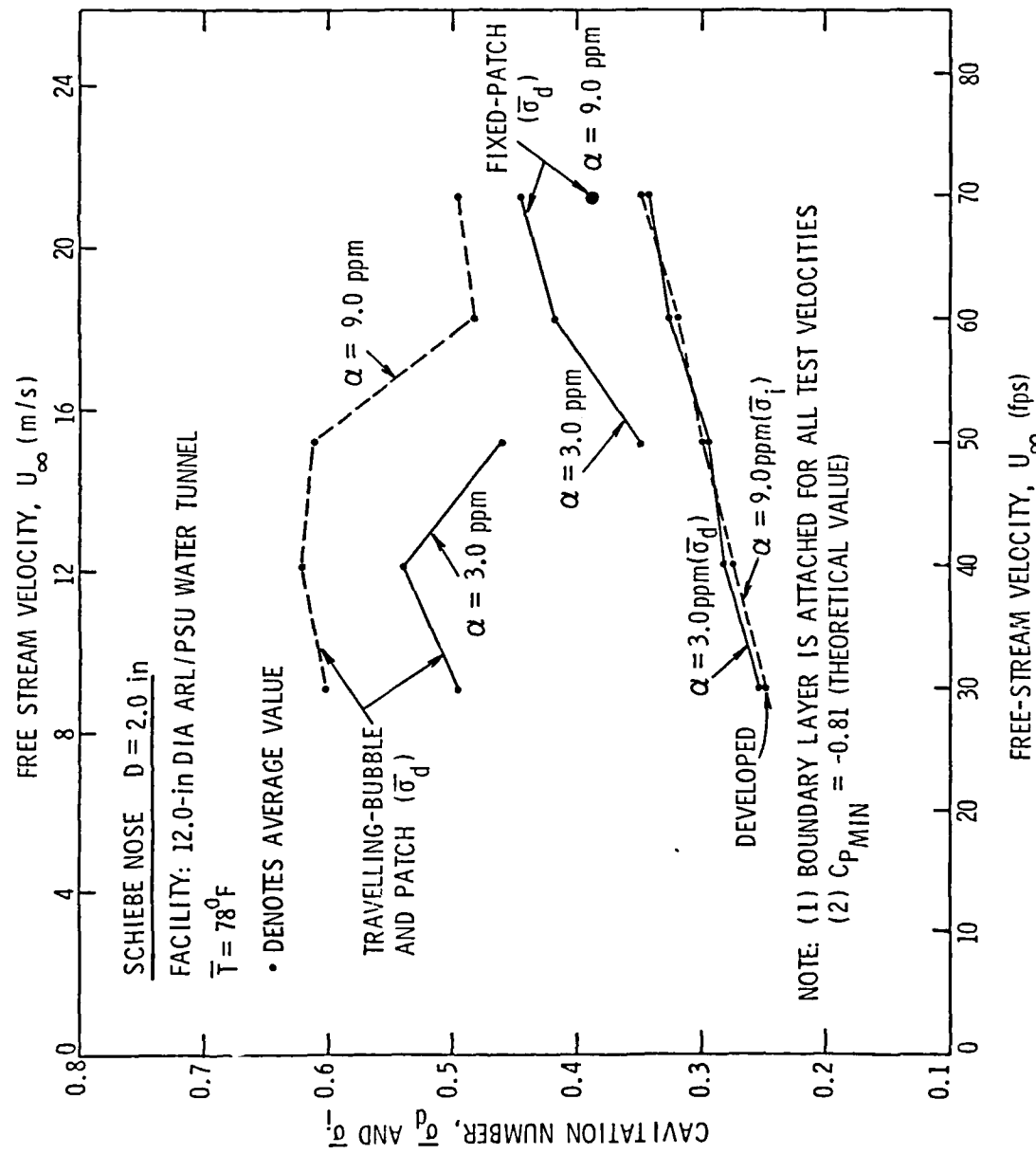


Figure 29. Limited cavitation data versus U_∞ for various types of cavitation on a 2.0-in. diameter Schieber nose for two values of air content.



Figure 30. Photograph of two types of transient cavitation on the Schiebe nose.
Above is a travelling bubble and below is a travelling patch.
($U_{\infty} = 60.0$ fps, $\sigma = 0.365$, $\alpha = 9.0$ ppm)



Figure 31. Photograph of a travelling bubble with small lateral tails observed on the Schiebe nose. ($U_{\infty} = 40.0$ fps, $\sigma = 0.368$, $\alpha = 9.0$ ppm)



Figure 32. Photograph of a travelling bubble with large lateral tails which appear to merge together (lower center) on the Schiebe nose. Above is a fixed patch and below is a travelling patch. ($U_{\infty} = 60.0$ fps, $\sigma = 0.336$, $\alpha = 9.0$ ppm)



Figure 33. Photograph of fixed-patch cavitation (three cavities) on the Schiebe nose. ($U_{\infty} = 60.0$ fps, $\sigma = 0.361$, $\alpha = 4.0$ ppm)



Figure 34. Photograph of developed cavitation on the Schiebe nose.
($U_{\infty} = 60.0$ fps, $\sigma = 0.355$, $\alpha = 9.0$ ppm)

velocity is 60.0 fps, the cavitation number is 0.365, and the air content is 9.0 ppm. Desinent cavitation data are presented collectively for both types of transient cavitation in Figure 29 for air contents of 3.0 and 9.0 ppm. Both curves indicate a decreasing trend in σ_d with free stream velocity. Also quite evident is the effect of air content on this form of cavitation.

Observations of an intermediate form of transient cavitation suggest that travelling-patch cavitation is actually a further developed form of travelling-bubble cavitation. Occasionally, travelling bubbles were observed to have two lateral tails which trailed behind the bubble. Closer inspection of the video tapes revealed an entire spectrum of travelling bubbles having progressively more developed tails. Apparently, a travelling patch is one in which the tails are quite large and have merged together. Figure 31 shows a photograph of a large travelling bubble with two small tails occurring on the Schiebe nose. Figure 32 shows a photograph of what appears to be a travelling bubble whose tails are quite large and appear to have merged together. Its appearance begins to resemble that of a travelling-patch cavity as shown in Figure 30. Also in the photograph (Figure 32) is a fixed-patch cavity on top of the body and a travelling-patch cavity on the underside. The cavitation numbers for Figures 31 and 32 are 0.365 and 0.336, respectively. For both cases, the free stream velocity is 60.0 fps and the air content is 9.0 ppm.

4.2.2.2 Attached cavitation. As mentioned previously, attached cavitation on the Schiebe nose appeared in the form of

fixed-patch cavitation and, for low cavitation numbers, as developed cavitation. Fixed-patch cavitation on the Schiebe nose was generally observed for higher free stream velocities of 50.0 to 70.0 fps. For low air content (about 3.0 ppm), fixed-patch cavities would appear evenly arranged about the circumference of the model. In desinence, the cavities were observed to shrink with increasing pressure to a streamwise length of approximately 0.5 body diameters and then disappear. For higher air contents (about 9.0 ppm), the cavities appeared to be much more unstable and continually shifted to different positions around the circumference of the body. In desinence, the cavities did not appear to shrink as much as for the case of higher air content before disappearing. At this higher air content, fixed-patch cavitation was observed only at the free stream velocity of 70.0 fps. Desinent cavitation data for fixed-patch cavitation on the Schiebe nose is presented in Figure 30 for air contents of 3.0 and 9.0 ppm. A definite increasing trend in σ_d with increase in free stream velocity is noted. It is also apparent that σ_d decreases with an increase in air content. A photograph of fixed-patch cavitation on the Schiebe nose is presented in Figure 33. Three cavities arranged evenly about the circumference of the body are shown. Here, the free stream velocity is 60.0 fps, the cavitation number is 0.361, and the air content is 4.0 ppm.

The second form of attached cavitation observed on the Schiebe nose is that of developed cavitation. This type of cavitation has been observed to form gradually when either fixed-patch cavitation merges together or myriads of transient cavities coalesce. Developed cavitation may also appear very suddenly in the absence of any

precursor cavities. This appearance is usually at low air contents and is accompanied by considerable hysteresis effects. A photograph of developed cavitation on the Schiebe nose is presented in Figure 34 for a free stream velocity of 60.0 fps, a cavitation number of 0.355, and an air content of 9.0 ppm. Desinent cavitation data are presented in Figure 29 for air contents of 3.0 and 9.0 ppm. The desinent cavitation number increases strongly with free stream velocity, but is not affected by air content.

4.2.3 DTNSRDC nose

4.2.3.1 Transient cavitation. Both forms of transient cavitation, namely, travelling-bubble cavitation and travelling-patch cavitation, were observed on the DTNSRDC nose. As with the Schiebe nose, travelling-patch cavitation was more abundant at high velocities and travelling bubbles prevailed at low velocities. Travelling bubbles with lateral tails, believed to be underdeveloped travelling patches as described earlier, were also observed on the DTNSRDC nose. No differences were noted in the transient cavitation characteristics between subcritical separating flow and supercritical nonseparating flow for the DTNSRDC nose. Figure 35 shows a photograph of profuse travelling-bubble cavitation on the DTNSRDC nose for a free stream velocity of 25.0 fps, a cavitation number of 0.573, and an air content of 9.0 ppm. In a photograph of the DTNSRDC nose, Figure 36, is shown a travelling bubble with two large lateral tails and a regular travelling bubble below it. The free stream velocity is also 25.0 fps, the cavitation number is 0.355, and the air content is 4.0 ppm. Figure 37 is a photograph of a travelling patch and a small travelling bubble on



Figure 35. Photograph of travelling-bubble cavitation on the DTNSRDC nose.
($U_{\infty} = 25.0$ fps, $\sigma = 0.573$, $\alpha = 9.0$ ppm)



Figure 36. Photograph of a travelling bubble with lateral tails on the DTNSRDC nose. A travelling bubble is also present. ($U_{\infty} = 25.0$ fps, $\sigma = 0.355$, $\alpha = 4.0$ ppm)

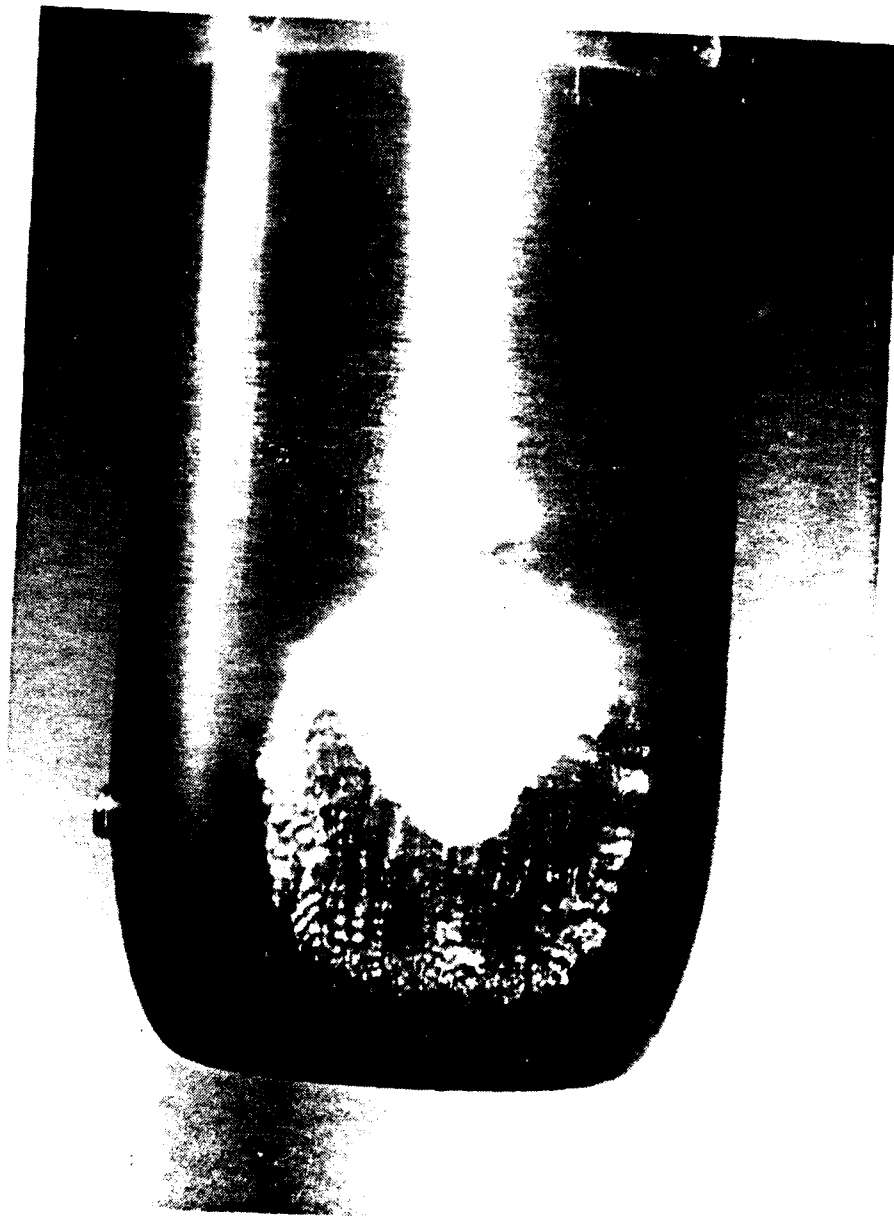


Figure 37. Photograph of two types of transient cavitation on the DTNSRDC nose. The large cavity is a travelling patch. At top is a travelling bubble. ($U_{\infty} = 50.0$ fps, $\sigma = 0.525$, $\alpha = 9.0$ ppm)

the DTNSRDC nose for a free stream velocity of 50.0 fps, a cavitation number of 0.525, and an air content of 9.0 ppm. Desinent cavitation data for transient cavitation on the DTNSRDC nose are presented collectively in Figure 38 for air contents of 3.0 and 8.0 ppm. As with the Schiebe nose and the hemispherical nose, these data show a decreasing trend with an increase in free stream velocity and a strong correlation with air content.

4.2.3.2 Attached cavitation. All cavitation types observed on the DTNSRDC nose were the same as those observed on the Schiebe nose with the addition of band cavitation which occurred on the DTNSRDC nose at low free stream velocities. At 25.0 and 30.0 fps, band cavitation was observed well downstream on the DTNSRDC nose near the theoretically determined location of laminar boundary layer separation. The appearance of band cavitation on the DTNSRDC nose was much more unstable and not as well defined as band cavitation on the hemispherical nose. Also, bubble-ring cavitation which often preceded band cavitation on the hemispherical nose was not observed on the DTNSRDC nose. A photograph of band cavitation on the DTNSRDC nose is presented in Figure 39 for a free stream velocity of 25.0 fps, a cavitation number of 0.305, and a air content of 4 ppm. Desinent cavitation data are given in Figure 38 for air contents of 3.0 and 8.0 ppm. No trend in σ_d with velocity could be determined because of the limited free stream velocity range. Desinent cavitation numbers appear to decrease slightly with increased air content. For high air content, when many free stream bubbles were present, transient cavitation was abundant and no band cavitation was observed. As described earlier, this situation

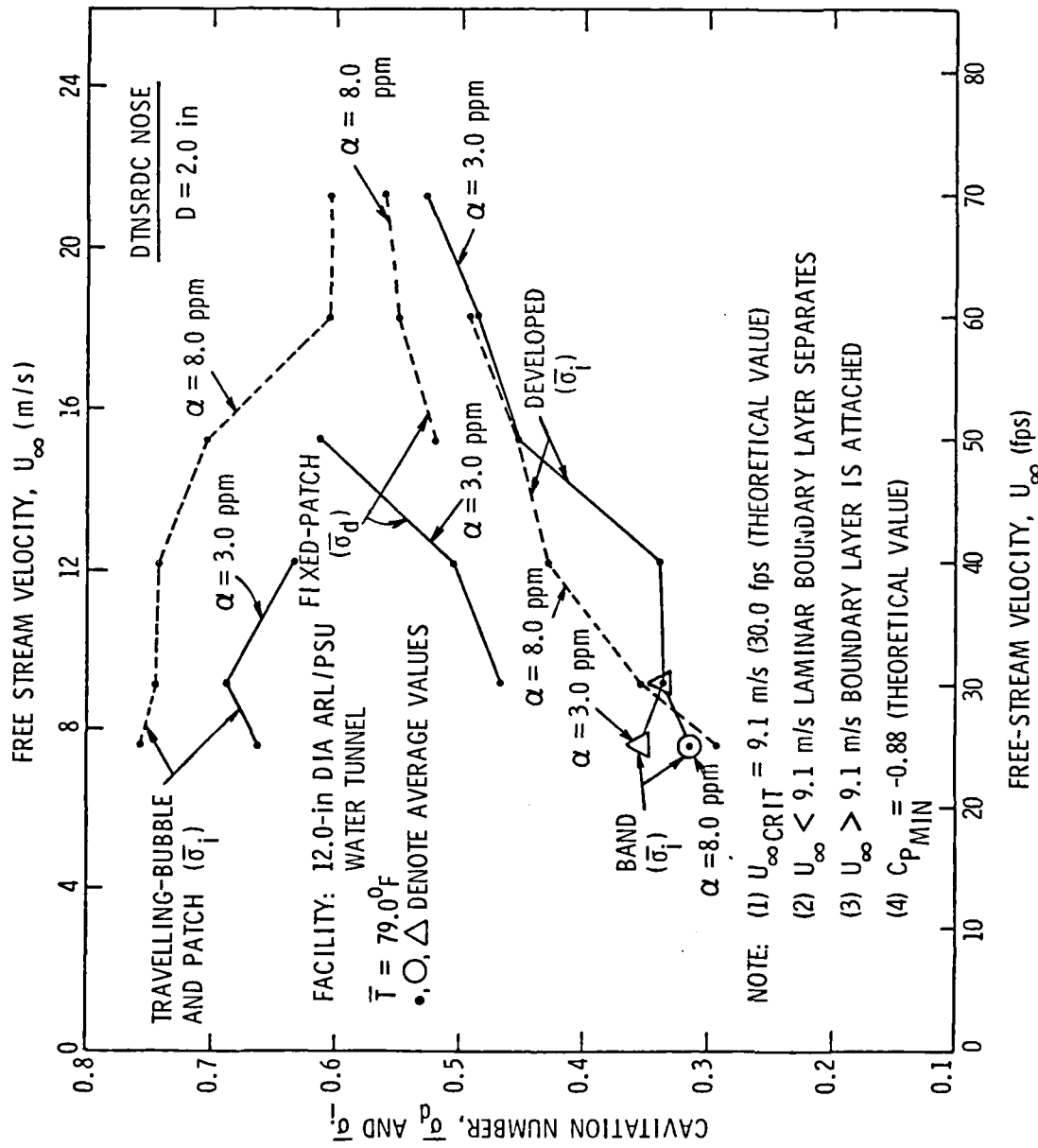


Figure 38. Limited cavitation data versus U_{∞} for various types of cavitation on a 2.0-in. diameter DTNSRDC nose for two values of air content.



Figure 39. Photograph of band cavitation on the DTNSRDC nose. Laminar boundary layer separation is present. ($U_{\infty} = 25.0$ fps, $\sigma = 0.305$, $\alpha = 4.0$ ppm)

may be similar to the elimination of band cavitation by the presence of transient cavitation on the hemispherical nose.

Other types of attached cavitation on the DTNSRDC nose included fixed-patch cavitation and developed cavitation. The appearance and characteristics of these two types of cavitation were essentially the same as those observed on the Schiebe nose. A photograph of fixed-patch cavitation on the DTNSRDC nose is presented in Figure 40.

Several cavities are shown to be positioned evenly around the circumference of the model. The free stream velocity is 60.0 fps, the cavitation number is 0.546, and the air content is 4.0 ppm. Fixed-patch cavitation was somewhat more predominant on the DTNSRDC nose than on the Schiebe nose under similar test conditions. Desinent cavitation data for fixed-patch cavitation on the DTNSRDC nose are presented in Figure 38. As on the Schiebe nose, the desinent cavitation number increased strongly with velocity and decreased with increased air content. Fixed-patch cavitation appeared to be somewhat more stable for higher velocities. For low air contents fixed-patch cavitation was able to persist at lower velocities. Free stream bubbles and transient cavitation appeared to cause fixed-patch cavitation to become unsteady and to shift erratically about the model.

A photograph of developed cavitation on the DTNSRDC nose is presented in Figure 41 for a free stream velocity of 40.0 fps, a cavitation number of 0.412, and an air content of 9.0 ppm. Desinent cavitation data are presented in Figure 38. The desinent cavitation number increases strongly with velocity, but shows little change with variation in air content.

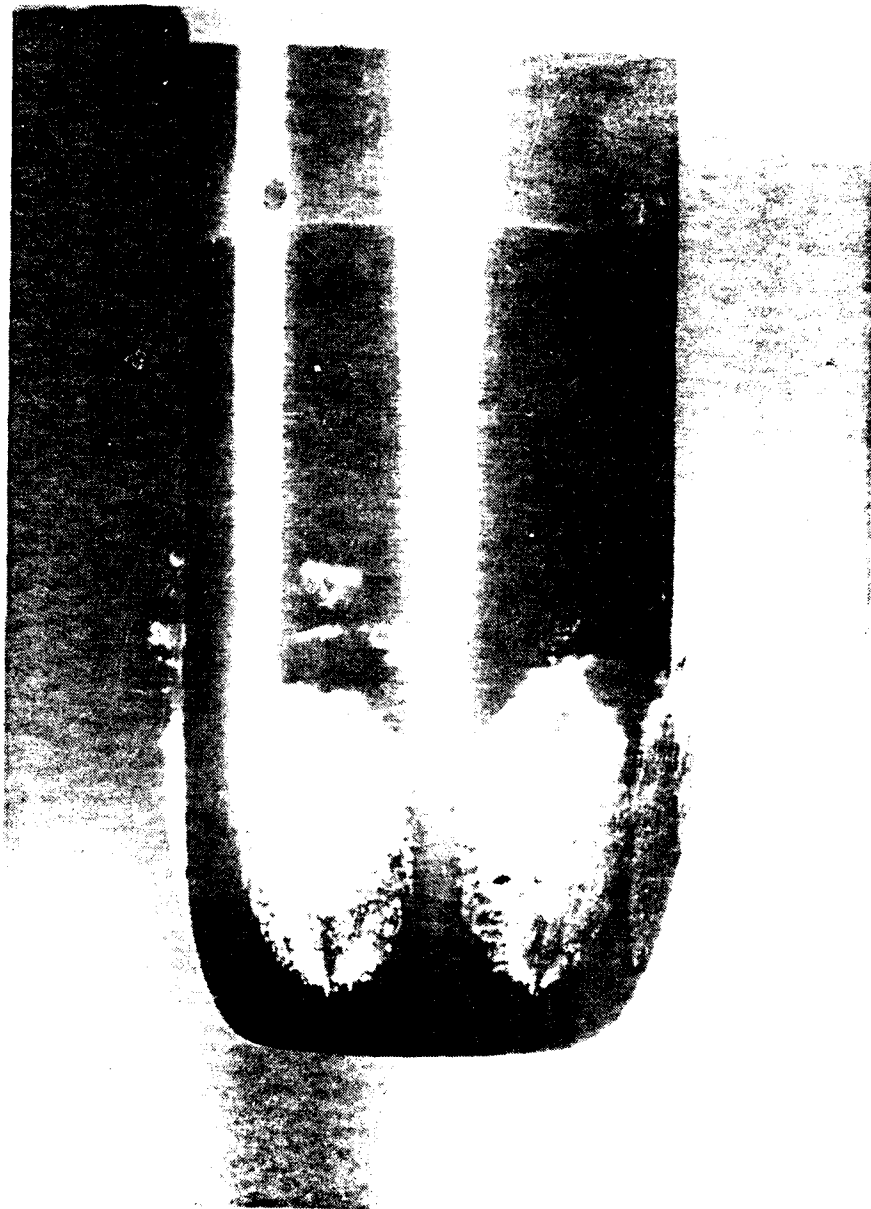


Figure 40. Photograph of fixed-patch cavitation (four cavities) on the DTNSRDC nose. ($U_{\infty} = 60.0$ fps, $\sigma = 0.412$, $\alpha = 9.0$ ppm)

AD-A104 779

PENNSYLVANIA STATE UNIV UNIVERSITY PARK APPLIED RESE--ETC F/6 20/4
OBSERVATIONS OF THE EFFECTS OF BOUNDARY LAYER AND NUCLEI ON CAV--ETC(U)
FEB 81 J A CARROLL
N00024-79-C-6043

UNCLASSIFIED

2 or 3
ARL
ARL0479

PLA
P
S

NL

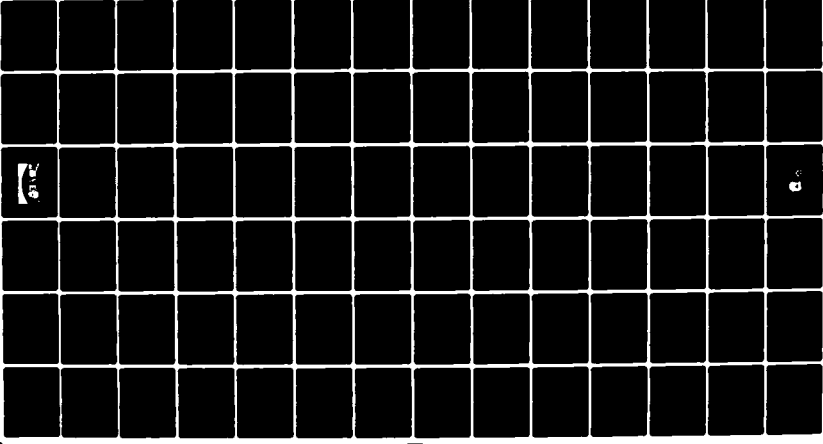




Figure 41. Photograph of developed cavitation of the DTNSRDC nose.
($U_{\infty} = 40.0$ fps, $\sigma = 0.412$, $\alpha = 9.0$ ppm)

CHAPTER 5

DISCUSSION OF CAVITATION OBSERVATIONS

5.1 Travelling Cavitation

Travelling cavitation was the most commonly observed form of cavitation in the present investigation. Several notable characteristics are listed below:

1. Travelling cavitation showed no apparent correlation with a particular boundary layer status (i.e., separated, attached, laminar, or turbulent). This type of cavitation was observed on all three models in the present investigation.
2. The value of the limited cavitation number, σ_ℓ , for travelling cavitation was significantly influenced by air content. Particularly at low velocities, increasing the air content may raise σ_ℓ to a value approaching $|C_{P_{min}}|$ of the body.
3. The value of σ_ℓ for travelling cavitation was observed to decrease with an increase in free stream velocity in most cases.
4. Two different types of travelling cavitation were observed, namely, travelling-bubble and travelling-patch cavitation. Travelling-bubble cavitation predominated at limited cavitation conditions corresponding to low free stream velocities. At these low velocities, for values of σ less than σ_ℓ , travelling-patch cavitation was observed. As free stream velocity was increased, σ_ℓ for travelling cavitation was shown to decrease. At limited cavitation conditions

corresponding to higher velocities and lower values of σ_ℓ , travelling-patch cavitation predominated.

5.1.1 Characteristics. The observed characteristics of travelling cavitation in the present investigation are consistent with the work of Schiebe [20], who reports that the formation of travelling cavitation is largely controlled by the number and size of nuclei in the free stream. A similar conclusion is reported by Gates [13]. Therefore, if the nuclei population of two water tunnel facilities are very different, then one could expect to see differences between the travelling cavitation on the same model when tested in both facilities. In particular, differences should be evident in the results of cavitation tests performed in tunnel facilities with and without resorbers. A very important example is the High Speed Water Tunnel facility at the California Institute of Technology. This tunnel is equipped with a resorber to minimize the amount of free gas in the water. It is interesting to note that travelling cavitation is seldom observed in this facility [10].

The fact that σ_ℓ for travelling cavitation approaches $|C_{p_{\min}}|$ for increasing air content (or increase in nuclei population) is also reported by Gates [13]. In his investigation, an increase in the free-gas content (total gas content remaining constant) resulted in an increase in the incipient cavitation number. Arakeri and Acosta [15] gave similar results for their electrolysis tests on an ITTC nose. By providing cavitation nuclei through electrolysis, they were able to produce cavitation at a cavitation number significantly greater than σ_ℓ but less than $|C_{p_{\min}}|$.

The decreasing trend in σ_ℓ with free stream velocity for travelling cavitation is consistent with the results reported by both Van der Meulen [17], who tested a 10-mm (0.394-in.) diameter Schiebe nose, and Schiebe [20], from tests on a 0.625-in. diameter ITTC nose. Brockett [21] reported a slight increasing trend in σ_ℓ with velocity for travelling cavitation on a 2.0-in. diameter DTNSRDC nose. His data, however, covered the very small free stream velocity range of 15.0 to 24.0 fps. A larger variation in free stream velocity would have, perhaps, produced data showing the reverse trend.

5.1.2 Estimates for free stream nuclei size. Travelling cavitation occurs as the result of nuclei in the free stream. The tendency of a nucleus to cavitate is determined largely by the cavitation number, σ , and the initial radius, R_0 . Consider a bubble which is in static equilibrium with the liquid around it. The internal pressure, due to the vapor of the liquid and the noncondensable gasses, is balanced by the external pressure, due to surface tension and local ambient pressure. The resulting equilibrium equation for a bubble in a liquid is

$$P_v + P_G = \frac{2\gamma}{R} + P_L , \quad (6)$$

where

P_v = vapor pressure inside the bubble,

P_G = pressure of any noncondensable gasses in the bubble,

γ = surface tension,

R = radius of the bubble, and

P_L = local pressure of the liquid surrounding the bubble.

If the noncondensable gas is assumed to be an ideal gas at isothermal conditions, we may write

$$P_G = \frac{K}{R^3} , \quad (7)$$

where K is a constant and the amount of gas is assumed to be fixed.

Substituting Equation (7) into Equation (6) and rearranging one obtains

$$P_L - P_v = \frac{K}{R^3} - \frac{2\gamma}{R} . \quad (8)$$

The critical radius, R_{crit} , is found by setting the derivative $[d(P_L - P_v)/dR]$ equal to zero. This yields

$$R_{crit} = \frac{3}{2} \frac{K}{\gamma} . \quad (9)$$

Substituting Equation (9) into Equation (8) one gets the general equation for the critical radius:

$$R_{crit} = \frac{4}{3} \frac{\gamma}{P_v - P_L} . \quad (10)$$

A more complete discussion of bubble growth is presented in reference [22]. With Equation (10), one can calculate the size of a bubble which is in static equilibrium in a liquid at the specified local pressure, P_L . It is assumed that bubbles having radii larger than R_{crit} are candidates for vaporous growth (i.e., cavitation). For our purposes, we will assume that vaporous growth also occurs for nuclei whose sizes

are equal to R_{crit} . By specifying $(P_L - P_v)$ according to the minimum pressure of the model at the experimentally determined conditions of limited travelling cavitation, one obtains an estimate of the size (R_{crit}) of nuclei which will produce travelling cavitation at conditions of limited cavitation on the model. Equation (10) is modified slightly to employ the experimental values of σ_ℓ and $C_{P_{min}}$, thereby specifying the quantity $(P_L - P_v)$. The resulting equation is

$$R_{crit} = \frac{4}{3} \frac{\gamma}{\frac{1}{2} \rho U_\infty^2 (|C_{P_{min}}| - \sigma_\ell)} . \quad (11)$$

It is further assumed that the nuclei which cavitate at conditions of limited travelling cavitation are typically the largest nuclei present in the free stream at those conditions. This is a reasonable assumption, since all nuclei smaller than R_{crit} will not cavitate at the specified value of σ and since nuclei larger than R_{crit} should cavitate at a value of σ correspondingly higher than σ_ℓ . Therefore, we have

$$R_{crit} = R_{max} , \quad (12)$$

and, finally,

$$R_{max} = \frac{4}{3} \frac{\gamma}{\frac{1}{2} \rho U_\infty^2 (|C_{P_{min}}|) - \sigma_\ell} . \quad (13)$$

where R_{max} represents the upper limit for nuclei size in the free stream.

Values of R_{max} have been calculated according to Equation (13) using travelling cavitation data for the three models of the present

investigation. The results are presented in Figure 42. Two plots of R_{max} versus U_∞ are given for each model corresponding to different air contents. These data suggest that, as the free stream velocity was decreased from 70.0 to 20.0 fps during a routine limited cavitation test, the size of the largest (or most cavitation-prone) free stream nuclei in the test section increased by over two orders of magnitude. Visual observations of free stream bubbles in the test section during the course of a cavitation test also indicated that their size and number increased significantly as the free stream velocity was decreased. The data from tests having similar air contents suggest that, at a given velocity, a relatively small range of nuclei sizes was involved with limited travelling cavitation on the three different models.

Van der Meulen [17], Schiebe [20], and Brockett [21] also reported limited cavitation data for travelling cavitation on a 10-mm (0.394-in.) diameter Schiebe nose, a 0.624-in. diameter ITTC nose, and a 2.0-in. diameter DTNSRDC nose, respectively. Values of R_{max} were calculated for these three sets of data and are also plotted in Figure 42. The data all fall within a relatively narrow band which is quite remarkable, since they represent several different models, test facilities, and cavitation calling techniques. The variation in R_{max} with free stream velocity for the different data sets is quite consistent and suggests a universal shift in nuclei size with tunnel velocity for several different facilities. It is interesting to note that none of the tunnel facilities considered here have resorbers. The high-speed water tunnel at CIT, however, is equipped with a resorber and

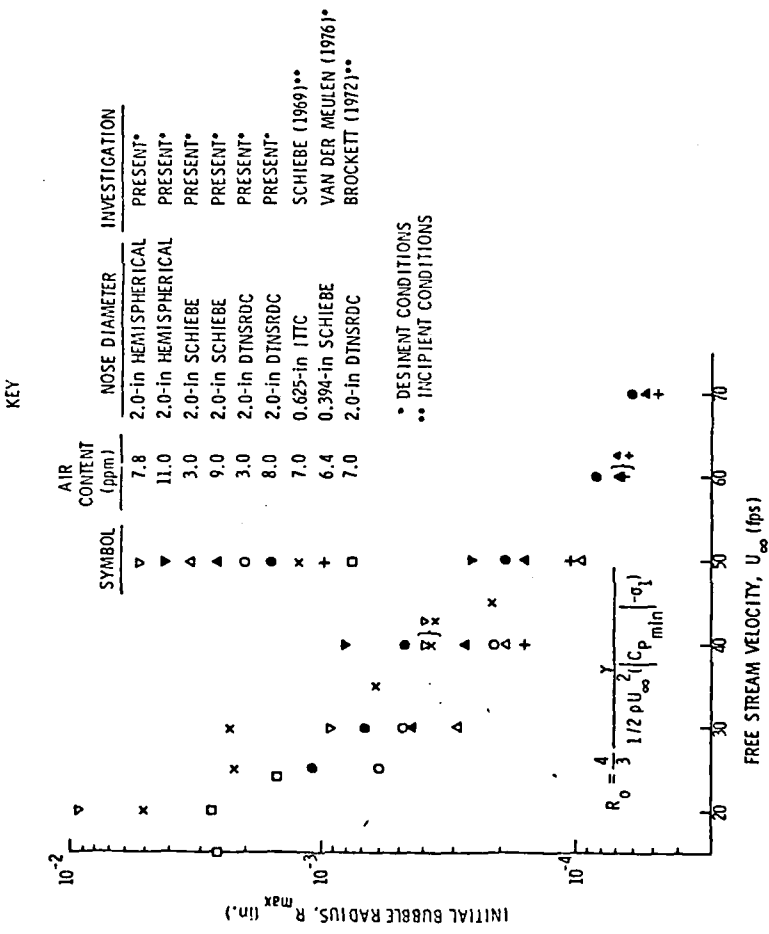


Figure 42. Calculated values of R_{\max} versus U_∞ at conditions of limited transient cavitation from several investigations.

travelling cavitation is rarely seen in this facility, as mentioned previously. It seems likely that values of R_{max} calculated for limited travelling cavitation data from this facility would fall well below the band of data in Figure 42.

The accuracy of the aforementioned calculations is not readily known. It is felt, however, that the results are significant in a qualitative sense. They suggest that limited travelling cavitation characteristics of any model may be predicted from the cavitation data from just one arbitrary model tested in the same facility. Also, the results of calculations using cavitation data from different test facilities may provide a comparison of the nuclei characteristics of the different facilities. The above generalities are presented without substantial experimental evidence and, therefore, are not conclusive. To make these calculations more meaningful provision should be made to account for the effects of model diameter and air content.

5.1.3 Theoretical modelling of travelling cavitation. The idea that the largest or most cavitation-prone nuclei in the free stream vary in size with tunnel velocity, as previously discussed, may be useful in theoretical studies of cavitation. Several attempts have been made in previous investigations to model the physical process of travelling cavitation. Nuclei of specified size were theoretically swept through the pressure distribution of a given model, and the growth of the nuclei was predicted. Generally, the state of limited cavitation was determined by the growth of nuclei from a prescribed initial radius, R_i , to a prescribed final radius, R_f . These initial and final radii remained fixed for all free stream velocities.

See, for example, Holl and Kornhauser [23]. The results always indicated that σ_L increased with free stream velocity. This trend, however, is inconsistent with limited travelling cavitation data from the present investigation.

For theoretical considerations, the process of travelling cavitation formation was simplified to that of a single spherical bubble responding to a spherically symmetric pressure field in a liquid. The liquid was assumed to be irrotational and incompressible. The dynamic behavior of the bubble is described by the Rayleigh-Plesset equation given by

$$R\ddot{R} + \frac{3}{2}\dot{R}^2 = \frac{1}{\rho_L} \left[P_v(T_R) + P_G - P_L - \frac{2\gamma}{R} - \frac{4\mu\dot{R}}{R} \right], \quad (14)$$

where

R = bubble radius;

\dot{R} = $\frac{dR}{dt}$, radial velocity of bubble wall (t = time);

\ddot{R} = $\frac{d^2R}{dt^2}$, radial acceleration of bubble wall;

ρ_L = density of surrounding liquid;

P_v = vapor pressure;

T_R = temperature at the bubble wall;

P_G = pressure of noncondensable gas within the bubble;

P_L = pressure of surrounding liquid;

γ = surface tension; and

μ = coefficient of viscosity of surrounding liquid.

This equation is discussed in greater detail by Hsieh [24]. For a flowing system and for an isothermal process, Equation (14) reduces to

$$\ddot{R} + \frac{3}{2} \dot{R}^2 = \frac{1}{\rho_L} \left\{ p_G - \frac{2\gamma}{R} - \frac{4\mu\dot{R}}{R} + \left[C_p(t) - \sigma \right] \frac{1}{2\rho} U_\infty^2 \right\}, \quad (15)$$

where $C_p(t)$ is a time-dependent pressure coefficient corresponding to the pressure history of a bubble travelling over the model surface.

The numerical solution of Equation (15) is discussed in reference [23].

By giving constant initial values to R_i and R_f , Holl and Kornhauser calculated values of σ_ℓ for travelling cavitation for three different velocities. As mentioned previously, however, the calculated values of σ_ℓ increased with an increase in free stream velocity, which is opposite to the experimental trend observed in the present investigation for transient cavitation. A possible resolution of this problem would be to decrease the value R_i for increasing free stream velocity as suggested by the general trend of R_{max} with velocity, shown in Figure 42. An even more direct method would be to base R_i on measured nuclei data.

5.1.4 Travelling-bubble and travelling-patch cavitation. The development of two different types of travelling cavitation was presumably determined by cavitation number, nuclei size, and distance (of nuclei) from the model surface. Travelling-bubble cavitation was observed to predominate at limited cavitation conditions corresponding to lower velocities, although it was occasionally observed at high velocities. At low free stream velocities, the free air content tended to be higher because the tunnel static pressure was low.

The result was an increase in the number and size of free stream nuclei. Cavitation inception occurred at values of σ_L which approached $|C_{p\min}|$, which indicated that tensions in the water were relatively small. On the other hand, travelling-patch cavitation was predominant at limited cavitation conditions at higher velocities and correspondingly lower cavitation numbers. The number and size of free stream nuclei were significantly lower for this case, and liquid tensions were correspondingly higher. At 30.0 fps, travelling-bubble inception occurred on the Schiebe nose at a calculated tension of -0.75 psia (corresponding to the minimum pressure). In comparison, at 70 fps, travelling-patch inception was observed for a tension of -9.38 psia. This suggests that much greater tensions are required to produce travelling-patch cavitation. The occurrence of travelling bubbles, together with travelling-patch cavitation (Figures 29 and 37) and the observations of partially developed travelling-patch cavitation (Figures 31 and 36), may be explained if one considers nuclei size and/or distance from the model surface. An extremely small nucleus or one that is relatively far from the model may not experience low enough local pressures to develop into a travelling patch. It is also noted that, for these figures, the cavitation number is less than σ_L .

Subsequent high-speed motion pictures of travelling cavitation on a Schiebe nose were taken by David R. Stinebring of the Applied Research Laboratory. The free stream velocity was 30 fps. Large numbers of travelling bubbles, emerging very close to the minimum pressure location, growing as they moved downstream, and then collapsing, were observed. The development of what appeared to be

a travelling patch was also observed. Initially, it resembles a travelling bubble. As it grew and moved downstream, it appeared to drag along the model surface and thereby form a tail. The cavity continued to elongate and the spherical front portion broke off. The remaining cavity then moved downstream and collapsed. A series of sketches are presented in Figure 43 showing the apparent development of a travelling patch.

5.2 Attached Cavitation

5.2.1 Band cavitation. The following characteristics of band cavitation were noted:

1. Band cavitation is controlled by the presence of laminar boundary layer separation.
2. The limited cavitation number for band cavitation increased slightly with free stream velocity. Band cavitation appears to scale reasonably well with the magnitude of pressure coefficients associated with the location of the separated region.
3. The limited cavitation number for band cavitation is essentially insensitive to changes in free stream air content.
4. Band cavitation inception was occasionally preceded by the development of a second type of separation-controlled cavitation, namely, bubble-ring cavitation.

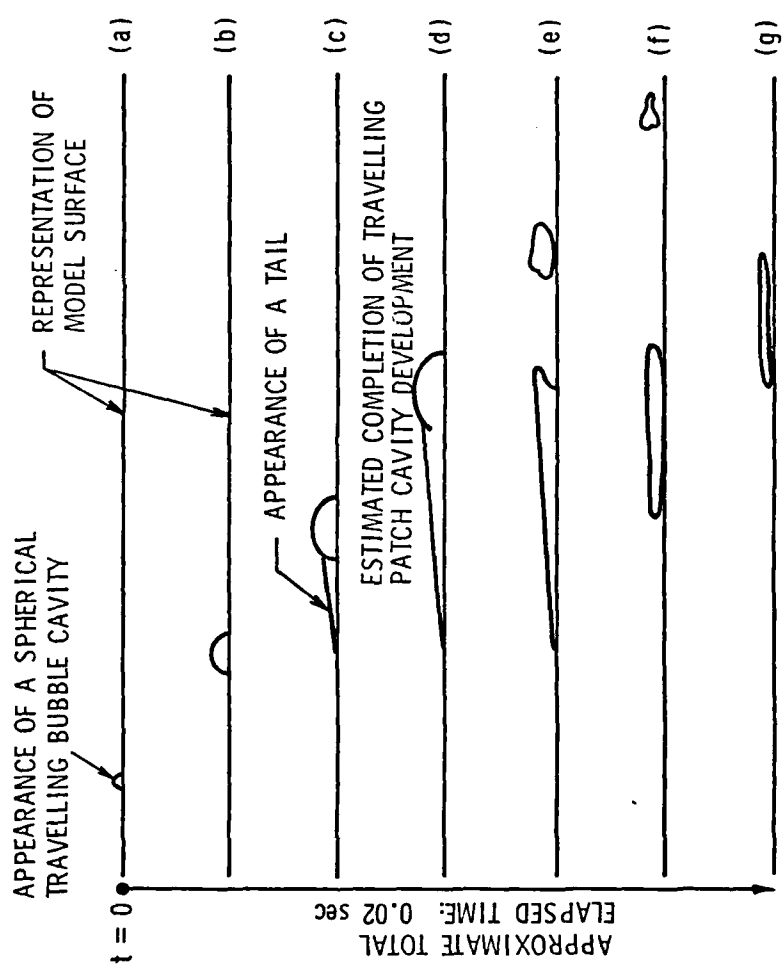


Figure 43. Sketches suggesting the development of travelling-patch cavitation. From observations of high-speed movies of transient cavitation on a Schiebe nose.

5.2.1.1 Characteristics of band cavitation. Band cavitation occurs on axisymmetric bodies which exhibit laminar boundary layer separation. This result was originally reported by Arakeri and Acosta [15], then later by Van der Meulen [17], and by Gates [13]. In the present investigation, band cavitation was observed on the hemispherical nose and the DTNSRDC nose. The fact that both of these models exhibit laminar boundary layer separation was experimentally verified by Gates [13].

Conversely, no band cavitation was observed if laminar boundary layer separation was not present on the model. The following models and test conditions are cited as experimental verification of this observation:

- 1) the hemispherical nose with a boundary layer trip to remove separation,
- 2) the DTNSRDC nose at super-critical Reynolds numbers, and
- 3) the Schiebe nose at all test velocities (natural separation does not occur).

It was also noted that the occurrence of a large number of transient cavities on the hemispherical nose in the presence of band cavitation brought about the elimination of band cavitation as shown in Figures 26(a), (b), and (c). Similarly, on the DTNSRDC nose, it was noted that band cavitation could not be achieved at moderately high air contents. In fact, a more stable band cavity could be obtained on the DTNSRDC body by testing at relatively low air contents. A similar effect of free stream nuclei on band cavitation on both the hemispherical and DTNSRDC noses was reported by Gates [13].

Band cavitation on the hemispherical nose had a very well-defined, steady appearance (see Figure 24). In contrast, on the DTNSRDC nose, band cavitation appeared very irregular and unstable (see Figure 39). This difference in appearance is presumably the result of boundary layer separation being more strongly imposed on the hemispherical nose. Similarly, Gates [13] found laminar separation on the DTNSRDC nose to be quite sensitive to changes in the level of free stream turbulence, whereas laminar separation on the hemispherical nose was not affected. These results were not really surprising since the critical Reynolds numbers, $Re_{D_{crit}}$, for the two bodies differ by an order of magnitude. For cavitation tests, the highest velocity on the hemispherical nose corresponded to $0.23 Re_{D_{crit}}$. In comparison, the highest velocity for band cavitation on the DTNSRDC nose (30.0 fps) corresponded to a Reynolds number equal to the critical Reynolds number calculated for the body. (This observation suggests that the calculated $Re_{D_{crit}}$ for the DTNSRDC nose may be somewhat low.)

5.2.1.2 Scaling of σ_ℓ for band cavitation. Arakeri and

Acosta [15], using Schlieren photography, showed that laminar boundary layer separation is closely associated with the inception of band cavitation. They suggested equating σ_ℓ to the pressure coefficient at the location of boundary layer separation, C_{p_S} , to give

$$\sigma_\ell(\text{band}) = |C_{p_S}| . \quad (16)$$

In Figure 44, pressure coefficients and cavitation numbers for band cavitation on a hemispherical nose are compared. Two sets of

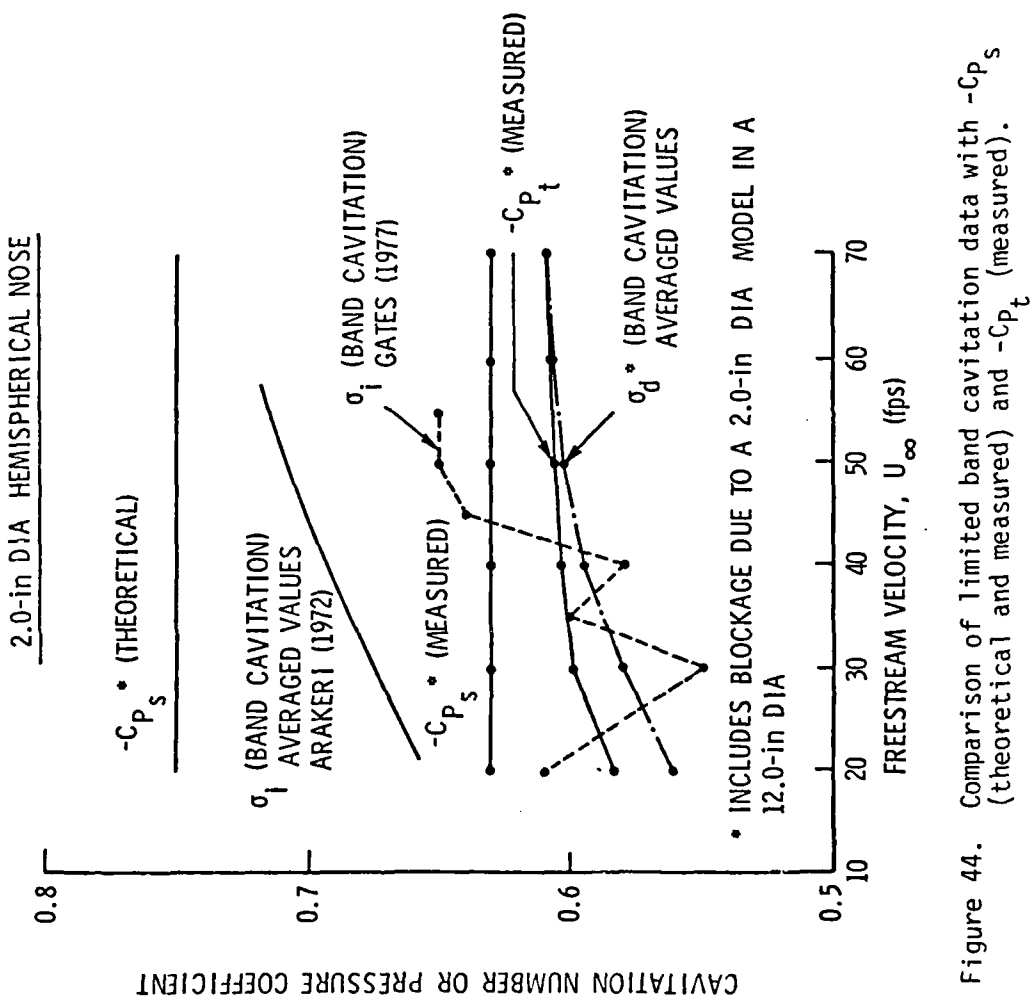


Figure 44. Comparison of limited band cavitation data with $-\bar{C}_{P_s}$ (theoretical and measured) and $-\bar{C}_{P_t}$ (measured).

cavitation data are presented from investigations by Arakeri and Acosta [15] and Gates [13]. Also presented are the averaged values of σ_d for the tests at two air contents from this investigation. In addition, three sets of pressure coefficient data are presented, i.e., the theoretical value of C_{pS} , and the measured values of C_{pS}_{meas} and C_{pt}_{meas} from Figure 49. It is seen that the cavitation data obtained in this investigation are approximated fairly well by the relationship

$$\sigma_\ell(\text{band}) \approx |C_{pt}_{meas}| , \quad (17)$$

whereas

$$\sigma_\ell(\text{band}) < |C_{pS}_{meas}| . \quad (18)$$

In order to compare the CIT data of Arakeri, Acosta, and Gates with the ARL data from this investigation, it is necessary to increase the incipient cavitation numbers by approximately 8.5 percent in order to correct for blockage. The CIT data are thus generally higher than the ARL data, and the reasons for these discrepancies have not been explained. Generally, the measured coefficients, C_{pS}_{meas} and C_{pt}_{meas} , would not be available, whereas one can in principle obtain C_{pS} by theoretical means. Thus, comparing all data for the blocked state indicates that, in most cases, the cavitation number satisfies the relation

$$\sigma_\ell(\text{band}) < |C_{pS}(\text{theoretical})| . \quad (19)$$

Although fewer data were obtained for limited band cavitation on the DTNSRDC nose, the above relation was also satisfied for this nose.

5.2.1.3 Effects of air content on band cavitation. The relative insensitivity of σ_ℓ to variation in air content for band cavitation agrees with the early findings of Parkin and Kermeen [10], and the recent results of Gates [13]. Two small effects were noted, however, which suggest that air content does influence band cavitation. For high air contents which result in a large free stream nuclei population, a slight reduction in σ_ℓ was observed for band cavitation. This effect was generally observed at low free stream velocities. Also, band cavitation has been observed to disappear in the presence of many travelling bubbles as discussed earlier [see Figures 26(a), (b), and (c)]. The second effect was a noted increase in hysteresis for band cavitation at low air contents. This point will be discussed in greater detail subsequently.

5.2.1.4 Bubble-ring cavitation. Bubble-ring cavitation, which was observed only on the hemispherical nose in the present investigation, is generally associated with band cavitation. Both bubble-ring and band cavitation are controlled by laminar boundary layer separation. Bubble-ring cavitation occurs in the reattachment region where large turbulent fluctuations have been reported in references [25], [26], and [27]. In the present investigation, σ_ℓ for bubble-ring cavitation was always greater than σ_ℓ for band cavitation by approximately a constant value, which was usually no greater than 0.03 (refer to Figure 21). Therefore, we can say

$$\sigma_\ell(\text{bubble-ring}) = \sigma_\ell(\text{band}) + \Delta\sigma , \quad (20)$$

where $\Delta\sigma \approx 0.03$. If we use the correlation $\sigma_\ell(\text{band}) = |C_{pS}|$ as discussed previously, and relate $\Delta\sigma$ to the fluctuating pressures of reattachment ($\Delta\sigma = |C_{p'_r}|$, where $C_{p'_r} = P'_r/1/2\rho U_\infty^2$, and P'_r is the instantaneous pressure fluctuation at reattachment), we may write

$$\sigma_\ell(\text{bubble-ring}) = \sigma_\ell(\text{band}) + \left| \frac{P'_r}{\frac{1}{2}\rho U_\infty^2} \right| \quad (21)$$

or

$$\sigma_\ell(\text{bubble-ring}) = \left| C_{pS} \right| + \left| \frac{P'_r}{\frac{1}{2}\rho U_\infty^2} \right| . \quad (22)$$

Measurements of the pressure fluctuations at reattachment were performed on a hemispherical nose in the present investigation and will be discussed in Chapter 7.

Several tests were performed to determine the effect of air content on bubble-ring cavitation. The results showed some rather interesting effects of both air content and water temperature on bubble-ring cavitation formation. Generally, bubble-ring cavitation was observed for all air contents from 4.0 to the upper limit of 12.0 ppm. No bubble-ring cavitation was observed for values less than 4.0 ppm. Its appearance with regard to number and density of individual cavities and overall steadiness of the ring formation many times differed from one test to the next and often showed no correlation with a change in air content. In separate cavitation tests at nearly equal air contents, a data spread of as much as

6.0 percent was noted in the limited cavitation results. It was later discovered that this scatter in the data could be correlated surprisingly well with the operating temperature of the water. The results of three separate tests for bubble-ring cavitation are presented in Figure 45. The air contents for the three tests were all about 8.0 ppm. It is apparent that σ_ℓ decreased slightly with increasing water temperature. Also, as temperature increased, bubble-ring cavitation was eliminated at the lower velocities. It is strongly suspected that a selective size range of nuclei is required for bubble-ring cavitation to occur. On the other hand, raising the water temperature decreases the solubility of air in water and results in an increase in the number and size of nuclei. This trend would suggest that σ_ℓ should increase with temperature for bubble-ring cavitation; this is opposite to the observed trend. Thus, other factors are controlling the phenomena. Perhaps the increased nuclei population which resulted from higher water temperatures acted as a free stream disturbance which affected the laminar boundary layer separation processes. Consequently, the pressure fluctuations at reattachment were also affected in such a way that bubble-ring cavitation was suppressed. Recall that large numbers of free stream nuclei and travelling-bubble cavitation have been observed to affect boundary layer separation and result in the elimination of band cavitation.

5.2.1.5 Bubble-ring and band cavitation. Bubble-ring cavitation on the hemispherical nose serves as a nuclei source for band cavitation. In a typical cavitation run, bubble-ring cavitation developed in the reattachment region, then gradually extended forward

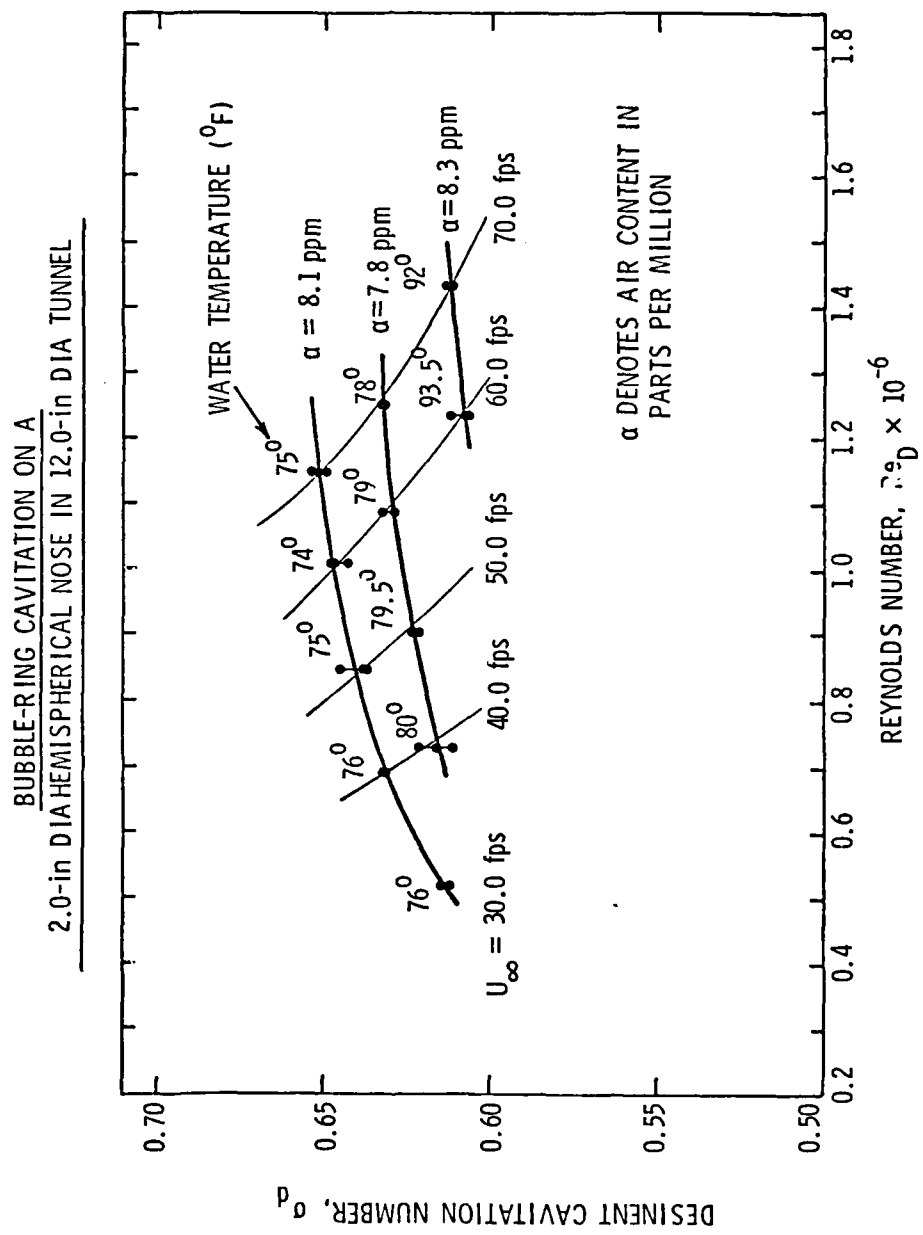


Figure 45. Effect of temperature of σ_d for bubble-ring cavitation on a 2.0-in. diameter hemispherical nose.

into the separation region to form band cavitation. This transformation from bubble-ring to band cavitation is shown in Figure 25. Hysteresis effects were not apparent for band cavitation if bubble-ring cavitation was observed. When no bubble-ring cavitation occurred, however, band cavitation often appeared suddenly in a developed state and was interpreted as hysteresis. In this case, the readily available nuclei (in the form of bubble-ring cavitation) were not present. As a result, inception of band cavitation presumably had to depend on the event of a nucleus from the free stream travelling close enough to the body to initiate cavitation. Hysteresis effects in band cavitation on the hemispherical nose became apparent for low air contents and/or high water temperatures. In all cases, bubble-ring cavitation was suppressed. A similar result was reported by Acosta and Hamaguchi [28] for cavitation observations on a 1.755-in. diameter ITTC nose. Bubble-ring cavitation was not reported for this body and band cavitation was indeed observed to appear "abruptly in the form of a small band all around the nose of the body."

5.2.1.6 Occurrence of bubble-ring cavitation. Observations of separation-controlled cavitation have been reported on various axisymmetric models in previous investigations. Parkin and Holl [9] observed band cavitation on both the hemispherical nose and 1.5-caliber ogive nose in tests which involved several different model diameters. Band cavitation was also observed on a 2.0-in., 1.0-caliber ogive nose in a preliminary test during the present investigation, a 1.755-in. diameter ITTC nose [26], a 2.0-in. diameter, 1/8-caliber ogive nose [29], and a 2.0-in. pointed headform used by Brockett [21]. Of these

models, bubble-ring cavitation was observed on only the hemispherical nose and the 1/8-caliber ogive nose. It seems rather curious that, for several models which exhibited laminar boundary layer separation, bubble-ring cavitation was only observed on certain models. This suggests that the influence of laminar boundary layer separation on limited cavitation differs slightly from one model to the next.

Consider two axisymmetric models (A and B) which both exhibit laminar boundary layer separation. Model A has a large separated region of nearly constant pressure, accompanied by strong turbulent pressure fluctuations in the reattachment region. Model B has a thin separation region with a slight adverse pressure gradient and correspondingly small pressure fluctuations at reattachment. These two examples are illustrated in Figure 46. The large pressure fluctuations at reattachment for Model A result in a fluctuation pressure coefficient, C_{P_r}' , whose magnitude is greater than the magnitude of the pressure coefficient at separation, $|C_{P_S}|$. Therefore, bubble-ring cavitation occurs on Model A prior to the gradual development of band cavitation as the cavitation number is lowered. At desinence, band cavitation gradually transforms back into bubble-ring cavitation. On Model B, it is shown that C_{P_r}' is less than $|C_{P_S}|$. Bubble-ring cavitation is not observed on this model. As the tunnel pressure is lowered, the pressure in the separation region falls to vapor pressure before the pressure in the reattachment region. If bubble-ring cavitation occurs at reattachment, it immediately transforms into band cavitation because the separated region is at a lower pressure. Otherwise, band cavitation inception occurs when a free stream nucleus enters the separated region.

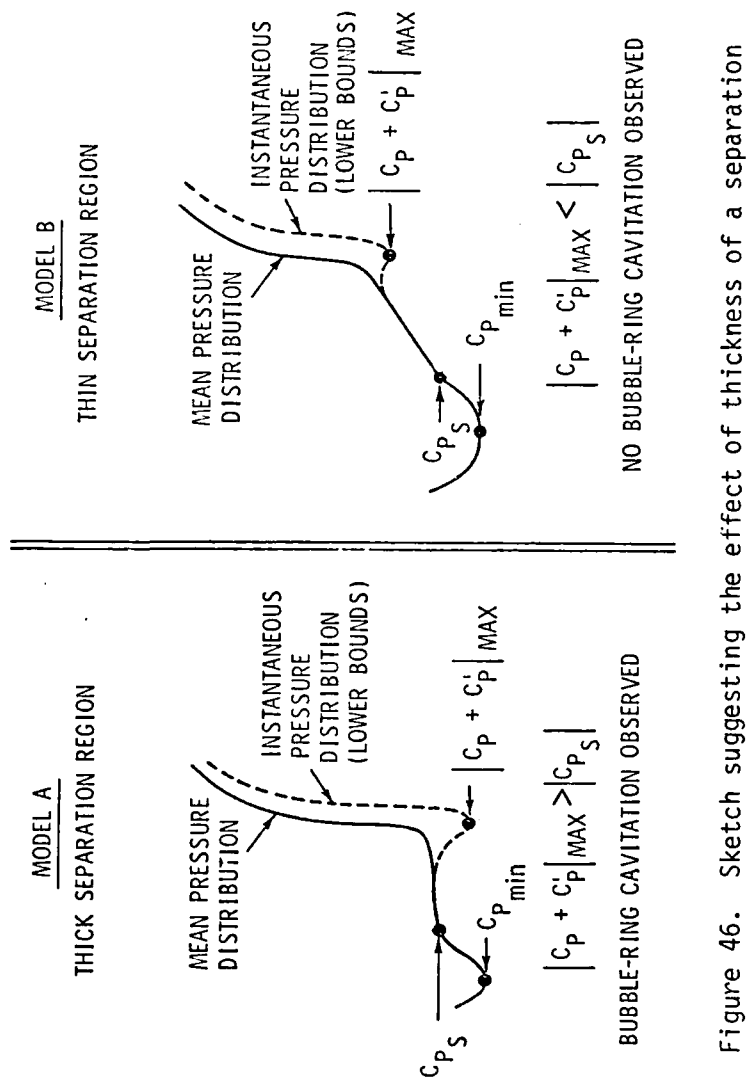


Figure 46. Sketch suggesting the effect of thickness of a separation region on the surface pressure distribution.

In either case, band cavitation is observed to form suddenly as a completely developed cavity. At desinence, band cavitation gradually disappears with no trace of bubble-ring cavitation. Hysteresis is, therefore, observed on Model B. Noses which exhibit the characteristics of Model A are the hemispherical nose and the 1/8-caliber ogive nose. Those characteristics of Model B include the 1.5-caliber ogive nose, 1.0-caliber ogive nose, ITTC nose, and the DTNSRDC nose.

5.2.2 Fixed-patch cavitation. The following are several characteristics of fixed-patch cavitation which were observed in the present investigation:

1. Fixed-patch cavitation was predominant at high free stream velocities.
2. Limited cavitation data for fixed-patch cavitation showed a definite increasing trend of σ_i with an increase in free stream velocity.
3. High air contents appeared to suppress the formation of fixed-patch cavitation and resulted in lower values of σ_ℓ .
4. Each individual cavity of fixed-patch cavitation appeared to be attached to the model surface at one or two points on the upstream end of the cavity. These points of attachment may possibly be located on very small depression-type irregularities on the model surface.

5.2.2.1 Characteristics of fixed-patch cavitation. Fixed-patch cavitation was observed on the Schiebe nose and the DTNSRDC nose in the present investigation. It was also observed on a 1.755-in. diameter ITTC nose in the investigation by Acosta and Hamaguchi [28].

They show an excellent photograph of fixed-patch cavitation occurring simultaneously with band cavitation on their model. Their indication that fixed-patch cavitation occurred at higher velocities is consistent with the results of the present investigation. Parkin and Holl [9] also reported the observation of "small diamond-shaped cavitation zones apparently due to very small rough spots." These observations were made during cavitation tests which were conducted with 4.0-in. and 8.0-in. diameter hemispherical noses. Their description suggests that this also was fixed-patch cavitation. In the present investigation, fixed-patch cavitation occasionally occurred on the 2.0-in. diameter hemispherical nose as a result of dirt on the model. Wiping off the model surface subsequently eliminated the formation of fixed-patch cavitation on the hemispherical nose, but the same procedure showed little or no effect on the DTNSRDC and Schiebe noses.

Generally, increasing the air content of the water resulted in a more unsteady form of fixed-patch cavitation. Occasionally, when many free stream nuclei passed by the model, fixed-patch cavities became very unstable and erratic, and they appeared and disappeared all around the circumference of the nose. The nuclei in the free stream seemed to act as disturbances which affected the seemingly delicate attachment that the cavities had to the model surface. In contrast, when the air content was low and few free stream nuclei were observed, the cavities appeared very steady and rigidly affixed to the model surface.

An effect which may be related to the above observation is reported by Arakeri and Acosta [16]. In their investigation of cavitation on an ITTC standard headform, they observed the elimination of

fixed-patch cavitation by the application of a boundary layer trip. This suggests that fixed-patch cavitation cannot occur in the presence of a turbulent boundary layer. Thickening the boundary layer by tripping tends to decrease σ for a given roughness, whereas changing the velocity profile from laminar to turbulent would tend to increase σ . Since these are counteracting effects, it is difficult to explain this result from Arakeri and Acosta.

In the present investigation fixed-patch cavities always appeared abruptly at inception and disappeared abruptly at desinence. This was apparent particularly at the low free stream velocities. Large cavities, almost a full body diameter in length, would suddenly appear at inception and grow as the pressure was lowered. On increasing the pressure, the cavities would generally shrink to their initial size at inception and then disappear. At higher velocities, much smaller cavities were observed which had lengths of about one-quarter of the body diameter. The growth characteristics of these smaller cavities were essentially the same as for the larger ones.

The attachment of fixed-patch cavities occurred at very definite locations on the model surface. Although, in general, no cavities showed any preferred location around the circumference of the body, they all seem to attach at an axial location just downstream of, but very near to the minimum pressure location. Particularly at high free stream velocities, several nearly identical fixed-patch cavities often formed and were evenly spaced around the circumference of the model. Figures 33 and 40 show this on the Schiebe nose and the DTNSRDC nose, respectively. That the cavities on each body are similar in size

suggests that the surface irregularities are similar around each nose. The model surfaces were subsequently inspected. Both models showed a distributed roughness of approximately 4.0 micro-in. (rms). Isolated machining scratches which were estimated to be about 0.001-in. wide were also found on both models in the region of the minimum pressure. All roughnesses were depressions into the surface. For comparison, the laminar boundary layer thickness at the minimum pressure location for both models is about 0.002-in. at the maximum free stream velocity of 70.0 fps.

5.2.2.2 Scaling problem of fixed-patch cavitation. Fixed-patch cavitation was observed predominantly at high velocities in the present investigation. Also, the value of σ_{ℓ} increased very definitely with an increase in free stream velocity. Such characteristics are expected for cavitation controlled by surface roughness. However, several inconsistencies appeared when attempting to understand this form of cavitation by applying existing theoretical modelling techniques. For example, Bohn [30] used the superposition method of Holl [31] along with empirical cavitation data for a specified roughness on a flat plate to predict σ_{ℓ} for the same roughness on a specified body. The equation for the cavitation number of a body with roughness is given by

$$\sigma_{\ell} = - C_{P_B} + \sigma_R \left(1 - C_{P_B} \right) \quad (23)$$

where

σ_{ℓ} = limited cavitation number of a body with roughness,

C_{P_B} = pressure coefficient on smooth body at roughness location,
and

σ_R = limited cavitation number of the roughness on a flat plate.

Using this method, one always obtains a σ_ℓ for a body with roughness which is greater in magnitude than the pressure coefficient of the smooth body at the roughness location, provided that σ_R is positive.

In the present investigation, all limited cavitation data for fixed-patch cavitation were less than $|C_p|$ at the corresponding point of cavity attachment. From photographs of the DTNSRDC nose, the value of x/D for cavity attachment was estimated to be 0.09. The value of $|C_p|$ corresponding to this location was 0.77. Measured values of σ_ℓ for fixed-patch cavitation on this body ranged from 0.57 to 0.69.

Similarly, for the Schiebe nose, cavity attachment occurred at an x/D of about 0.18; the corresponding value of $|C_p|$ was 0.65, and σ_ℓ ranged from 0.35 to 0.45. It was apparent, therefore, that Bohn's method could not be applied to the fixed-patch cavitation that was observed in this investigation.

Equation (23) has been revised by Arndt, Holl, Bohn, and Bechtel [32] to include bubble dynamic effects. The revised equation is

$$\sigma_\ell = - C_{P_B} - \Omega + \sigma_R \left(1 - C_{P_B} \right) . \quad (24)$$

The function Ω accounts for possible bubble dynamic effects and is defined as

$$\Omega = \frac{P_v - P_{\min-r}}{\frac{1}{2} \rho U_\infty^2} , \quad (25)$$

where P_{min-r} is the minimum pressure produced by the roughness. In some cases, where Ω is sufficiently large, Equation (24) suggests that σ_ℓ can be less than $|C_{p_B}|$. Application of Equation (24) to some of the fixed-patch cavitation encountered in this investigation indicated this type of behavior. An inconsistency exists, however. Raising the air content tends to increase the size of free stream nuclei and the results should be higher values of σ_ℓ for fixed-patch cavitation. As mentioned previously, the opposite trend was observed.

5.2.2.3 Hypothetical development of fixed-patch cavitation.

It is believed that the location of fixed-patch cavity attachment is significant. Attachment always seemed to occur in a laminar boundary layer in a region which had a severely adverse pressure gradient. It may be that this type of cavitation occurred as a consequence of the adverse pressure gradient and the tendency for the boundary layer to separate. Consider the following hypothetical development:

A nucleus in the boundary layer cavitates and causes a local flow separation to occur which is augmented by the effect of the adverse pressure gradient. The vapor cavity immediately fills the three-dimensional separation region. The separation region and the cavity both spread upstream into lower pressures. The upstream end of the cavity then becomes stabilized at the site of a very tiny depression-type irregularity on the model surface, close to the minimum pressure location. The above process occurs over a very short time period, making the cavity development appear to be instantaneous.

A sketch is presented in Figure 47 illustrating the events just described in this hypothetical development of fixed-patch cavitation.

The following characteristics help to support this hypothesis:

- 1) It is a form of attached cavitation. This fact in itself suggests that the cavity resides in a separation region.
- 2) Boundary layer tripping eliminates fixed-patch cavitation. The resulting turbulent boundary layer is more resistant to separation.
- 3) Irregularities in the model surface were in the form of very small depression-type roughnesses. It seems unlikely that similar forms of attached cavities would occur on the same type of roughness on a flat plate with no pressure gradient because the suspected roughness size is so much smaller than the resulting cavity.

The foregoing discussion of fixed-patch cavitation suggests that surface roughness can play a major role in controlling this type of cavitation on axisymmetric bodies. Investigations at ARL also indicate that surface roughness can control the limited cavitation characteristics of sheet cavitation on hydrofoils.

Unfortunately, the mechanisms involved in the formation of fixed-patch cavitation are not understood. Very few, if any, investigations have been performed on depression-type surface irregularities, particularly in the presence of a strong adverse pressure gradient. The observations of fixed-patch cavitation in several cavitation investigations (where surface roughness was not considered significant) suggests that more work should be done in this area.

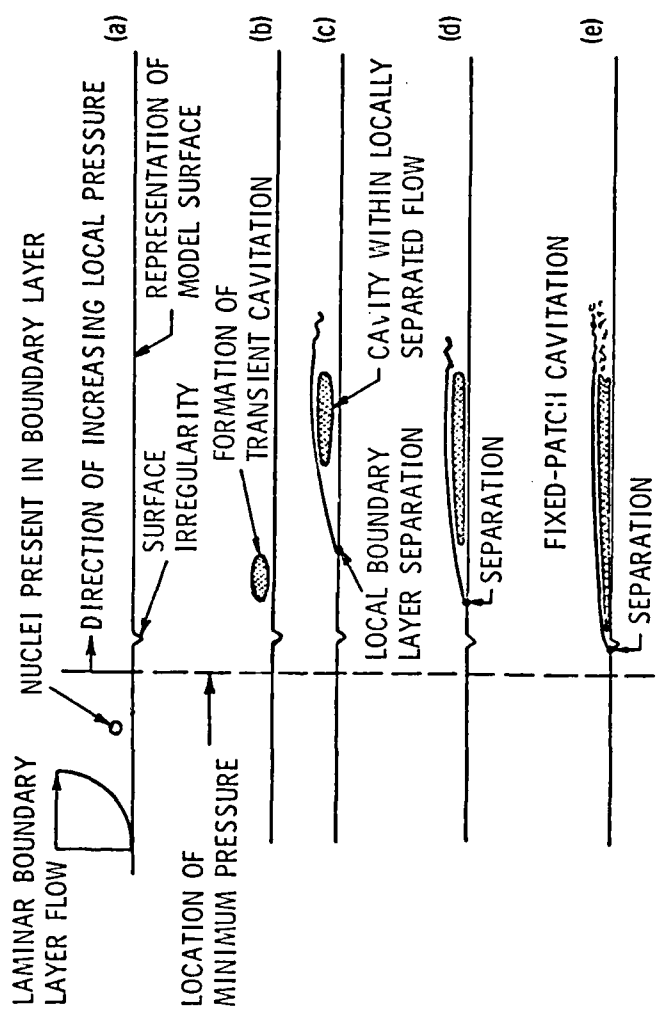


Figure 47. Sketches illustrating the hypothetical development of fixed-patch cavitation.

5.2.3 Developed cavitation. Developed cavitation, as described in the results (Section 4.1.2) was observed on the Schiebe half-body and the DTNSRDC headform for all test velocities. The formation of this type of cavitation drastically changes the flow about a body and, therefore, was not considered of interest in the present investigation. It is interesting to note that developed cavitation as defined in this investigation does not appear on the hemispherical nose. Instead, band cavitation forms and continues to grow, mostly in the downstream direction, for lower and lower values of the cavitation number. The manner in which this occurs is discussed in more detail by Arakeri [14].

It is believed that developed cavitation remains attached to the body by the presence of a cavitation-induced flow separation. The process is similar to that discussed for fixed-patch cavitation. The initial formation of cavitation (transient or fixed-patch) in the region of an adverse pressure gradient disturbs the flow and causes it to separate at a position just downstream from the minimum pressure point. A large single cavity fills the separated region and, thereby, stabilizes the separated region and the cavity on the body. This order of events for developed cavitation formation was hypothesized from playback and analysis of the cavitation tapes.

CHAPTER 6

PRESENTATION AND DISCUSSION OF MEAN PRESSURE MEASUREMENTS
ON A 2.0-IN. DIAMETER HEMISPHERICAL NOSE6.1 Introduction

The recently discovered association between band cavitation and laminar boundary layer separation has resulted in a renewed interest in the real pressure distribution over a hemispherical nose. For years, it was believed that laminar boundary layer separation did not occur on a hemispherical nose for typical values of Reynolds number. In 1948, Rouse and McNown [11] measured the mean pressure distribution over a 2.0-in. diameter hemispherical nose for several Reynolds numbers. The influence of a separated boundary layer was reported up to a Reynolds number of 2.0×10^5 . Poor spatial resolution due to relatively large spacing between pressure taps yielded misleading results. Twenty-five years later, Arakeri and Acosta [15] showed by means of Schlieren photography that laminar boundary layer separation exists on a 2.0-in. diameter hemispherical nose for Reynolds numbers in excess of 1×10^6 . They also showed that viscous effects and, more specifically, the presence of laminar boundary layer separation has a significant influence on the inception of cavitation on axisymmetric models.

Two regions are associated with laminar boundary layer separation; namely, (1) the separated region, and (2) the transition/reattachment region.

The separated region is characterized by the small pocket of nearly stagnant fluid located beneath the separated streamline and just above the model surface. The pressure is nearly constant throughout the

separated region. In the present investigation, only a short separation bubble regime was considered since the conditions necessary for a long bubble, as proposed by Gaster [25], were not present. The theoretical location of laminar boundary layer separation is predicted when the wall shear stress vanishes in the presence of an adverse pressure gradient. For a given body, the location of laminar boundary layer separation does not vary in the streamwise direction with Reynolds number. Arakeri and Acosta [15] verified this experimentally on a 1.813-in. diameter hemispherical nose. Their Schlieren photographs of the thermal boundary layer showed that the streamwise distance to separation was constant for velocities from approximately 10.0 to 60.0 fps. It should be mentioned, however, that in this same investigation, Arakeri and Acosta reported a slight downstream shift in the position of laminar separation on a 1.755-in. diameter ITTC nose over the same velocity range. No explanation was offered since the shift was considered insignificant. Van der Meulen [17] also concluded that the location of laminar boundary layer separation remains constant with velocity from his investigation of the flow over a 10-mm (0.394-in.) diameter hemispherical nose. Flow visualization was achieved by the injection of low concentration salt water from the stagnation tap of his model into the boundary layer flow. Holographs were taken which very clearly showed the structure of the separation region.

Dimensions of the separation region showed significant variation from one model shape to the next. Arakeri [14] presented height and length information for the separated region on a 1.813-in. diameter hemispherical nose and a 2.0-in. Swedish headform (ITTC nose) for a

range of velocities. Gates [13] presented similar information for a 2.0-in. diameter hemispherical nose and 2.0-in. diameter DTNSRDC nose. The results clearly indicate that the dimensions of a separation region decrease with increasing Re_D . This dependence on Reynolds number differs, however, for the different nose shapes.

The transition/reattachment region occurs at the downstream end of the separation region. The length of the separation region is controlled solely by the location of transition and reattachment, since the upstream end, defined by the point of separation, does not move with variation in free stream velocity. Transition occurs when the free shear layer above the separation region becomes unstable. The instability of the free shear layer increases, producing turbulent mixing which results in the reattachment of a turbulent boundary layer to the model surface. The reattachment region is characterized by large turbulent pressure fluctuations. Arakeri [26] measured peak pressure fluctuations in this region of the order of 26.0 percent of the dynamic pressure on a 2.0-in. diameter hemispherical nose in water. With such large pressure fluctuations in the reattachment region, it seems reasonable that cavitation inception has been frequently observed on the hemispherical nose at the site of laminar boundary layer reattachment rather than at the theoretical location of the minimum pressure [13, 15, and 17].

It is apparent that viscous effects must be taken into consideration in order to understand more fully the mechanisms of cavitation inception. The presence of laminar boundary layer separation may significantly alter the mean pressure distribution from that predicted

by potential theory. Also, pressure fluctuations arising from boundary layer turbulence may play a significant role in the process of cavitation inception. Reliable measurements of both the mean and fluctuating pressure components in the region of separation and reattachment would be very helpful in the investigation of limited cavitation.

Mean pressure measurements were made in the region of boundary layer separation and reattachment on a 2.0-in. diameter hemispherical nose in water and are presented and discussed in this section.

Fluctuating pressure measurements were made in water in the region of boundary layer reattachment and will be discussed in Chapter 7. The results from these mean and fluctuating pressure measurements are discussed in connection with band and bubble-ring cavitation, respectively, as observed on the hemispherical nose.

6.2 Experimental Setup Procedure

Mean pressure measurements over a 2.0-in. diameter hemispherical nose were performed in the 12.0-in. diameter water tunnel located in the Garfield Thomas Water Tunnel Building of the Applied Research Laboratory at The Pennsylvania State University. Measurements were made by using static pressure taps which were distributed over the model surface. A total of 18 taps were employed, including a total pressure or stagnation tap. All measurements were nondimensionalized by the reading from this stagnation tap. All taps were 0.0135-in. in diameter. Locations of the taps on the model are presented in Table 2. The axial spacing of the taps provided good spatial resolution, which is important due to the small size of the separation region. The circumferential positioning of the taps was to avoid possible measurement errors due

Table 2
Pressure Tap Locations on 2.0-in.
Diameter Hemispherical Nose

<u>Tap Number</u>	<u>x/D</u>	θ (deg)
1	0.000	—
2	0.280	51
3	0.335	64
4	0.390	38
5	0.430	77
6	0.465	25
7	0.480	90
8	0.500	129
9	0.515	116
10	0.530	142
11	0.545	103
12	0.560	155
13	0.575	77
14	0.625	129
15	0.675	116
16	0.725	129
17	0.775	116
18	0.825	129

to wake interference from upstream taps. This consideration was made only in the laminar flow region and was not considered a problem in the regions of separated and turbulent flow.

A 2.0-in. diameter stainless steel model was machined for this investigation. The model was made in two parts with pressure taps located in a removable hatch. A photograph of the model is presented in Figure 48. The hatch configuration made it possible to connect pressure lines to the 18 short steel tubes located within the model. The pressure lines ran through a hollow afterbody, down through the mounting strut, and out of the tunnel into a 48-position scani-valve. Alignment of the model in the test section was achieved by visually checking the flow direction of dye-colored water forced out through the stagnation tap on the front of the model. True alignment was attained when the dye was observed to flow uniformly over the model. All pressures were measured with a Bell and Howell differential-type pressure transducer. Static calibration prior to testing showed the transducer to have a linear response for the entire pressure range. Measurement errors for this type of pressure transducer are within ± 0.06 percent of full-scale range as claimed by the manufacturer. The scani-valve was operated by an automatic, programmable stepping control unit. The unit was programmed to step through the 18 pressure channels plus four reference channels for zeroing purposes. An additional channel provided the pressure drop through the test section nozzle for monitoring the tunnel velocity. For each channel, the unit time-averaged the signal and punched the data on paper tape. At each test velocity, the unit stepped through each of the 23 channels

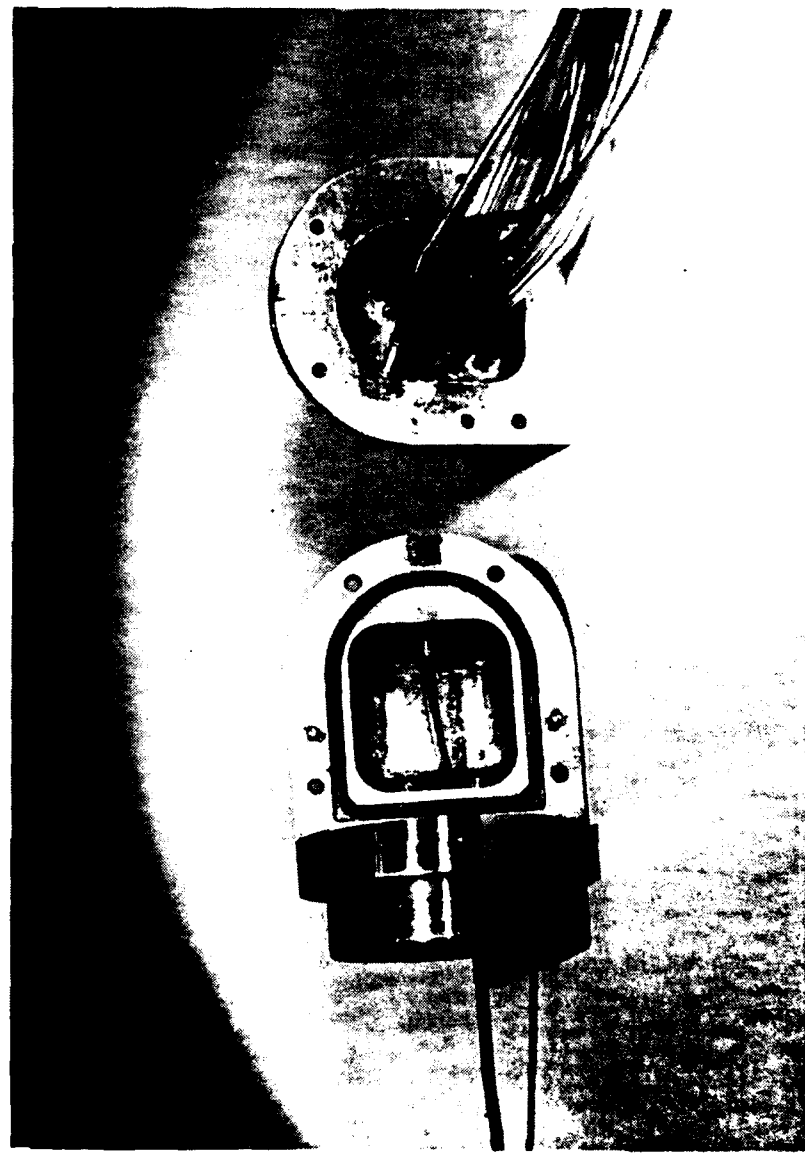


Figure 48. Photograph of instrumented 2.0-in. diameter hemispherical nose used for mean pressure measurements.

five times. The test velocity was varied from 30.0 to 70.0 fps. The tunnel pressure was held constant at about 30.0 psia. The data were subsequently reduced and averaged on a computer. A similar series of tests were also performed to show the effect of a boundary layer trip which was placed on the model to eliminate laminar boundary layer separation.

6.3 Results

The measured mean pressure distributions over a 2.0-in. diameter hemispherical nose are presented in Figure 49 for several values of free stream velocity. Data are shown as plots of pressure coefficient, C_p , versus axial distance, x/D , along the model. The theoretical curve for a hemispherical nose with appropriate blockage is also shown for comparison. As mentioned earlier, each data point represents the averaged values of five separate measurements. Spread in the measured data is approximately ± 0.006 .

The results of tripping the boundary layer are presented in Figures 50 and 51 for free stream velocities of 30.0 and 40.0 fps, respectively. Both figures compare tripped and nontripped cases with the curve from potential theory. These data are tabulated in Appendix D. Values of standard deviation, S_d , and relative standard deviation, \bar{S}_d , are also given.

6.4 Discussion of Results

The occurrence of laminar boundary layer separation on a 2.0-in. diameter hemispherical nose is indicated by Figure 49 for Reynolds number up to 1.17×10^6 (70.0 fps). This result is in agreement with

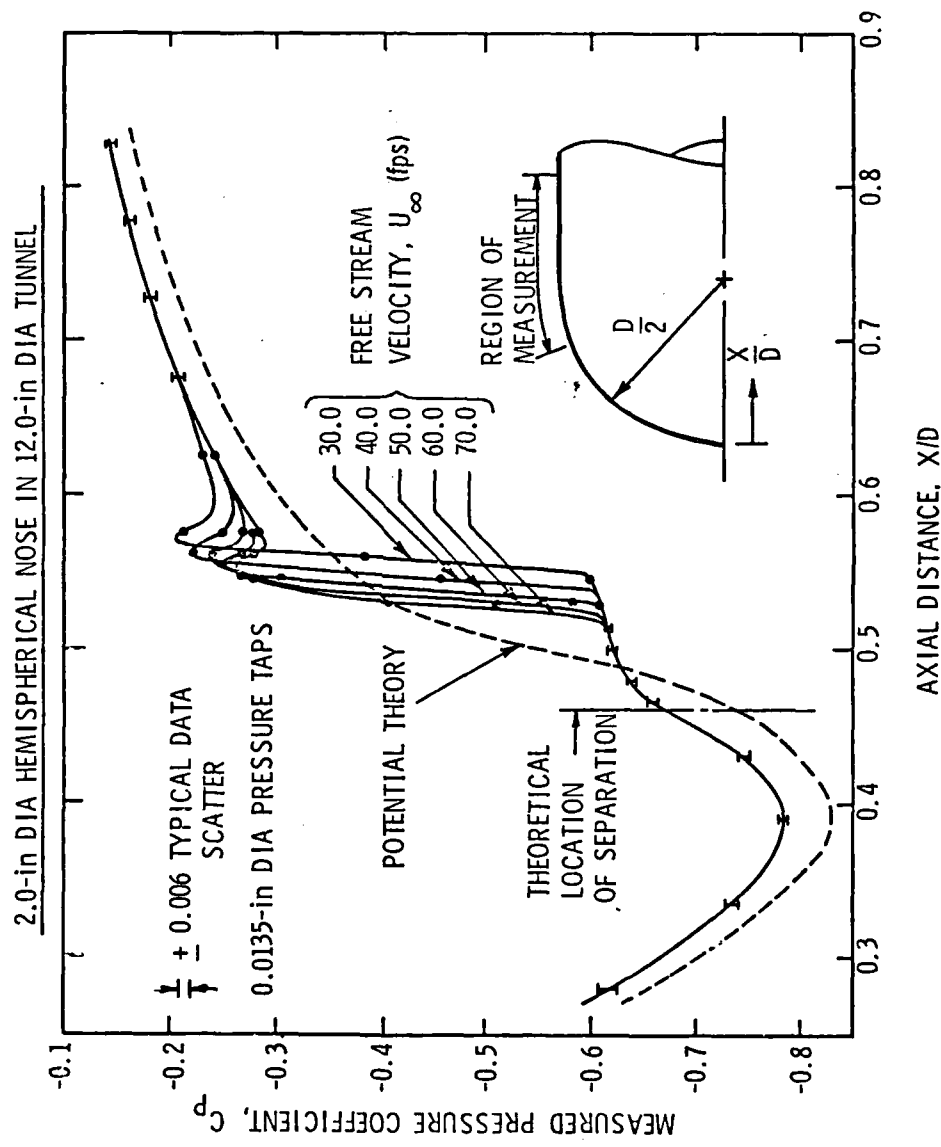


Figure 49. Measured pressure distribution over a 2.0-in. diameter hemispherical nose for several free stream velocities.

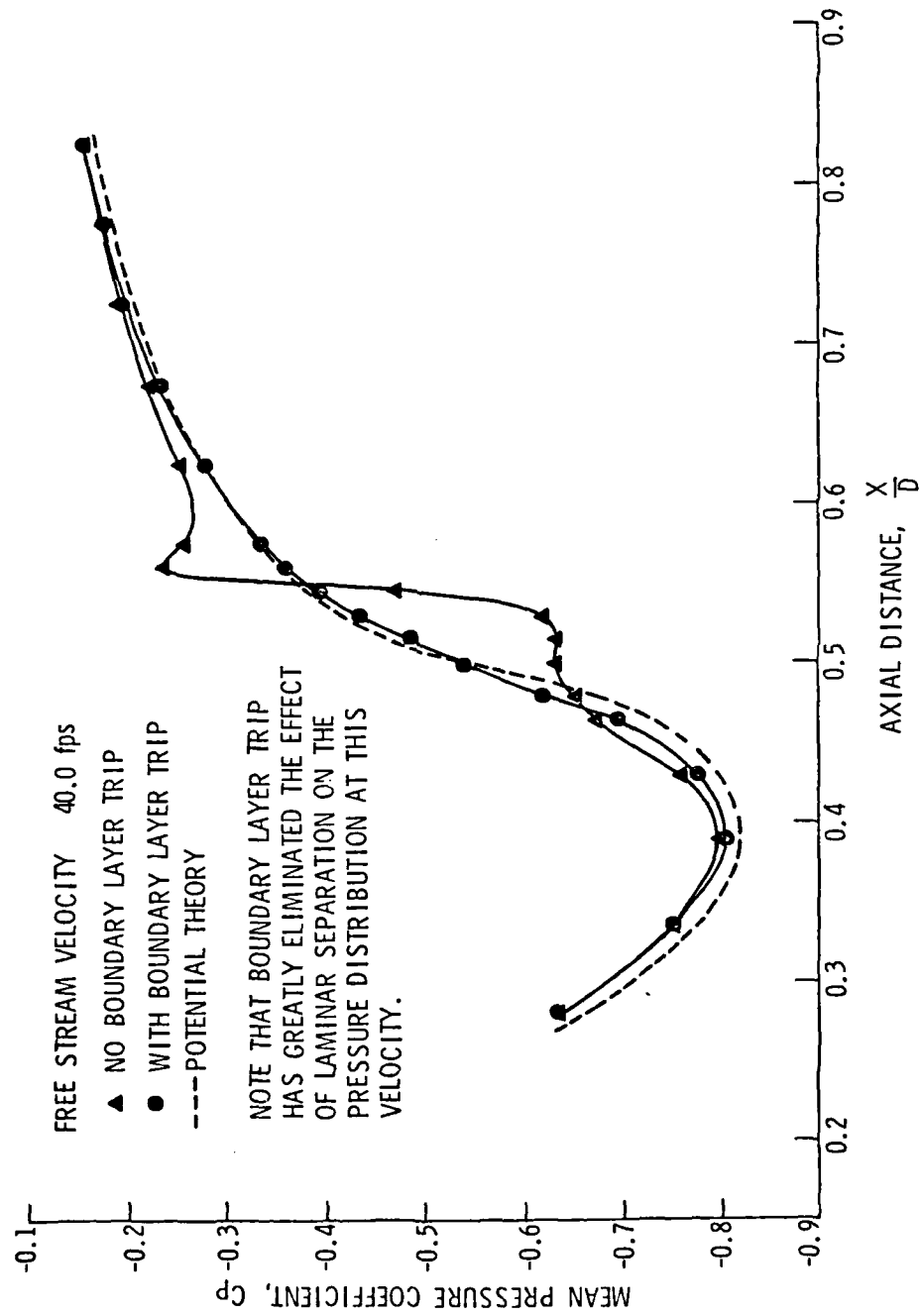


Figure 50. Comparison of measured pressure distributions for a 2.0-in. diameter hemispherical nose with and without a boundary layer trip ($U_{\infty} = 40.0$ fps).

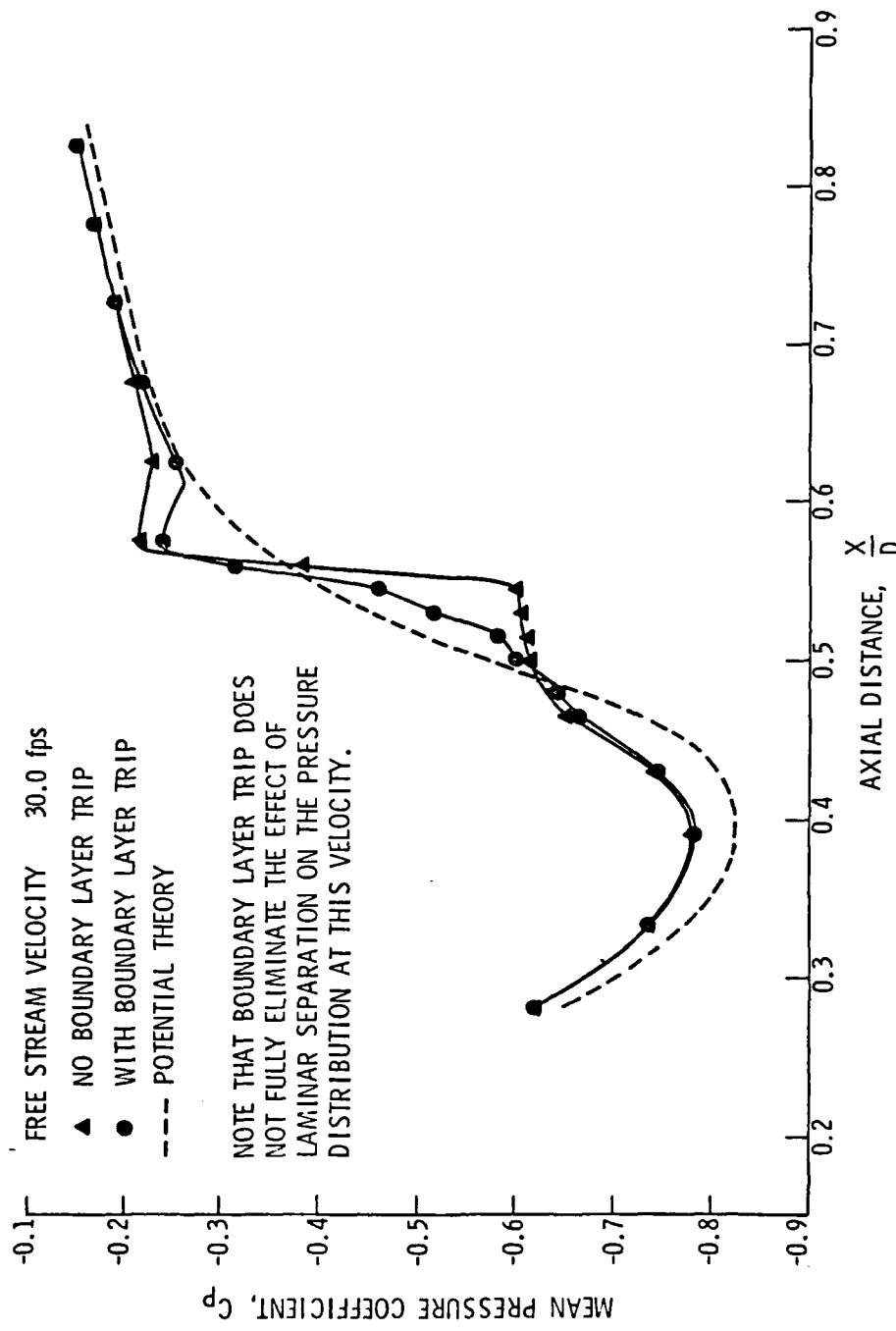


Figure 51. Comparison of measured pressure distributions for a 2.0-in. diameter hemispherical nose with and without a boundary layer trip ($U_\infty = 30.0$ fps).

Arakeri and Acosta [15], who reported laminar separation at a Reynolds number of 9.07×10^5 (60.0 fps) on a 1.813-in. diameter hemispherical nose using Schlieren flow visualization. The calculated value for the critical Reynolds number on a hemispherical nose is given in reference [15] to be 5×10^6 based on the calculation method of Jaffe, Okamura, and Smith [33]. The critical Reynolds number corresponds to the flow condition for which transition is predicted at the theoretical location of laminar boundary layer separation.

The influence of laminar boundary layer separation on the measured pressure distributions is quite evident. A sketch is provided in Figure 52 to define the important features of the pressure distribution curves to be discussed. The locations of transition and reattachment are observed to move systematically upstream for an increase in free stream velocity. The location of transition, $(x/D)_t$, as defined in Figure 52, is plotted against Reynolds number in Figure 53. Also plotted here are transition data which were converted from the separation bubble length data of Arakeri [14] for a 1.813-in. diameter hemispherical nose. Arakeri defines the end of the separation bubble as the position where the free shear layer, visible by Schlieren, disappears as a result of turbulent mixing. In the present investigation, the end of the separation region is arbitrarily located at the transition point as indicated in Figure 52. Good agreement is apparent between these two investigations. The actual location of laminar boundary layer separation cannot be determined accurately from the pressure distributions. The theoretical location of separation

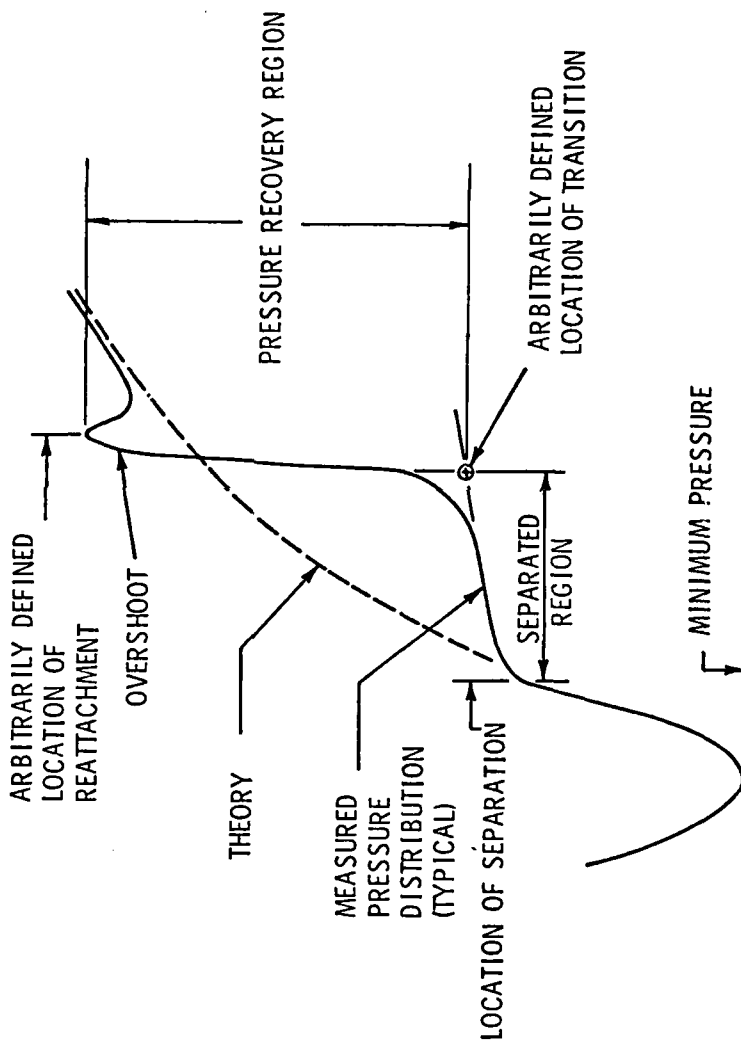


Figure 52. Sketch defining important features of a typical measured pressure distribution for a hemispherical nose.

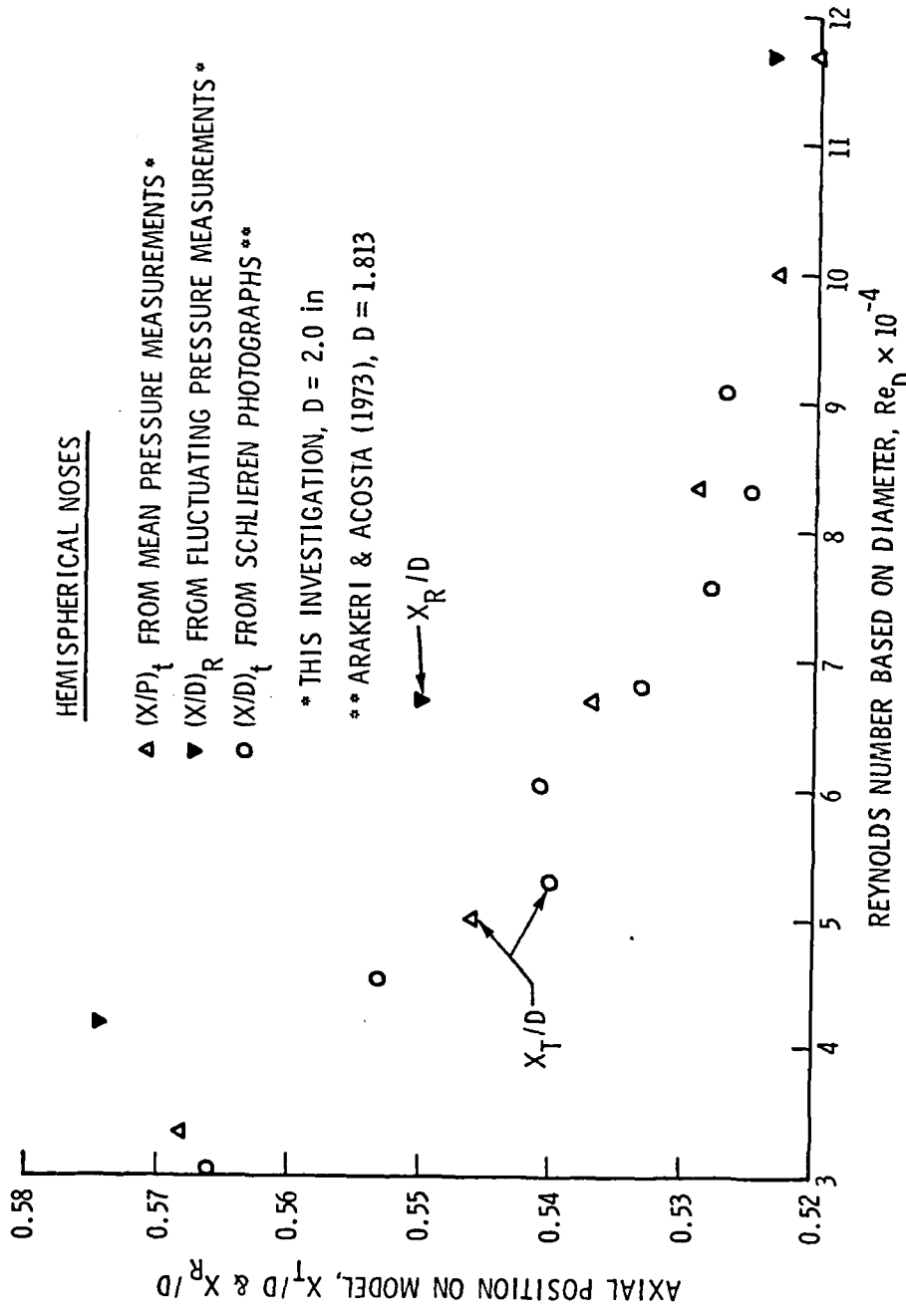


Figure 53. Measured locations of boundary layer transition and reattachment on a 2.0-in. diameter hemispherical nose for variation in free stream velocity.

$[(x/D)_S = 0.462]$ is, however, quite consistent with the data. Also, the data taken at locations very close to the point of laminar boundary layer separation did not show appreciable change with free stream velocity. Both Arakeri and Acosta [15] and Van der Meulen [17] reported that the experimental location of laminar boundary layer separation remains constant with free stream velocity on the hemispherical nose. They also reported good agreement between the theoretical and experimental locations of laminar boundary layer separation.

The indicated region of separation is immediately followed by a pressure recovery region marked by a very steep adverse pressure gradient. Boundary layer reattachment is arbitrarily located at the peak of the small overshoot at the end of the pressure recovery region (refer to Figure 52). For the case where laminar boundary layer separation has been eliminated by a trip, the resulting pressure distribution does not have these characteristic features. Figure 50 shows the pressure distribution for a fully tripped boundary layer at a free stream velocity of 40.0 fps. The measured curve more closely resembles the theoretical curve as expected. Figure 51 shows the pressure distribution for the same tripped hemispherical nose at a velocity of 30.0 fps. Here, the boundary layer trip was not fully effective, as evidenced by the presence of an irregular separation region and an overshoot which is indicative of reattachment.

The results of these mean pressure measurements are significant to the analysis of band cavitation on models which exhibit laminar boundary layer separation. Specific reference is made to these results in the discussion of band cavitation on a hemispherical nose in Section 5.2.1.

CHAPTER 7

PRESENTATION AND DISCUSSION OF FLUCTUATING PRESSURE MEASUREMENTS IN
THE REATTACHMENT REGION OF A 2.0-IN. DIAMETER HEMISPHERICAL NOSE7.1 Introduction

Laminar boundary layer separation on an axisymmetric body is generally accompanied by the turbulent reattachment of the boundary layer a short distance downstream from the separation point. Large velocity and pressure fluctuations exist in the region of reattachment. Measurements show that the turbulent pressure fluctuations found in the region of reattachment are significantly greater than those characteristic of natural laminar boundary layer transition [25,27]. Laminar separation and reattachment often occur in the low pressure region of a body a short distance downstream from the minimum pressure point. Negative peak pressures in the region of reattachment may, therefore, exceed the theoretical value of the minimum pressure of the body. Consequently, the region of boundary layer reattachment is a likely location for cavitation inception. Observations of cavitation inception in the reattachment region of axisymmetric bodies have been reported by Arakeri and Acosta [15], Gates [13], and Van der Meulen [17].

Measurements of the fluctuating pressures in the region of reattachment were reported by Arakeri [26] on a 2.0-in. diameter hemispherical headform in water. He cited peak pressure fluctuations of the order of 26.0 percent of the dynamic pressure at a free stream velocity of about 8.0 fps. His measurements were made using a 0.14-in. diameter, flush-mounted piezoelectric pressure transducer. However, the accuracy

of his results is limited, particularly at high velocities, due to the large size of the transducer relative to the turbulent length scales involved. He noted that increasing effects of spatial averaging were realized as the velocity was increased. These measurements should, therefore, be regarded as a lower limit for fluctuating pressure levels in the reattachment region.

Huang and Hannon [27] measured the pressure fluctuations in the region of transition and reattachment on an axisymmetric body (Forebody S), which also experienced laminar boundary layer separation. The measurements were made in air using pinhole microphones. The root mean square (rms) pressure fluctuations at reattachment, normalized by the dynamic pressure, were found to be an order of magnitude higher than those characteristic of a fully established turbulent boundary layer. The maximum level was reported to be 0.15. Gaster [25] measured velocity fluctuations in the free shear layer above the end of the separated region in a two-dimensional flow setup in air. He reported rms velocity fluctuations to be about $0.16 U_{\infty}$, which also suggests the presence of large pressure fluctuations in this region.

Arakeri [26] performed fluctuating pressure measurements in the laminar boundary layer just upstream of the separation point on a 2.0-in. diameter, 1.5-caliber ogive nose in water. Good agreement was found between the theoretical and experimental values of the critical frequency of Tollmien-Schlichting disturbances in the boundary layer of the model at a free stream velocity of 53.3 fps. This critical frequency corresponds to the most dominant disturbance frequency in the boundary layer. Disturbances having this characteristic frequency

are amplified and often result in transition from a laminar to a turbulent boundary layer. Theoretical calculations of the critical frequency were based on the method of Jaffe, Okamura, and Smith [33]. A brief summary of these calculations is presented by Gates [13]. Transition prediction is based on an empirically determined value of the amplification ratio between initial and final disturbance amplitudes. Transition on an axisymmetric body is suspected to occur for an amplification ratio of e^7 . The critical frequency is that frequency (of an imposed disturbance) which most rapidly produces transition.

Observations of bubble-ring cavitation in the region of boundary layer reattachment on the hemispherical nose have aroused an interest in the magnitude of the fluctuating pressures in this region. In this investigation, fluctuating pressure measurements were made in the reattachment region of a 2.0-in. diameter hemispherical nose in water. Measurements were made with a cavity-mounted piezoelectric pressure transducer in an attempt to minimize spatial averaging due to the finite size of the sensing element. Maximum fluctuation levels were measured for three different free stream velocities corresponding to three different positions on the body. Additional tests were performed with a boundary layer trip on the model to eliminate laminar boundary layer separation. The results of the measurements are presented along with some discussion of the many difficulties encountered in using a cavity-mounted transducer in water. Interpretations of the results are incomplete. The data presented, however, may be useful in subsequent investigations.

7.2 Equipment and Procedure

Fluctuating pressure measurements were performed on a specially-machined 2.0-in. diameter hemispherical headform. The headform was made in two parts so that the instrumentation was accessible by means of a detachable hatch. For details, refer to the photograph in Figure 54. The measurements were made on the outer surface of the hatch and care was taken to ensure that the surface of the hatch conformed to the model contour. Measurements were made at three streamwise locations in order to obtain maximum fluctuating pressure readings for three different velocities.

A piezoelectric transducer, whose active sensing diameter is 0.208-in. was mounted in a cavity which was connected to the flow by means of a 0.0135-in. diameter duct. This arrangement effectively reduced the transducer sensing diameter by a factor of more than 15. As a result, the spatial averaging of the fluctuating signal was significantly reduced by more closely matching the effective transducer size with the characteristic length scales of the turbulence in the boundary layer. A special housing was made to accommodate the transducer and cavity. The housing was anchored inside the hatch at one of three desired measurement locations. Refer to Figure 55 for an illustrative sketch of the transducer mounting arrangement.

Because the transducer was cavity-mounted, the Helmholtz frequency of the duct and cavity had to be considered. A periodic signal having a frequency equal to the Helmholtz frequency will produce standing waves in a cavity and result in an undesirable cavity resonance. Also to be considered was the characteristic maximum frequency, f_{max} ,

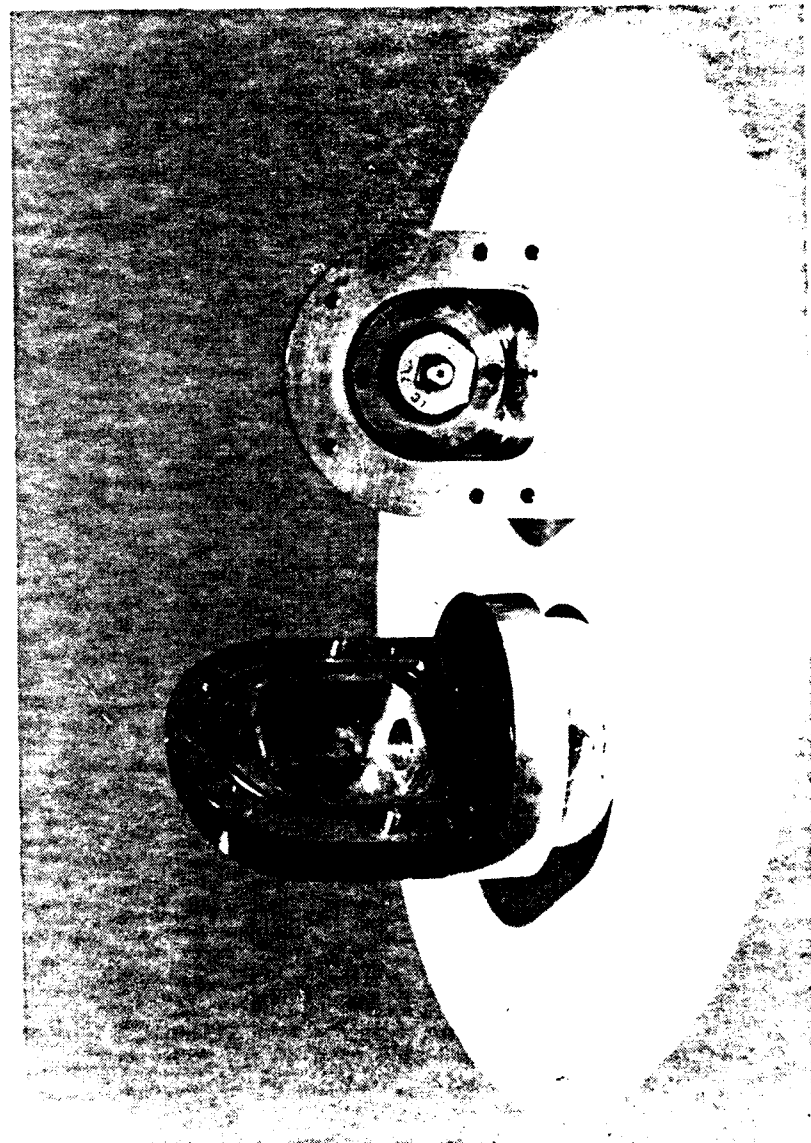


Figure 54. Photograph of instrumented 2.0-in. diameter hemispherical nose used for fluctuating pressure measurements.

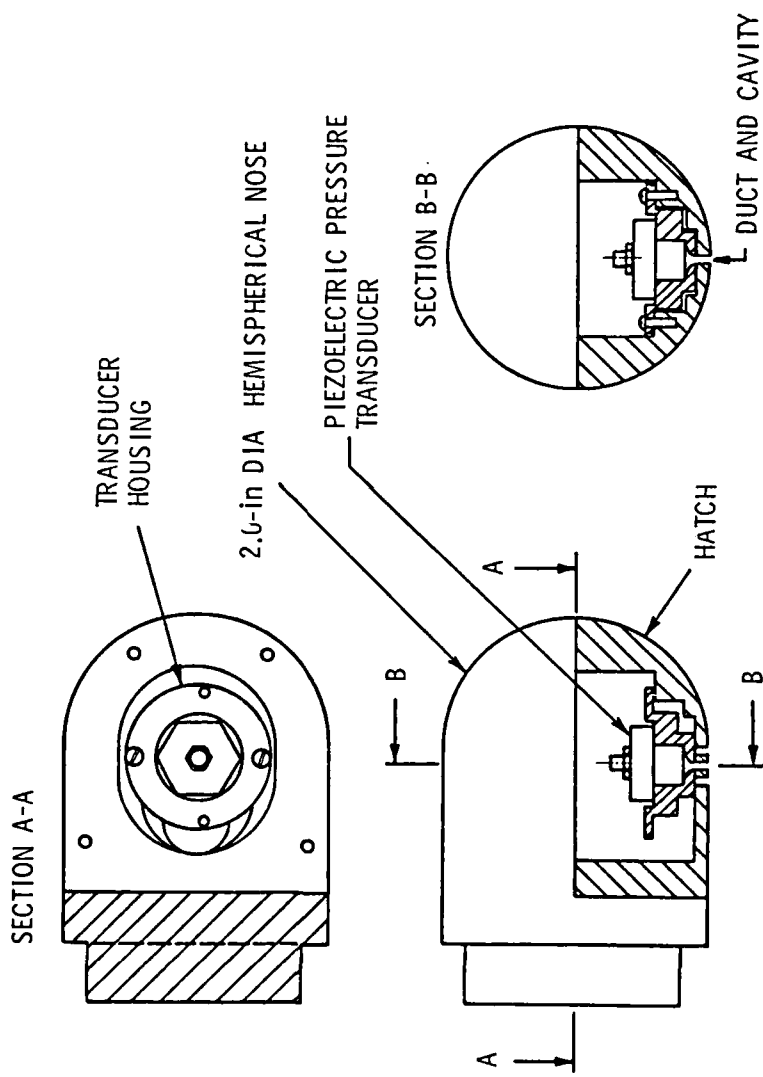


Figure 55. Installation details of a cavity-mounted pressure transducer in a 2.0-in. diameter hemispherical nose.

determined by the local flow and the diameter of the duct. The Helmholtz frequency, f_H , is given by

$$f_H(\text{Hz}) = \frac{c}{2\pi} \sqrt{\frac{3\pi r^2}{4L_d V}} , \quad (26)$$

where

r = radius of duct,

L_d = length of duct,

V = volume of cavity, and

c = sonic speed in water.

The measurable frequency limit (f_{\max}) is calculated by

$$f_{\max}(\text{Hz}) = \frac{U_L}{2\pi d} , \quad (27)$$

where

U_L = local flow velocity, and

d = diameter of duct.

The response of a cavity-mounted transducer is generally linear for frequencies below f_H . The duct and cavity dimensions should, therefore, be designed so that the calculated value of f_H is greater than or equal to f_{\max} . For the present investigation, the value of f_{\max} was calculated to be about 12.5 kHz for a free stream velocity of 70.0 fps. The cavity and duct arrangement were, therefore, designed to produce a f_H of approximately 13 kHz.

The actual measurements were made with an LC-71 piezoelectric transducer made by Cellesco Corporation. A charge amplifier made by Endevco was used to boost the transducer signal. Three series of

measurements were performed, each corresponding to a different location on the hemispherical headform. Transducer locations for Series 1, 2, and 3 were $x/D = 0.575$, 0.550, and 0.525, respectively, where x/D is the nondimensionalized axial distance along the model.

The originally proposed experimental procedure is described below. Unfortunately, a resonance occurred in the transducer cavity which appeared predominately in the turbulent signal. As a result, peak pressure fluctuations from an oscilloscope trace and wide-band rms levels were unreliable and could not be used.

Peak fluctuating pressure levels, wide-band rms levels, and narrow-band rms power spectra were the three types of information that were desired from each of the three transducer locations. For each location, the tunnel velocity was to be varied until a maximum wide-band rms signal was obtained. A Disa true rms meter was used for this purpose. Small adjustments of the velocity shifted the location of reattachment and a maximum rms reading from the transducer indicated that reattachment was occurring at the location of measurement. Having achieved this condition, the power spectrum of the signal was to be recorded. Also, information on peak pressure fluctuations was to be obtained from the signal trace on the oscilloscope. The same type of information was to be obtained for the case of an artificially tripped boundary layer. Because of the aforementioned problem with the resonance, the procedure was modified and will be discussed in the results.

7.3 Results of Fluctuating Pressure Measurements

The results of the fluctuating pressure measurements in the reattachment region of a 2.0-in. diameter hemispherical headform are presented here and are then briefly discussed. The data are shown as rms pressures (60.0 Hz bandwidth) normalized by the dynamic pressure ($1/2 \rho U_\infty^2$) as a function of the Strouhal number based on the length of the separation region. (The appropriate lengths for the separation region were calculated from the data in Figure 53, which shows the locations of boundary layer reattachment on a 2.0-in. diameter hemispherical nose versus Reynolds number.) Figures 56, 57, and 58 show plots for several test velocities at measurement locations of $x/D = 0.575, 0.550$, and 0.525 , respectively.

The original test results were complicated by the effects of a resonance in the cavity over the transducer as mentioned previously. Details of the calibration which was performed to correct for this problem are presented in Appendix B. A description of the entire data reduction procedure is given in Appendix C.

The proposed scheme to find the actual pressure fluctuation levels at three different velocities involved adjusting the velocity to get a maximum reading on a rms meter (wide band) for each of three transducer locations. Unfortunately, the resonance of the transducer cavity influenced the readings and this method was not considered reliable. Instead, three series of power spectra (one for each transducer position) were recorded for several velocities and then corrected for the effect of the resonance. The power spectra indicating the greatest amount of energy in each series were then considered.

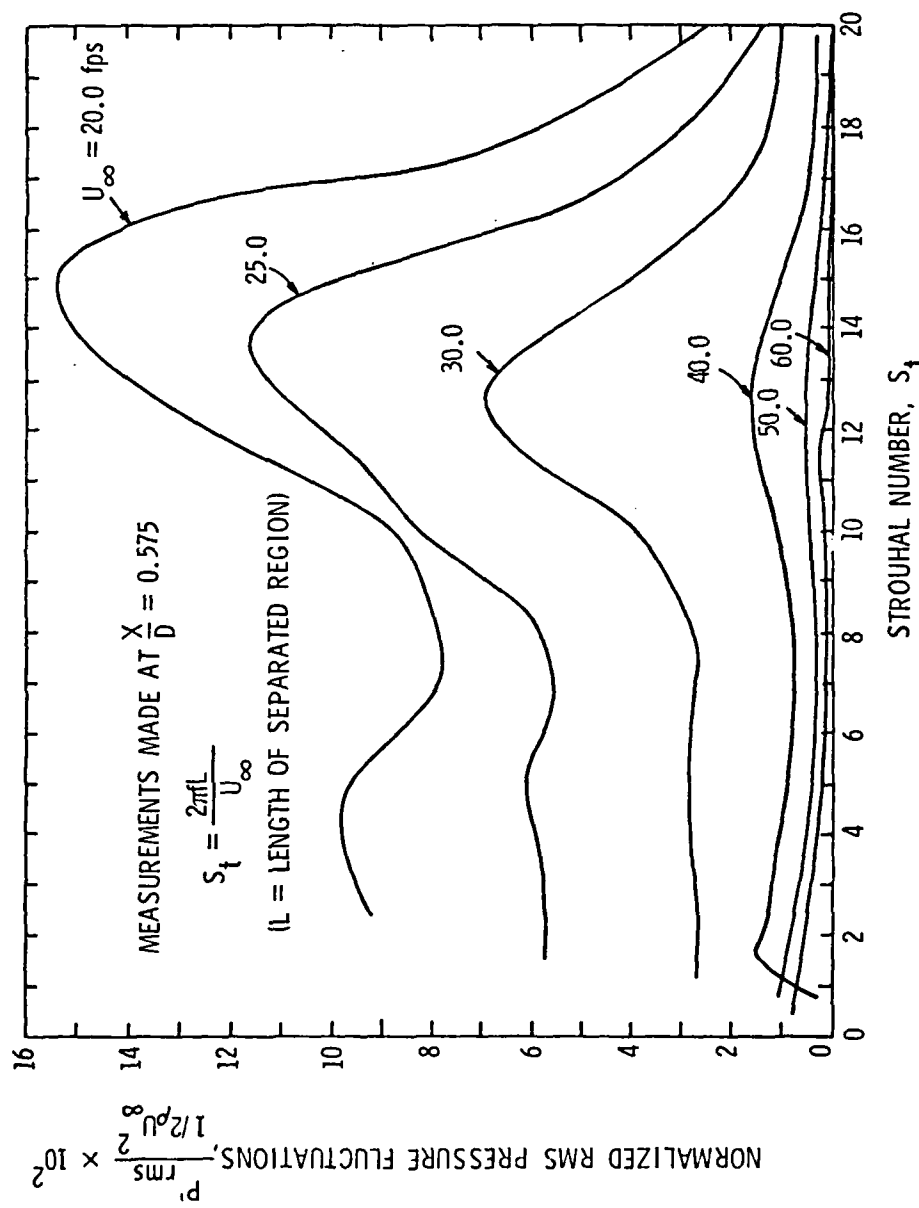


Figure 56. Levels of normalized rms pressure fluctuations on a 2.0-in. diameter hemispherical nose as a function of Strouhal number for several values of free stream velocity (measured at $x/D = 0.575$).

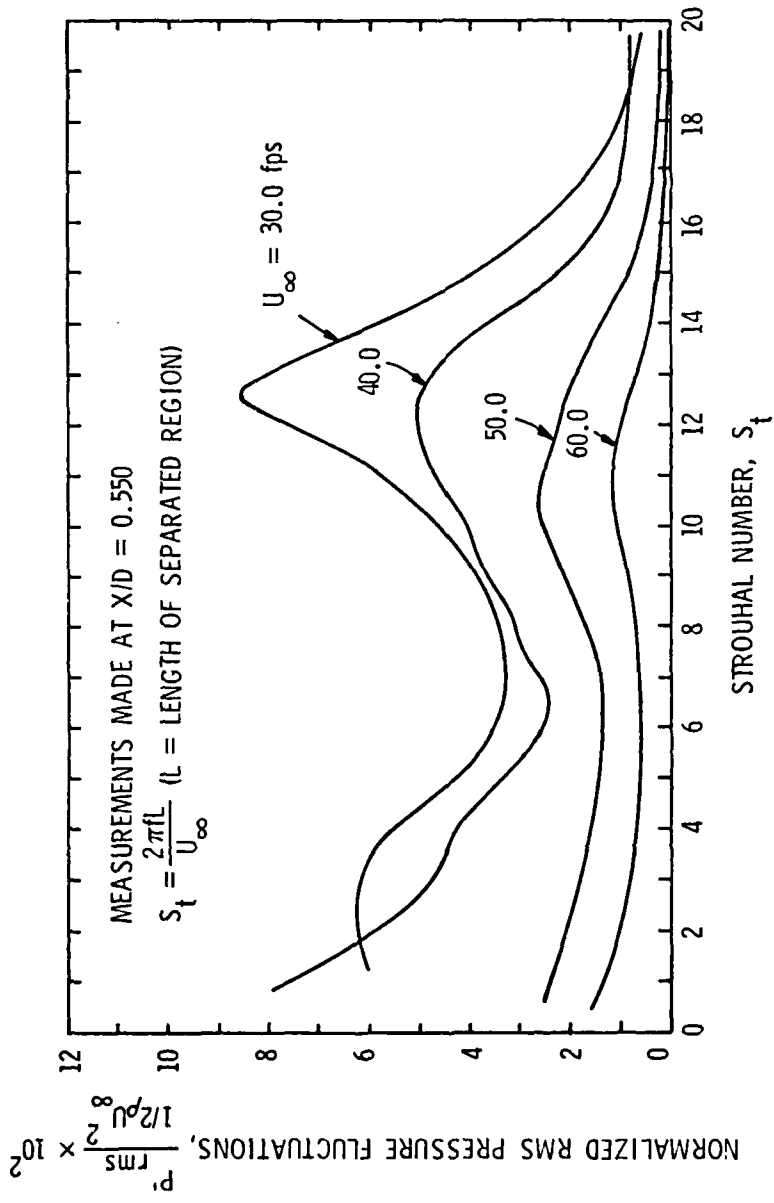


Figure 57. Levels of normalized rms pressure fluctuations on a 2.0-in. diameter hemispherical nose as a function of Strouhal number for several values of free stream velocity (measured at $x/D = 0.550$).

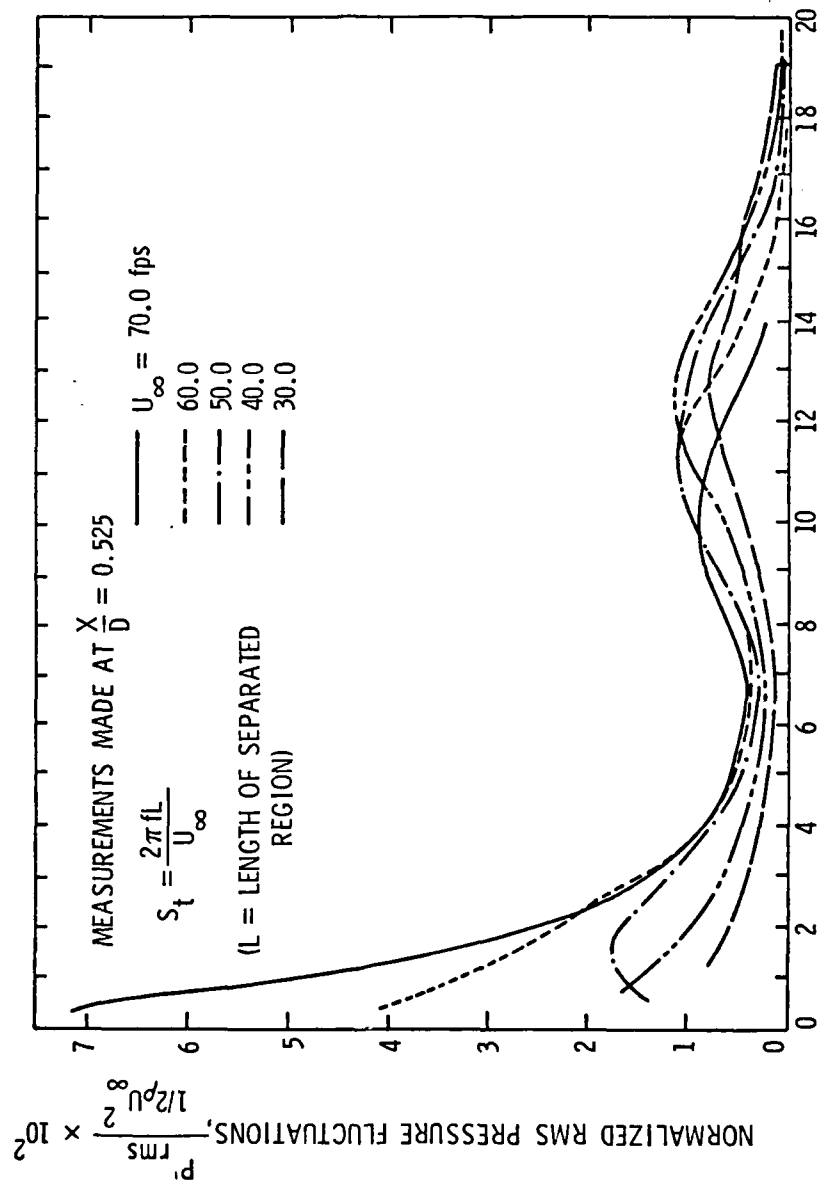


Figure 58. Levels of normalized rms pressure fluctuations on a 2.0-in. diameter hemispherical nose as a function of Strouhal number for several values of free stream velocity (measured at $x/D = 0.525$).

Three curves corresponding to these maximum levels are presented in Figure 59 as plots of rms pressure, nondimensionalized by the dynamic head, versus frequency. Figure 60 shows the same data as a function of the Strouhal number, S_t , based on the length of the separation region. Figures 61 and 62 are presented to show the effect of a boundary layer trip on the turbulent pressure fluctuations for free stream velocities of 40.0 and 70.0 fps, respectively.

7.4 Discussion

All fluctuating pressure signals were measured on a real-time signal analyzer over a frequency range of 0.5 to 20.0 kHz with a rms bandwidth of 60.0 Hz. In general, two peaks were observed in the power spectra of the measured signals for most velocities. The higher frequency peaks shifted with free stream velocity and suggest a Strouhal effect, whereas the lower frequency peaks did not show this shift. As a function of the Strouhal number (Figures 56, 57, and 58), the higher frequency peaks all occurred within the Strouhal number range of 10.0 to 14.0. The occurrence of two energy peaks is in agreement with the results of Arakeri [26], who also measured fluctuating pressures in the reattachment region, on a 2.0-in. diameter hemispherical headform. He associates the lower frequency energy peak with the oscillatory nature of the reattachment region and the higher frequency peak with transitional waves of the free shear layer. This explanation is consistent with the results of this investigation. Figure 63 is a sketch illustrating this idea. Both energy peaks are definitely associated with the presence of boundary layer separation as indicated by the results for the two tripped cases presented in

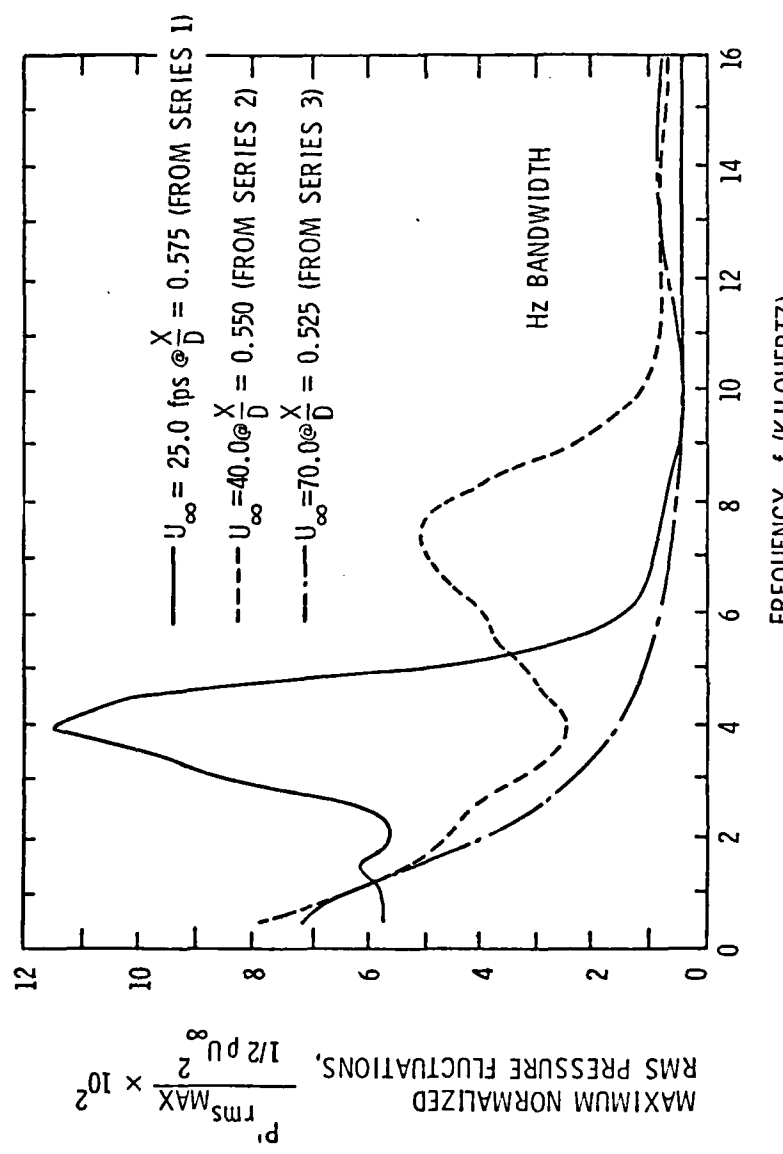


Figure 59. Maximum normalized rms pressure fluctuation levels plotted against frequency for three different free-stream velocities on a 2.0-in. diameter hemispherical nose.

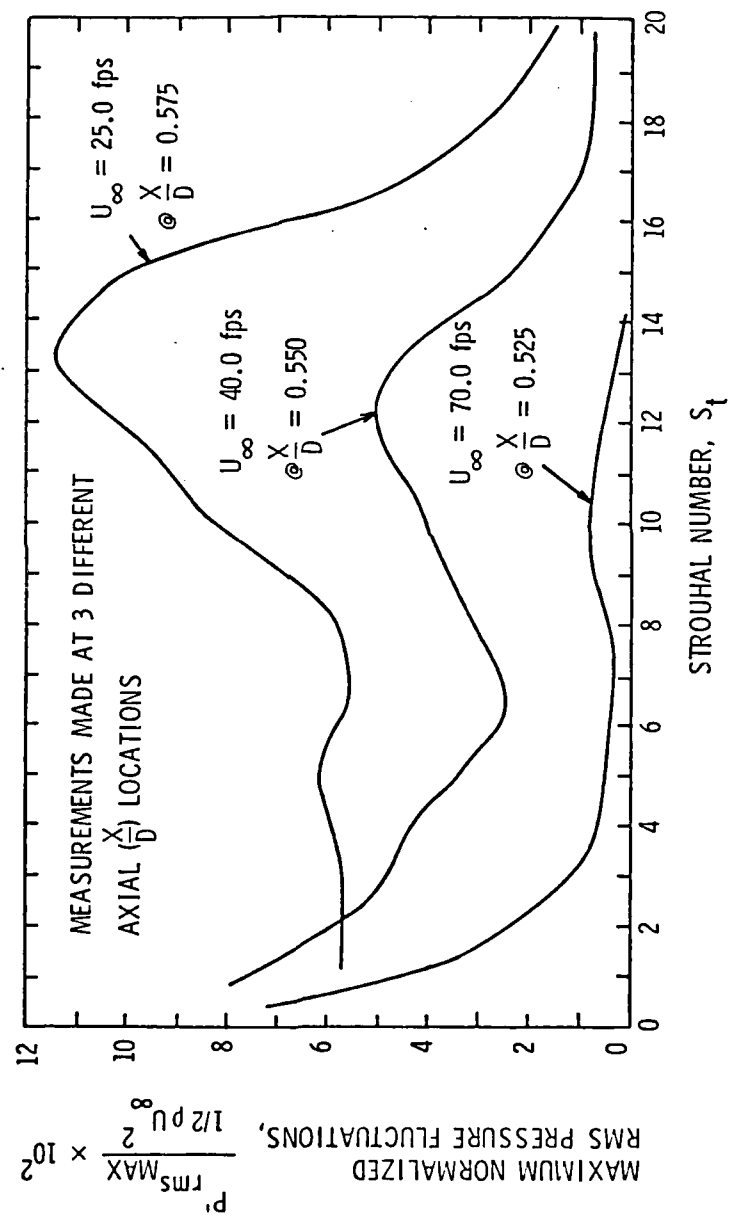


Figure 60. Maximum normalized rms pressure fluctuation levels plotted against Strouhal number for three different velocities on a 2.0-in. diameter hemispherical nose.

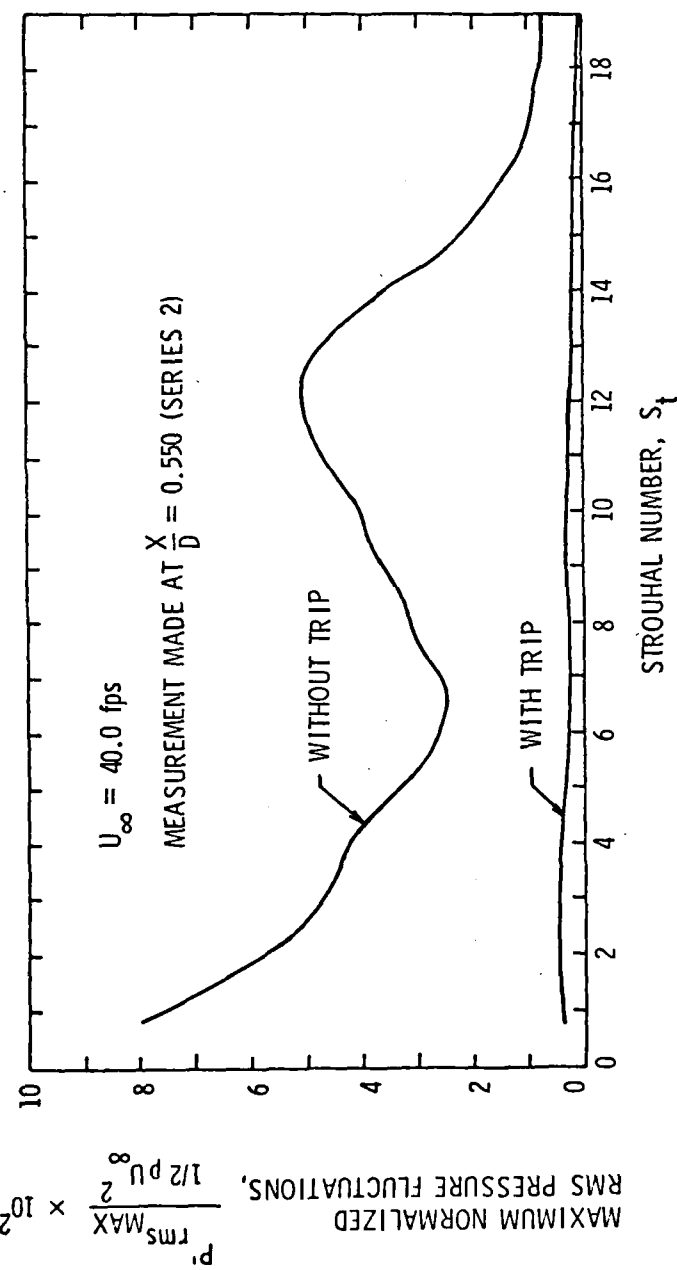


Figure 61. Maximum normalized rms pressure fluctuation levels versus Strouhal number for a tripped and a nontripped 2.0-in. diameter hemispherical nose (measured at $x/D = 0.550$).

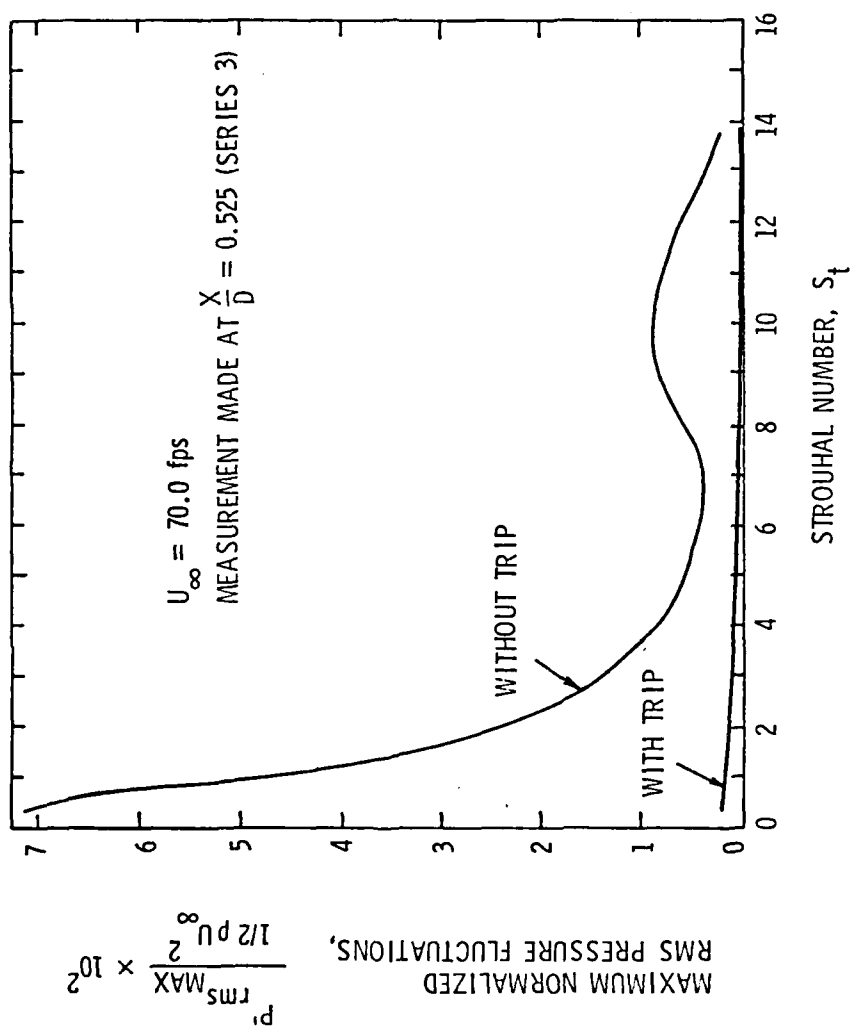


Figure 62. Maximum normalized rms pressure fluctuation levels versus Strouhal number for a tripped and a nontripped 2.0-in. diameter hemispherical nose (measured at $x/D = 0.525$).

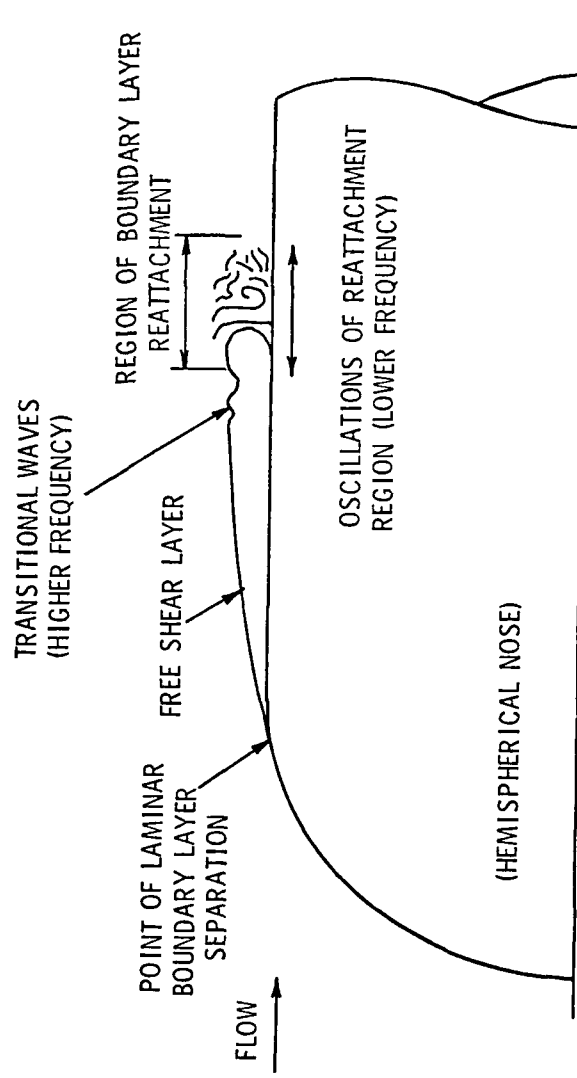


Figure 63. Sketch illustrating lower and higher frequency contributions to the turbulent energy of transition and reattachment on a 2.0-in. diameter hemispherical nose.

Figures 61 and 62. By eliminating boundary layer separation, the fluctuating pressure level was decreased considerably and both energy peaks were completely eliminated.

Results similar to those for a tripped boundary layer were observed for the case when reattachment occurred a sufficient distance upstream from the point of measurement. Apparently, a fully attached turbulent boundary layer develops rapidly and the pressure fluctuations associated with transition and reattachment quickly die out with distance. This is indicated in Figure 56 for free stream velocities of 50.0 and 60.0 fps. The distance from reattachment to the point of measurement is approximately 0.035 and 0.044 body diameters, respectively. Both spectral curves indicate relatively low turbulent pressure energy with no significant energy peaks. These curves are, in fact, very similar to those obtained for tripped boundary layers shown in Figures 61 and 62.

Maximum rms pressure fluctuation levels, $P'_{\text{rms MAX}}$, were observed for free stream velocities of 24.0, 40.0, and 70.0 fps, thereby indicating the corresponding positions of reattachment at $x/D = 0.575$, 0.550, and 0.525, respectively. These three cases are presented as plots of normalized rms pressure versus frequency in Figure 59. Two energy peaks are evident on all three curves. Frequencies corresponding to the higher frequency peaks are 4.0, 7.5, and 14.0 kHz for $U_\infty = 25.0$, 40.0, and 70.0 fps, respectively. Lower frequency peaks all occurred at approximately 500 Hz. Figure 64 shows two separate plots of normalized peak levels which correspond to the lower and higher frequency energy peaks (from Figure 59) versus velocity.

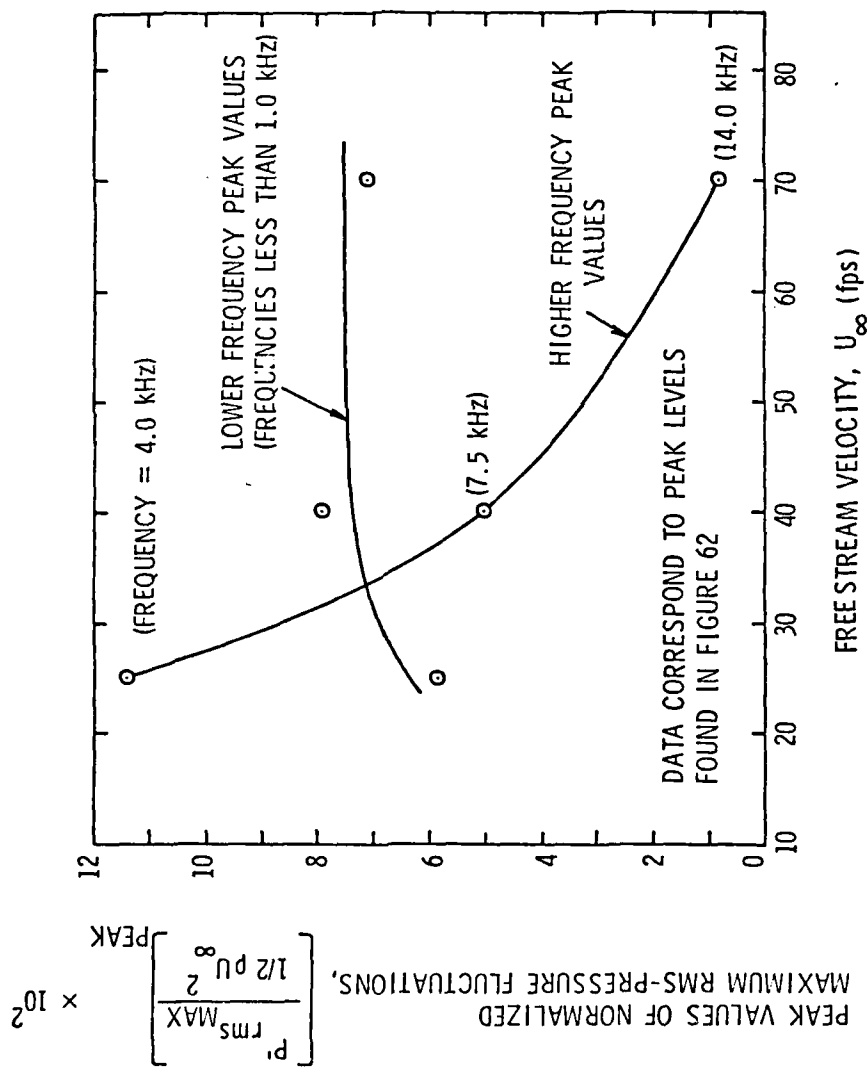


Figure 64. Variation in peak values of normalized maximum rms pressure fluctuations with velocity for higher and lower frequency energy peaks.

The level of the higher frequency peaks which corresponds to transitional energy decreased approximately as one over the square of the velocity. The maximum level or normalized $P'_{rms,MAX}$ of 0.114 occurs at a free stream velocity of 25.0 fps for this higher frequency case. The level of the lower frequency peaks which is associated with the oscillatory nature of reattachment is nearly constant with velocity. At free stream velocities of 70.0 and 40.0 fps, the averaged value of the normalized $P'_{rms,MAX}$ is approximately 0.075 and drops to about 0.059 at $U_\infty = 25.0$ fps.

For the sake of comparison, the three positions of maximum pressure fluctuations are presented as a function of their corresponding indicated free stream velocities in Figure 53. This graph shows plots of transition location versus velocity for a hemispherical headform. The trends show good agreement. It can be seen that the positions of maximum pressure fluctuations corresponding to reattachment occur just downstream of the measured locations of transition. This result is expected since transition always precedes reattachment in the streamwise sense.

The measured peak frequencies corresponding to the transitional waves (higher frequency) on the free shear layer appear to agree reasonably well with the calculated Tollmien-Schlichting frequencies estimated by the method of Jaffe, Okamura, and Smith [33]. In Figure 65, the peak frequencies (some are averages) measured on the hemispherical headform for several velocities are compared with the calculations performed by Gates [13] for a 2.0-in. diameter hemispherical nose. The calculations were carried out at the theoretical

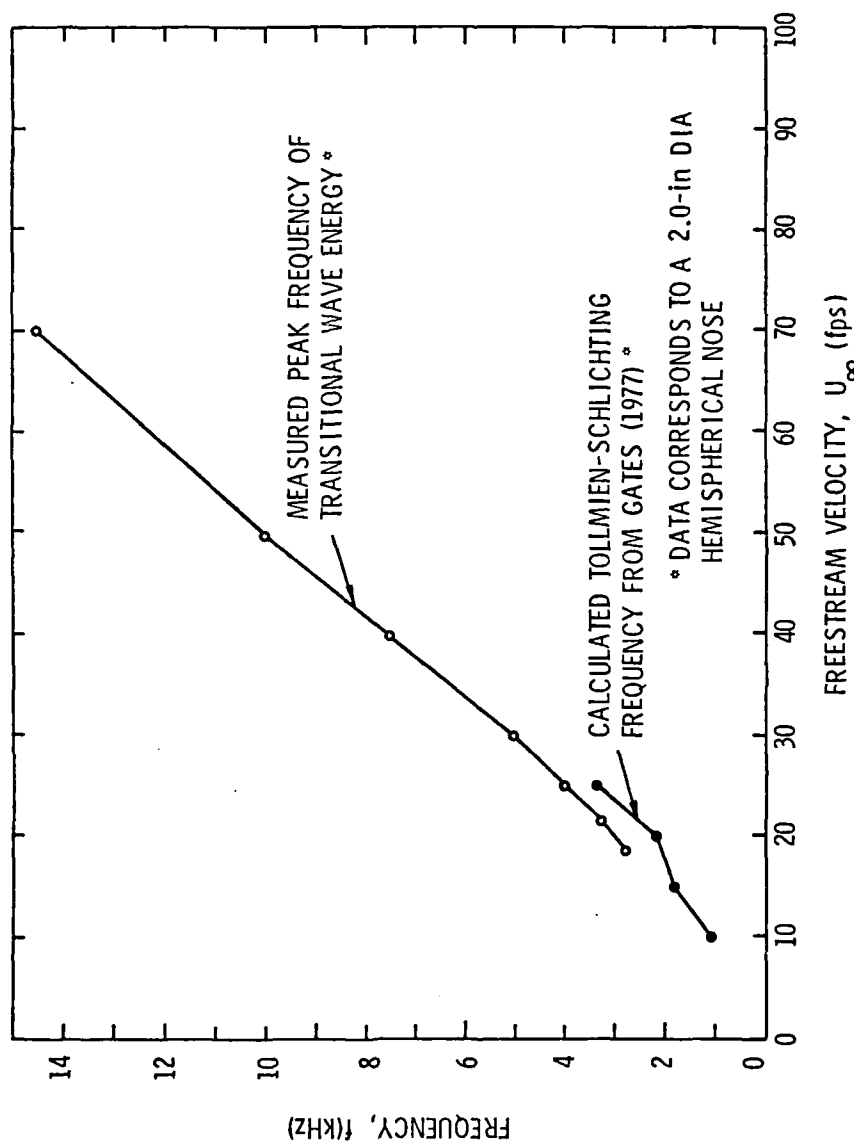


Figure 65. Comparison of measured peak frequencies of transitional wave energy with calculated Tollmien-Schlichting frequencies for several free stream velocities.

location of boundary layer separation. Such agreement seems remarkable since the theory assumes an attached laminar boundary layer, whereas the measurements were made in the presence of a separated laminar shear layer. Arakeri [26] also reports very good agreement between Smith's method and the measured critical frequency on a 2.0-in. diameter, 1.5-caliber ogive nose. In this case, however, the measurement was made upstream of separation in presumably an attached laminar boundary layer.

Bubble-ring cavitation on the hemispherical nose occurs in the region of boundary layer reattachment. Its transient nature suggests that it occurs as a result of the fluctuating pressures measured in this region. It is not known, however, which energy peak (higher or lower frequency) may be responsible. Bubble-ring cavitation predominates at high velocities. This suggests that the higher frequency energy is not as important since its level drops off rapidly with velocity. At 70.0 fps the lower frequency peak at a level of 0.071 is greater than the higher frequency peak by a factor of nine (see Figure 64).

These pressure fluctuation data are related to cavitation on the hemispherical nose by Equations (20) and (21). The value of $\Delta\sigma$ [Equation (20)] is estimated from Figure 21 to be 0.03. Therefore, from Equation (21), it can be seen that

$$\frac{\frac{P'}{r}}{\frac{1}{2} \rho U_\infty^2} = 0.03 , \quad (28)$$

where P'_r is the instantaneous pressure fluctuation in the reattachment region. Since instantaneous peak readings are greater than rms values, the fluctuating pressure data should be considered as a lower limit for the actual pressure fluctuations. In any event, bubble-ring cavitation appears to be produced by pressure fluctuations whose non-dimensionalized level is approximately 0.03. This result suggests that the lower frequency energy is responsible for bubble-ring cavitation. Figure 64 shows that the higher frequency energy level at 70.0 fps is less than 0.01 and, therefore, rather low to be considered important. This result is not conclusive, however, because information on instantaneous pressure fluctuations at these two frequency ranges is not available. Normally, instantaneous pressure readings are taken directly from an oscilloscope trace of the signal. Because of the cavity resonance which was present in all of the tests, instantaneous pressure readings were unreliable. An additional point to consider here is that bubble-ring cavitation on the hemispherical nose is observed adjacent to the model surface; this suggests its origin is in the turbulent region of reattachment rather than away from the body in the free shear layer. Photographs of bubble-ring cavitation and boundary layer visualization by Van der Meulen [17] for a 10.0 mm (0.4-in.) diameter hemispherical headform show this quite clearly.

CHAPTER 8

SUMMARY, CONCLUSIONS, AND RECOMMENDATIONS FOR
FUTURE STUDIES8.1 Summary

Several types of limited cavitation were observed on the three models tested in the present investigation. Four basic types were noted and are listed below:

- 1) transient cavitation,
- 2) band cavitation,
- 3) fixed-patch cavitation, and
- 4) developed cavitation.

Two general forms of transient cavitation were observed, namely, travelling cavitation and bubble-ring cavitation. Travelling cavitation was the most frequently observed type of cavitation and occurred on all three models. Two forms of travelling cavitation were noted, namely, travelling-bubble and travelling-patch cavitation. Travelling-patch cavitation was observed mostly at higher velocities (50.0 to 70.0 fps) when very few bubbles were visible in the free stream. This form of transient cavitation was generally not seen on the hemispherical nose. Travelling-bubble cavitation was observed on all three models, most notably, at low velocities (20.0 to 30.0 fps) when free stream bubbles were visible in the test section. In general, for travelling cavitation, σ_L decreased with an increase in velocity and increased with an increase in air content. Simple calculations were performed to obtain R_{max} , the radius of the largest nuclei present in the flow and those assumed to produce cavitation at the minimum pressure of the particular model for

conditions of limited cavitation from σ_{ℓ} data. The results suggested that, for the three models at a particular velocity, a relatively small range of nuclei sizes was involved in limited travelling cavitation. Secondly, for an increase in the tunnel velocity from 20.0 to 70.0 fps the average value of R_{max} decreased by two orders of magnitude. Similar trends were noted in the values of R_{max} calculated from limited travelling cavitation data from various other models and test facilities.

Band cavitation was observed on the hemispherical nose at all test velocities and on the DTNSRDC nose for velocities of 30.0 fps or less. Band cavitation only occurred when laminar boundary layer separation was present. The value of σ_{ℓ} for band cavitation increased slightly with an increase in velocity and showed little variation with a change in air content. A unique form of transient cavitation, namely, bubble-ring cavitation, was observed only on the hemispherical nose and is apparently associated with the pressure fluctuations in the boundary layer reattachment region. The trend in σ_{ℓ} with velocity for bubble-ring cavitation was similar to that for band cavitation. For low values of air content (less than four parts per million) bubble-ring cavitation did not occur.

Fixed-patch cavitation occurred on the Schiebe and DTNSRDC noses, most notably at higher velocities (40.0 to 70.0 fps). This type of cavitation formed despite efforts to keep the model surfaces polished and free of roughness. The value of σ_{ℓ} for fixed-patch cavitation increased significantly with an increase in free stream velocity. Free stream bubbles which were associated with high air content appeared to suppress the formation of fixed-patch cavitation or cause the cavities

to become unsteady. This type of cavitation was occasionally observed on the hemispherical nose, however, cleaning the model eliminated its formation.

The Schiebe and the DTNSRDC noses both exhibited developed cavitation which resulted in a dramatic change in the flow characteristics of each body. The value of σ_{ℓ} for developed cavitation increased significantly with an increase in free stream velocity, but changed little with air content.

Mean pressure measurements over a 2.0-in. diameter hemispherical nose indicate laminar boundary layer separation at a free stream velocity of 70.0 fps ($Re_D = 1.17 \times 10^6$). The value of σ_{ℓ} for band cavitation appears to scale approximately with the experimentally derived value of pressure coefficient at the location of transition, C_{p_t} .

Results of fluctuating pressure measurements on the hemispherical nose in the region of boundary layer reattachment were presented. The results suggest that turbulent energy in this region comes from two sources, namely, transitional waves on the free shear layer and oscillations of the reattachment region. These results were initially given by Arakeri [26]. The energy from the oscillations of reattachment may be associated with the formation of bubble-ring cavitation. Further analysis of these measurements, although not within the scope of this investigation, may be helpful in understanding the relationship between fluctuating pressures and cavitation inception.

8.2 Conclusions

The following conclusions are based on results from the present investigations:

1. The nuclei characteristics of a particular test facility play a major part in determining the travelling cavitation characteristics of a test body, regardless of the body shape or size. In the present facility, travelling cavitation was observed on all three noses.

Observations of bubbles in the free stream indicated that the number and size of free stream nuclei increased with decreasing test velocity during the course of a routine limited cavitation test. The limited cavitation number also increased for decreasing test velocities. A decreasing trend in σ_L with velocity for travelling cavitation was also reported by Van der Meulen [17] for a 10-mm diameter Schiebe nose and Schiebe [20] for a 0.625-in. diameter ITTC nose. Gates [13] concluded that for models which exhibited laminar boundary layer separation, removal of laminar separation resulted in travelling-bubble cavitation. The value of the limited cavitation number for this type of cavitation generally depends on the nuclei population.

The characteristic size of free stream nuclei in a recirculating water tunnel facility may change dramatically during the course of a cavitation test. Visual observations during limited cavitation tests in the present investigation indicate that much larger nuclei occur at lower tunnel speeds. Generally, at high tunnel speeds free stream nuclei were too small to see. This effect is a consequence of lower tunnel pressure occurring at the lower velocities and is enhanced by increased air content. Simple calculations showed an increase in free

stream nuclei size by nearly two orders of magnitude during the course of a single test. Similar results were obtained from various other water tunnel facilities.

2. Axisymmetric laminar boundary layer separation may have a significant effect on the cavitation characteristics of a body. The separation region provides a site for attached band cavitation. On some models, the pressure fluctuations in the region of boundary layer reattachment produce bubble-ring cavitation.

Mean pressure measurements over a 2.0-in. diameter hemispherical nose showed that transition and reattachment moved upstream for increased free stream velocity (see Figure 49). Limited cavitation data for band cavitation on this body scale very well with the measured value of pressure coefficient associated with an arbitrarily defined point of transition [refer to Section 5.2.1.1, Figure 44 and Equation (17)]. It is believed that the tendency for σ_{ℓ} (band) to increase with velocity is due to the corresponding movement of transition closer to the minimum pressure point. It appears that for all bodies which exhibit band cavitation Equations (18) and (19) hold for measured or calculated values of $C_p S$. This relationship is in agreement with the results of Arakeri and Acosta [15] for an ITTC nose but differs from their results for a hemispherical nose. No reason can be given for this discrepancy, however, their limited cavitation data seem quite high as shown in Figure 44.

Complete removal of laminar boundary layer separation resulted in the elimination of all traces of band cavitation from the hemispherical nose (see Figures 27 and 28). From cavitation observations on a

tripped hemispherical nose, it is believed that, in general, if laminar separation is entirely removed from a model no attached form of band cavitation will appear. This conclusion appears to be inconsistent with the results of Arakeri and Acosta [15], Van der Meulen [17], and Gates [13], who observed attached cavities which they described as intermittent and rough forms of band cavitation in the presence of a presumably tripped boundary layer. It is suspected that, in these cases, separation occurred intermittently or the separation region was not completely removed.

Fluctuating pressure measurements in the reattachment region of a 2.0-in. diameter hemispherical nose revealed the existence of two fluctuating contributions, namely, higher frequency transitional waves on the free shear layer and lower frequency oscillations of the reattachment region. This result is in agreement with the observations of Arakeri [26]. Characteristic frequencies of the energy associated with transitional waves increased with velocity and correlated well with the Strouhal number based on measured separation length and free stream velocity. The level of rms pressure (normalized by $1/2 \rho U_\infty^2$) for this higher frequency energy dropped off very nearly as the inverse of the square of the free stream velocity. Turbulent pressure energy associated with the oscillatory nature of reattachment has a relatively low characteristic frequency (under 1.0 kHz), which did not appear to change with velocity. Nearly constant rms pressure fluctuations of the order of 7.0 percent of the dynamic head were measured.

The equation for limited bubble-ring cavitation is given by Equation (21) (see Chapter 5, Section 5.2.1.4). From limited cavitation

data for band and bubble-ring cavitation, we find that $P'_r / 1/2 \rho U_\infty^2 \approx 0.03$, and is nearly constant with velocity. The results of pressure fluctuation measurements are all rms values. They are, therefore, assumed to be an indication of the lower limit for the instantaneous pressure levels ($\sqrt{P'_r} < P'$). Since it was found that for the lower frequency energy $\sqrt{P'_r} / 1/2 \rho U_\infty^2 \approx 0.07$; this energy contribution is, therefore, suspected to be the important mechanism for bubble-ring cavitation on the hemispherical nose. Turbulent pressure energy from higher frequency transitional waves is not believed to be important to the formation of bubble-ring cavitation on this body. The rms pressure level for the higher frequency energy on the hemispherical nose was observed to increase significantly with a decrease in velocity. This trend may be related to the increasing size of the separation region. Therefore, this high frequency source may be important on bodies which exhibit a larger separation region. For example, bubble-ring cavitation has been observed in the region of the free shear layer on the 1/8-caliber ogive nose; a body which exhibits a large separation region as shown by Arakeri, Carroll, and Holl [34].

3. The occurrence of attached cavitation on a body whose boundary layer is theoretically predicted not to separate strongly suggests the presence of cavitation-induced boundary layer separation. This statement is supported by the observations of both fixed-patch and developed cavitation on the DTNSRDC and Schiebe noses which correspond to cases of attached boundary layer flow. It is believed that initial cavitation produces a disturbance which causes flow separation. This separation region then, in turn, provides a site for an attached cavity.

This hypothesis is further supported by the fact that the leading edges of both fixed-patch and developed cavitation always seems to occur just downstream of the minimum pressure location in a strong adverse pressure gradient. The boundary layer in this region is quite prone to laminar separation.

The observations of fixed-patch cavitation indicate the need for further studies to better understand the mechanisms involved in its formation. Unanswered questions associated with fixed-patch cavitation include the following:

- 1) How does fixed-patch cavitation become attached to a seemingly smooth model? What types and sizes of surface roughness are involved?
- 2) Why do limited cavitation data decrease for an increase in air content?
- 3) Why is fixed-patch cavitation predominant on the Schiebe and DTNSRDC noses but only rarely observed on the hemispherical nose?
4. Several different types of limited cavitation were observed on three different axisymmetric models in the present investigation. A summary chart is presented in Table 3 listing the types of cavitation and their characteristics. The observations of such varied types of limited cavitation on axisymmetric models suggests the following points:
 - 1) In documentation of any limited cavitation tests, a detailed description of the observed cavitation types should accompany the cavitation data. Quantitative information about free stream nuclei is also important.

Table 3
Summary of Cavitation Observations

Type of Cavitation	Observed on Following Nose(s)	Cavitation Class of		Boundary Layer Status Present	Attached	Velocity	Air Content	Trend in σ_L with:
		Laminar	Separated					
Travelling-Bubble	Hemispherical Schieber DTNSRDC	Yes	Yes	Yes	Yes	$\frac{\partial \sigma_L}{\partial U_\infty} < 0$	$\frac{\partial \sigma_L}{\partial \alpha} > 0$	
	Schieber DTNSRDC	No	Yes	Yes	Yes			
Travelling-Patch	Hemispherical	Yes	Yes	No	No	> 0	≈ 0	
	Schieber DTNSRDC	No	Yes	Yes	Yes	> 0	≈ 0	
Bubble-Ring	Hemispherical	Yes	Yes	Yes	Yes	$\frac{\partial \sigma_L}{\partial U_\infty} < 0$	$\frac{\partial \sigma_L}{\partial \alpha} > 0$	
	Schieber DTNSRDC	No	Yes	No	No			
Band	Hemispherical DTNSRDC	Yes	Yes	Yes	Yes	> 0	≈ 0	
	Schieber DTNSRDC	No	No	No	No	> 0	≈ 0	
Fixed-Patch	Hemispherical DTNSRDC	No	Yes	Yes	Yes	> 0	< 0	
	Schieber DTNSRDC	No	Yes	Yes	Yes	> 0	≈ 0	
Developed	Hemispherical DTNSRDC	No	No	No	No	> 0	≈ 0	
	Schieber DTNSRDC	Yes	Yes	Yes	Yes	> 0	≈ 0	

- 2) When making comparisons between cavitation characteristics of different models, one must consider not only the cavitation data but also the type of cavitation that the data represent and the associated free stream nuclei characteristics.

8.3 Recommendations for Future Studies

The present investigation of limited cavitation on axisymmetric models has provided some insight into the mechanisms involved in the cavitation process. Secondly, this investigation has yielded numerous unanswered questions which require further work. The following is a list of recommendations for future studies:

- 1) Investigate limited cavitation on bodies with surface roughness (isolated and/or distributed, indentations and/or extrusions) which are located in a strong adverse pressure gradient. Also, the effects of laminar and turbulent boundary layers should be studied. These recommendations would be helpful in understanding fixed-patch cavitation.
- 2) Perform a theoretical analysis of travelling-bubble cavitation. Using measured values for initial nuclei size, perform calculations and compare the results with observed bubble growth.
- 3) Perform an investigation of the effects of temperature and/or nuclei population on bubble-ring cavitation.
- 4) Perform further analysis of the fluctuating pressure data presented in Chapter 7 and relate the results to bubble-ring cavitation.
- 5) Investigate the cavitation characteristics of additional models including axisymmetric bodies and hydrofoils.

- 6) Conduct a photographic study of the various forms of transient cavitation using both still and high-speed motion photography.

REFERENCES

1. Reynolds, O., "The Causes of the Racing of Screw Steamers, Investigated Theoretically and by Experiment," Transactions of the Institute of Naval Architects, Scientific Papers I, 1873, pp. 51-58.
2. Reynolds, O., "On the Effect of Immersion on Screw Propellers," Transactions of the Institute of Naval Architects, Scientific Papers I, 1874, pp. 78-80.
3. Wislicenus, G. F., "Remarks on the History of Cavitation as an Engineering Problem," Proceedings of Symposium on Cavitation State of Knowledge, ASME, 1909, pp. 10-14.
4. Holl, J. W., and Treaster, A. L., "Cavitation Hysteresis," Journal of Basic Engineering, Transactions ASME, Series D, Vol. 88, No. 1, March 1966, pp. 199-212.
5. Reed, R. L., "The Influence of Surface Characteristics and Pressure History on the Inception of Cavitation," M.S. Dissertation, Department of Aerospace Engineering, The Pennsylvania State University, March 1969.
6. Holl, J. W. and Wislicenus, G. F., "Scale Effects on Cavitation," Journal of Basic Engineering, Transactions ASME, September 1961, pp. 385-398.
7. Holl, J. W., "Limited Cavitation," Proceedings of Symposium on Cavitation State of Knowledge, ASME, 1969, pp. 26-63.
8. Kermeen, R. W., "Some Observations of Cavitation on Hemispherical Head Models," Hydrodynamics Laboratory, California Institute of Technology, Report E-35.1, June 1952.
9. Parkin, B. R. and Holl, J. W., "Incipient-Cavitation Scaling Experiments for Hemispherical and 1.5-Caliber Ogive-Nosed Bodies," A Joint Study by Hydrodynamics Laboratory, California Institute of Technology and Ordnance Research Laboratory, The Pennsylvania State University, Ser NOrd 7958.264, 15 May 1953.
10. Parkin, B. R. and Kermeen, R. W., "Incipient Cavitation and Boundary-Layer Interaction on a Streamlined Body," Hydrodynamics Laboratory, California Institute of Technology, Report E-35.2, December 1953.
11. Rouse, H. and McNown, J. S., "Cavitation and Pressure Distribution-Headforms at Zero Angle of Yaw," Iowa Institute of Hydraulic Research, State University of Iowa, 1948.

12. Lindgren, H. and Johnsson, C. A., "Cavitation Inception on Headforms—ITTC Comparative Experiments," Publications of the Swedish State Shipbuilding Experimental Tank, No. 58, 1966.
13. Gates, E. M., "The Influence of Freestream Turbulence, Freestream Nuclei Populations, and a Drag-Reducing Polymer on Cavitation Inception on Two Axisymmetric Bodies," Ph.D. Thesis, California Institute of Technology, April 1977.
14. Arakeri, V. H., "Viscous Effects in Inception and Development of Cavitation on Axi-Symmetric Bodies," Ph.D. Thesis, California Institute of Technology, 1973.
15. Arakeri, V. H. and Acosta, A. J., "Viscous Effects in the Inception of Cavitation on Axisymmetric Bodies," Journal of Fluids Engineering, Transactions ASME, Vol. 95, Series 1, No. 4, December 1973, pp. 519-528.
16. Arakeri, V. H. and Acosta, A. J., "Cavitation Inception Observations on Axisymmetric Bodies at Supercritical Reynolds Numbers," Journal of Ship Research, SNAME, Vol. 20, No. 1, March 1976, pp. 40-50.
17. Van der Meulen, J. H. J., "A Holographic Study of Cavitation on Axisymmetric Bodies and the Influence of Polymer Additives," Publication No. 509, Netherlands Ship Model Basin, Wageningen, The Netherlands, 1976.
18. Silberman, E. and Schiebe, F., "A Method for Determining the Relative Cavitation Susceptibility of Water," Presented at Conference on Cavitation, Institute of Mechanical Engineers, Edinburgh, Scotland, 1976.
19. Lehman, A. F., "The Garfield Thomas Water Tunnel," ORL Report No. NOrd 16597-56, The Pennsylvania State University, 1959.
20. Schiebe, F. R., "The Influence of Gas Nuclei Size Distribution on Transient Cavitation Near Inception," University of Minnesota, St. Anthony Falls Hydraulic Laboratory, Project Report No. 107, May 1969.
21. Brockett, T. E., "Some Environmental Effects on Headform Cavitation Inception," David Taylor Naval Ship Research and Development Center, Report No. 3974, October 1972.
22. Holl, J. W., "Nuclei and Cavitation," Journal of Basic Engineering, Transactions ASME, Vol. 92, December 1970, pp. 681-688.
23. Holl, J. W. and Kornhauser, A. L., "Thermodynamic Effects on Desinent Cavitation on Hemispherical Nosed Bodies in Water at Temperatures from 80°F to 260°F," Journal of Basic Engineering, Transactions ASME, Vol. 92, March 1970, pp. 44-58.

24. Hsieh, D. Y., "Some Analytical Aspects of Bubble Dynamics," Journal of Basic Engineering, Transactions ASME, Series D, Vol. 87, No. 4, December 1965, pp. 991-1005.
25. Gaster, M., "The Structure and Behavior of Laminar Separation Bubbles from Separated Flows, Part 2," AGARD-NATO Conference Proceedings, No. 4, May 1966, pp. 813-854.
26. Arakeri, V. H., "A Note on the Transition Observations on an Axisymmetric Body and Some Related Fluctuating Wall Pressure Measurements," Journal of Fluids Engineering, Transactions ASME, Vol. 97, Series 1, No. 1, March 1975, pp. 82-86.
27. Huang, T. T. and Hannan, D. E., "Pressure Fluctuations in the Regions of Flow Transition," David Taylor Naval Ship Research and Development Center, Report 4723, December 1975.
28. Acosta, A. J. and Hamaguchi, H., "Cavitation Inception on the ITTC Standard Headform," Hydrodynamics Laboratory, California Institute of Technology, Report E-149.1, March 1967.
29. Keller, A., "Experimentelle und Theoretische Untersuchungen zum Problem der Modellmaessigen Behandlung von Stroemungskavitation," Ph.D. Dissertation, Technical University of Munich, West Germany, February 1973.
30. Bohn, J. C., "The Influence of Surface Irregularities on Cavitation: A Collation and Analysis of New and Existing Data with Application to Design Problems," M.S. Thesis, Department of Aerospace Engineering, The Pennsylvania State University, December 1972.
31. Holl, J. W., "The Effect of Surface Irregularities on Incipient Cavitation," Ph.D. Thesis, The Pennsylvania State University, June 1958.
32. Arndt, R. E. A., Holl, J. W., Bohn, J. C., and Bechtel, W. T., "The Influence of Surface Irregularities on Cavitation Performance," Accepted for Publication, Journal of Ship Research, SNAME.
33. Jaffe, N. A., Okamura, T. T., and Smith, A. M. O., "Determination of Spatial Amplification Factors and Their Application to Predicting Transition," AIAA Journal, Vol. 8, No. 2, February 1970, pp. 301-308.
34. Arakeri, V. H., Carroll, J. A., and Holl, J. W., "A Note on the Effect of Short and Long Laminar Separation Bubbles on Desinent Cavitation," Proceedings of the Symposium on Measurements in Polyphase Flows, ASME, December 1978, pp. 115-120.

APPENDIX A
DISCUSSION OF EXPERIMENTAL ERROR IN MEASUREMENTS

Velocity Measurements

The combination of Bernoulli's equation and the one-dimensional momentum equation for incompressible flow through a pipe of varying diameter yields the following:

$$P_0 - P_\infty = \frac{1}{2} \rho U_\infty^2 \left[1 - \left(\frac{A_\infty}{A_0} \right)^2 \right] , \quad (29)$$

where

P = pressure,

ρ = fluid density,

U = fluid velocity, and

A = cross-sectional area.

By letting the subscripts 0 and ∞ correspond to the tunnel plenum and test section, respectively, we obtain the equation for the free stream velocity in the test section:

$$U_\infty = \left[\frac{2}{\rho} (P_0 - P_\infty) / \left(1 - \left(\frac{A_\infty}{A_0} \right)^2 \right) \right]^{1/2} . \quad (30)$$

The pressure drop through the contraction ($P_0 - P_\infty$) is measured and given as ΔP . The contraction ratio (A_∞/A_0) equals $1/9$. Substitution yields

$$U_\infty = \left(\frac{81}{40} \frac{\Delta P}{\rho} \right)^{1/2} . \quad (31)$$

Taking the first derivative of Equation (31) gives

$$d(U_{\infty}) = \frac{1}{2} \left(\frac{81}{40} \frac{1}{\rho} \right) \left(\frac{81}{40} \frac{\Delta P}{\rho} \right)^{-\frac{1}{2}} d(\Delta P) , \quad (32)$$

which may be rewritten as

$$d(U_{\infty}) = \frac{81}{80} \frac{1}{\rho} \frac{1}{U_{\infty}} d(\Delta P) . \quad (33)$$

The error in U_{∞} can, therefore, be calculated by the following equation:

$$\% \text{ Error in } U_{\infty} = \frac{d(U_{\infty})}{U_{\infty}} \times 100\% = \frac{81}{80} \frac{1}{\rho} \frac{1}{U_{\infty}^2} d(\Delta P) \times 100\% , \quad (34)$$

where $d(\Delta P)$ is the transducer accuracy as specified by the manufacturer (± 0.06 psi). Equation (34) suggests that the error in measured U_{∞} varies from about ± 0.1 percent to ± 0.5 percent for the velocity range of 70.0 to 30.0 fps.

Pressure Coefficients

The experimental pressure coefficients measured over the hemispherical nose were calculated as follows:

$$C_P = \frac{P_n - P_{\infty}}{P_1 - P_{\infty}} , \quad (35)$$

where

P_1 = stagnation pressure on the nose,

P_{∞} = static pressure in the test section, and

P_n = pressure measured by the n^{th} pressure tap on the nose.

The pressures were all measured with a single differential pressure transducer. We can, therefore, write Equation (35) as

$$C_p = \frac{\Delta P_n \pm \epsilon}{\Delta P_1 \pm \epsilon} , \quad (36)$$

where

ϵ = the inherent transducer error,

$\Delta P_1 = P_1 - P_\infty$, and

$\Delta P_n = P_n - P_\infty$.

The maximum error in C_p measurements can, therefore, be written as

$$\text{Error in } C_p = \left[\frac{\Delta P_n}{\Delta P_1} \left(\frac{1 + \frac{\epsilon}{\Delta P_n}}{1 - \frac{\epsilon}{\Delta P_1}} \right) - \frac{\Delta P_n}{\Delta P_1} \right] \left(\frac{\Delta P_1}{\Delta P_n} \right) . \quad (37)$$

Letting $\epsilon/\Delta P_n = v_n$ and $\epsilon/\Delta P_1 = v_1$, Equation (37) becomes

$$\text{Error in } C_p = \frac{1 + v_n}{1 - v_1} - 1 \quad (38a)$$

$$= \frac{v_n + v_1}{1 - v_1} \quad (38b)$$

$$= \left(\frac{v_n}{v_1} + 1 \right) / \left(\frac{1}{v_1} - 1 \right) \quad (38c)$$

$$= \left(\frac{v_n}{v_1} \right) / \left(\frac{1}{v_1} - 1 \right) + 1 / \left(\frac{1}{v_1} - 1 \right) \quad (38d)$$

Now,

$$1 / \left(\frac{1}{v_1} - 1 \right) = v_1 + v_1^2 + v_1^3 + v_1^4 + \dots . \quad (39)$$

Equation (38d) can, therefore, be written as

$$\text{Error in } C_p = \frac{v_n}{v_1} \left(v_1 + v_1^2 + v_1^3 + v_1^4 + \dots \right) + v_1 + v_1^2 + v_1^3 + v_1^4 + \dots , \quad (40)$$

which may be written as

$$\begin{aligned} \text{Error in } C_p = & v_n + v_1(v_n + 1) + v_1^2(v_n + 1) + v_1^3(v_n + 1) + v_1^4(v_n + 1) + \\ & + \dots . \end{aligned} \quad (41)$$

Substituting the values for v_n and v_i yields

$$\begin{aligned} \text{Error in } C_p = & \frac{\epsilon}{\Delta P_n} + \frac{\epsilon}{\Delta P_1} \left(\frac{\epsilon}{\Delta P_n} + 1 \right) + \left(\frac{\epsilon}{\Delta P_1} \right)^2 \left(\frac{\epsilon}{\Delta P_n} + 1 \right) \\ & + \left(\frac{\epsilon}{\Delta P_1} \right)^3 \left(\frac{\epsilon}{\Delta P_n} + 1 \right) + \dots , \end{aligned} \quad (42)$$

which for small values of $\epsilon/\Delta P_n$ and $\epsilon/\Delta P_1$, may be written as

$$\% \text{ Error in } C_p \doteq \epsilon \left(\frac{1}{\Delta P_n} + \frac{1}{\Delta P_1} \right) \times 100\% . \quad (43)$$

From Equation (43), it is apparent that the maximum error in C_p will occur for minimum values of ΔP_1 and ΔP_n , which correspond to minimum values of U_∞ and $|C_p|$, respectively. The transducer error is given as

$$\epsilon = \pm 0.025 \text{ psi} . \quad (44)$$

Approximate experimental error in the C_p data may be calculated from Equation (43). For a typical value of $|C_p|$ of 0.06, the resulting

error ranges from about 1.1 percent for a velocity of 30.0 fps to 0.21 percent for a velocity of 70.0 fps.

Cavitation Number

The cavitation number is calculated in the present investigation using the following equation:

$$\sigma = \frac{P_{atm} - P_v + \Delta P_\infty}{K\Delta P} , \quad (45)$$

where

P_{atm} = atmospheric pressure,

P_v = vapor pressure of water,

P_∞ = free stream static pressure,

ΔP_∞ = $P_\infty - P_{atm}$, and

K = constant,

The deviation in σ may be written as

$$d\sigma = \frac{\partial(\sigma)}{\partial(P_{atm})} d(P_{atm}) + \frac{\partial(\sigma)}{\partial(\Delta P_\infty)} d(\Delta P_\infty) + \frac{\partial(\sigma)}{\partial(\Delta P)} d(\Delta P) \quad (46)$$

for small deviations of P_{atm} , ΔP_∞ , and ΔP . The partial derivatives in Equation (46) are as follows:

$$\frac{\partial(\sigma)}{\partial(P_{atm})} = \frac{1}{K\Delta P} , \quad (47)$$

$$\frac{\partial(\sigma)}{\partial(\Delta P_\infty)} = \frac{1}{K\Delta P} , \quad (48)$$

and

$$\frac{\partial(\sigma)}{\partial(\Delta P)} = - \frac{(P_{atm} + \Delta P_\infty - P_v)}{\Delta P} = - \frac{\sigma}{\Delta P} . \quad (49)$$

The differentials $d(P_{atm})$, $d(\Delta P_\infty)$, and $d(\Delta P)$ correspond to the error involved in measuring P_{atm} , ΔP_∞ , and ΔP , respectively. The error in measurement of σ may, therefore, be approximated by

$$\text{Error in } \sigma = \frac{d\sigma}{\sigma} = \frac{1}{\sigma} \left[\left(\frac{1}{K\Delta P} \right) d(P_{atm}) + \left(\frac{1}{K\Delta P} \right) d(\Delta P_\infty) - \left(\frac{\sigma}{\Delta P} \right) d(\Delta P) \right] . \quad (50)$$

Equation (50) may be rewritten as

$$\text{Error in } \sigma = \frac{1}{\Delta P} \left[\frac{1}{K\sigma} \left(d(P_{atm}) + d(\Delta P_\infty) \right) - d(\Delta P) \right] . \quad (51)$$

The values of $d(P_{atm})$, $d(\Delta P_\infty)$, and $d(\Delta P)$ are approximately ± 0.025 psi, ± 0.03 psi, and ± 0.06 psi, respectively. The value of K is about one. The maximum error can be estimated from the resulting equation:

$$\% \text{ Error in } \sigma = \frac{1}{\Delta P} \left(\frac{0.055}{\sigma} + 0.06 \right) \times 100\% , \quad (52)$$

or in terms of U [see Equation (31)],

$$\% \text{ Error in } \sigma = \frac{1}{U_\infty^2} \left(\frac{8.3}{\sigma} + 9.02 \right) \times 100\% . \quad (53)$$

From the above analysis, the maximum error in σ is approximately 5.0 percent.

Another source of error in the measured values of σ should be mentioned. The calling of limited cavitation conditions was based on observation. The error due to human judgment may be quite significant, particularly for transient forms of cavitation. The resulting scatter in σ is estimated to be as much as ± 0.1 .

APPENDIX B

CALIBRATION PROCEDURE FOR A CAVITY-MOUNTED DYNAMIC
PRESSURE TRANSDUCER

An undesirable cavity resonance was discovered during preliminary turbulent pressure measurements made with a cavity-mounted pressure transducer as discussed in Chapter VII. A cavity resonance occurred with a frequency of 5.0 kHz and was much lower than the calculated resonance frequency of 13.1 kHz. It seems likely that the wrong effective cavity volume was used for the calibration [Equation (26)]. The transducer is waterproofed with an elastic material which occupies a small region over the sensing element. The region apparently should have been included as part of the cavity volume in performing the calculations. Nevertheless, the test program was carried out and all of the test results showed evidence of the cavity resonance. A frequency calibration which was performed later was used to correct the test data.

The calibration procedure is based on the substitution principle of known and unknown receivers. First, the unknown receiver, the cavity-mounted transducer, is placed in a fluctuating pressure field and the resulting signal spectrum is recorded. Next, the known receiver, in this case, the same transducer without a cavity, is substituted for the unknown receiver in the same fluctuating pressure field. The resulting signal is also recorded. The spectrum from the unknown receiver is then multiplied by the inverse of the spectrum from the known receiver. The resulting curve shows the spectral energy

associated with the cavity resonance and is used to correct the test data.

Two different transducer mounting arrangements were used for the unknown and the known cases. For the unknown case, the transducer was mounted in a housing containing the cavity and duct. The housing is the same one used for the actual test measurements. The housing was anchored in an assembly which duplicated the mounting configuration of the test model except for the flow surface which, in this case, was flat. The assembly for the known case simply anchored the transducer so that its sensing element was flush with the outer surface. Sketches of the known and unknown calibration assemblies are shown in Figure 66. The overall shape and dimensions of the two calibration assemblies were the same, so that substitution of one for the other was done easily. The fluctuating pressure field was produced by a turbulent water jet in air. First, the cavity-mounted configuration was positioned so that the jet impinged directly on the tiny orifice leading to the transducer cavity. A signal spectrum was recorded over the same frequency range as the test data. The plot of the energy spectrum of the unknown [$\phi(f)_{\text{unknown}}$] is presented in Figure 67. The familiar resonance spike can be seen in this spectrum. The "unknown" assembly was then removed and the flush-mounted "known" configuration was placed in exactly the same position relative to the jet. The spectrum of this signal was also recorded and is presented as $\phi(f)_{\text{known}}$ also in Figure 67. The actual frequency content of the turbulent jet is not of real importance because both known and unknown receivers measure

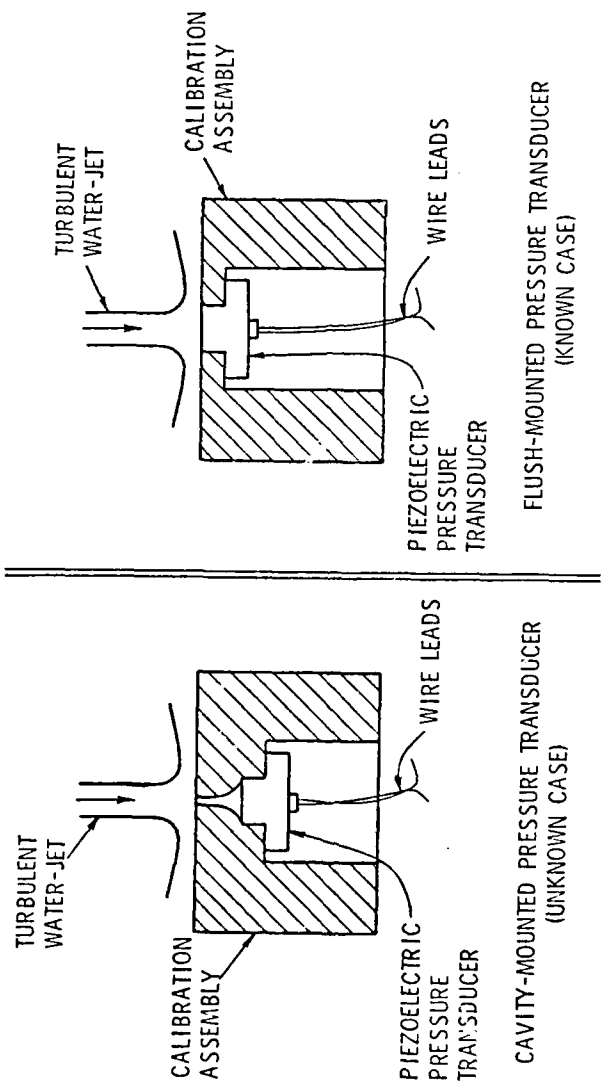


Figure 66. Sketch illustrating two types of pressure transducer mounting configurations used for calibration purposes.

AD-A104 779

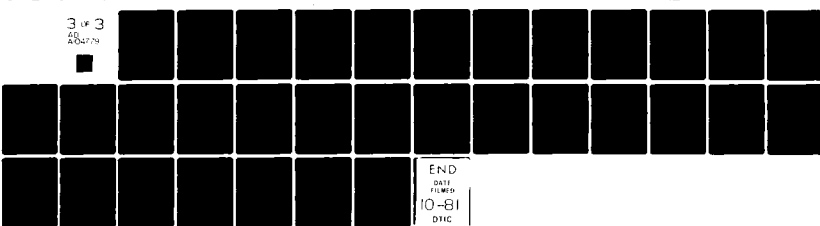
PENNSYLVANIA STATE UNIV UNIVERSITY PARK APPLIED RESE--ETC F/G 20/4
OBSERVATIONS OF THE EFFECTS OF BOUNDARY LAYER AND NUCLEI ON CAV--ETC(U)
FEB 81 J A CARROLL
ARL/PSU/TM-81-60

N00024-79-C-6043

NL

UNCLASSIFIED

3 w 3
60
A04779



END
DATE
FILED
10-81
DTIC

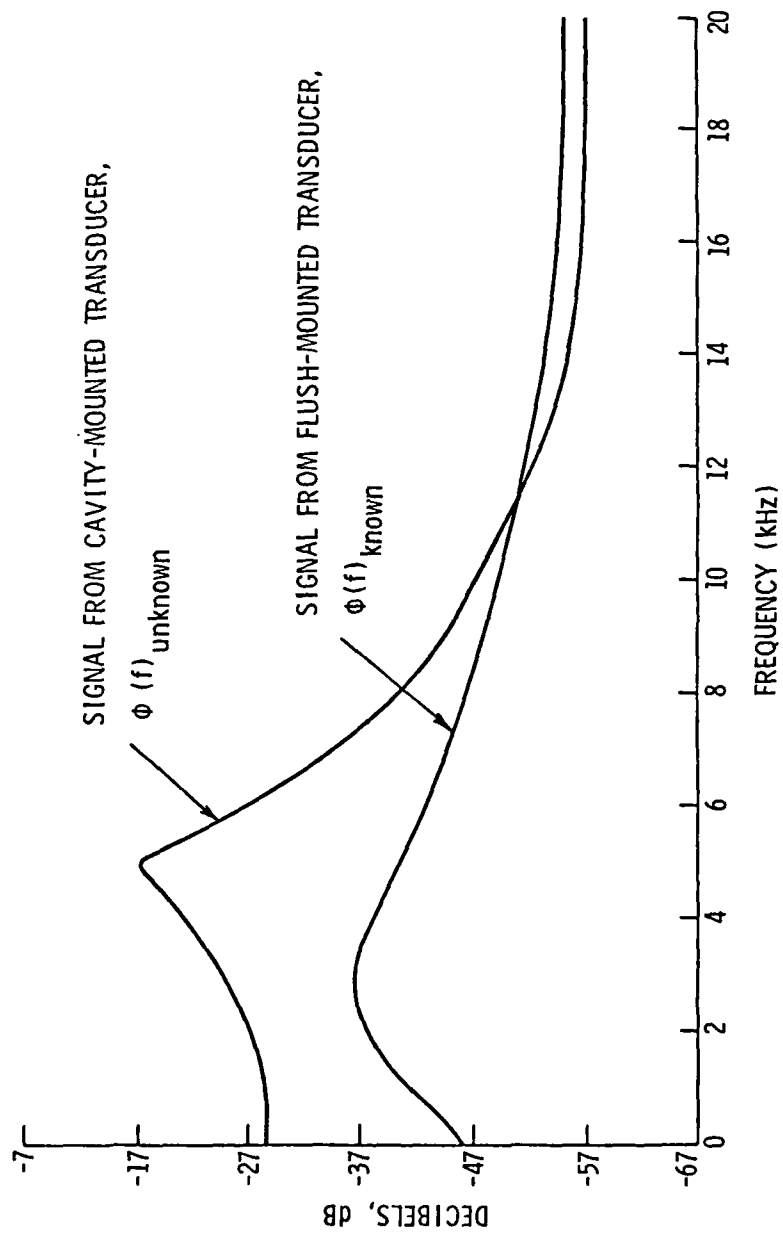


Figure 67. Comparison of energy spectra for cavity-mounted and flush-mounted pressure transducer configurations.

the same signal. The turbulent source should, however, meet the following requirements:

1. The highest frequency of the calibration signal should be at least as high as the highest frequency that occurs in the test data.
2. The dimension of the signal source (i.e., jet cross-section) should be at least as large as the transducer sensing area.

The correlation factor [$\phi_1(f)$] is obtained from the following equation:

$$\phi_1(f) = \phi(f)_{\text{known}} - \phi(f)_{\text{unknown}} . \quad (54)$$

A graph of $\phi_1(f)$ is presented in Figure 68. The effect of the cavity resonance present in the test data is eliminated by applying the correction factor [$\phi_1(f)$]. Further details of the data reduction process are given in Appendix C.

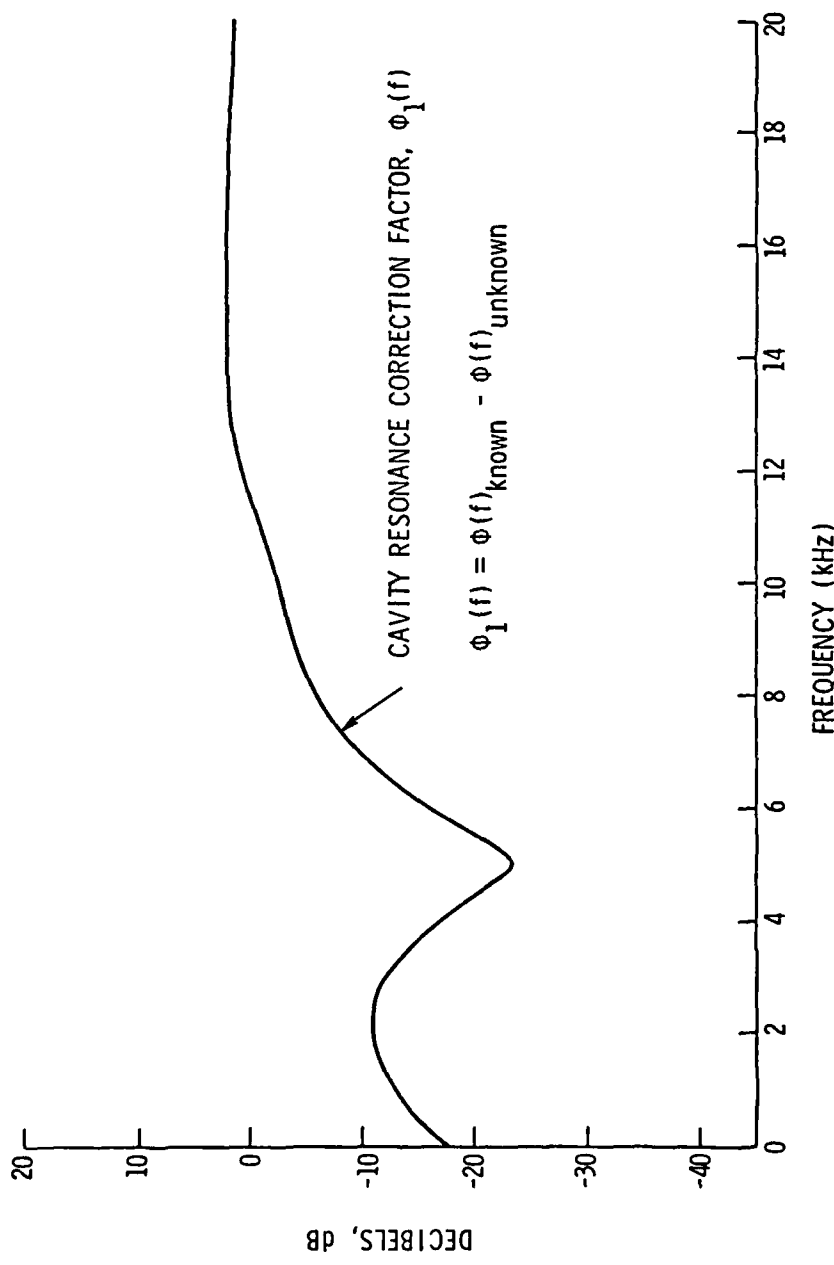


Figure 68. Plot of calibration results which was used to correct for the effect of cavity resonance.

APPENDIX C
PROCEDURE FOR REDUCTION OF FLUCTUATING PRESSURE DATA

Measured fluctuating pressure data were recorded as spectral plots of dB_V versus frequency. In order to obtain absolute pressure information from these plots, several corrections had to be applied. These corrections are as follows:

$$\Phi(f) = \phi_0(f) + \phi_1(f) + \phi_2(f) + \phi_3 \quad (55)$$

and

$$P'_{\text{rms MAX}}(f) = \frac{1}{20} \log^{-1} [\Phi(f)] , \quad (56)$$

where

$\Phi(f)$ = rms pressure (in dB_V),

$\phi_0(f)$ = original test data,

$\phi_1(f)$ = correction for cavity resonance,

$\phi_2(f)$ = attenuation due to frequency response of charge amplifier,

ϕ_3 = constant (transducer sensitivity), and

$P'_{\text{rms MAX}}(f)$ = rms pressure (60.0 Hz bandwidth).

The correction factor [$\phi_1(f)$] in Equation (55) is needed to correct for the effect of the cavity resonance. The procedure for obtaining $\phi_1(f)$ is discussed in Appendix B.

The signal attenuation due to the frequency response of the charge amplifier is represented by $\phi_2(f)$. This information was obtained by introducing a sinusoidal signal of known frequency in the transducer circuit and comparing the analyzer output with the known input for

several input frequencies. A plot of the resulting attenuation curve [$\phi_2(f)$] is presented in Figure 69.

The final term ϕ_3 in Equation (55) corrects for the transducer sensitivity, m . Its value is assumed constant over the frequency range of interest (0.5 to 20.0 kHz). The manufacturer's value for the sensitivity is given as 0.23 volts per psi for an average pressure signal of 125.0 psia. Because the dynamic pressures measured in the present investigation are of the order of one psia, it seemed advisable to check the sensitivity for a correspondingly lower signal amplitude. A pistophone, normally used for calibrating microphones, was used for this purpose. The output of the pistophone is 124.0 dB re 2×10^{-5} Pa (0.005 psia) with a frequency of 250.0 Hz. The output of the transducer was measured directly with an oscilloscope. The sensitivity, m , was found to be 0.13 volts per psi. Interpolation to a one psi signal gave essentially the same result. Therefore, this value of sensitivity was used in the data reduction. The correction, ϕ_3 , is related to the sensitivity, m , by the following relationship:

$$\phi_3 = 20 \log_{10}(m) . \quad (57)$$

The test data [$\phi_0(f)$], originally recorded in dB_V versus frequency, were corrected point by point according to Equation (55). Equation (56) was then used to obtain absolute pressure levels. The data correction procedure is illustrated in Figure 70. Original data are shown as $\phi_0(f)$ for an arbitrary test condition. The corrected curve is labeled $\phi(f)$.

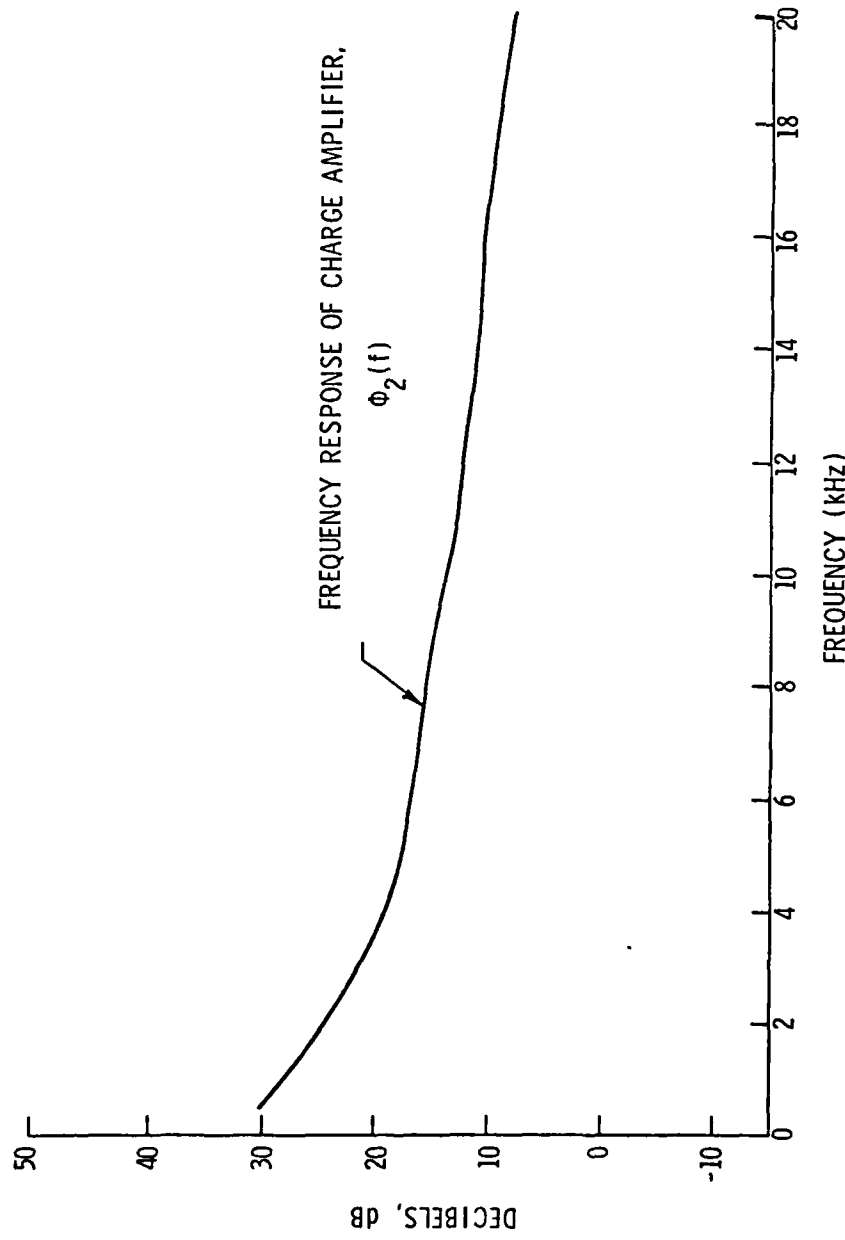


Figure 69. Plot of signal attenuation due to the frequency response characteristics of charge amplifier used in fluctuating pressure measurements.

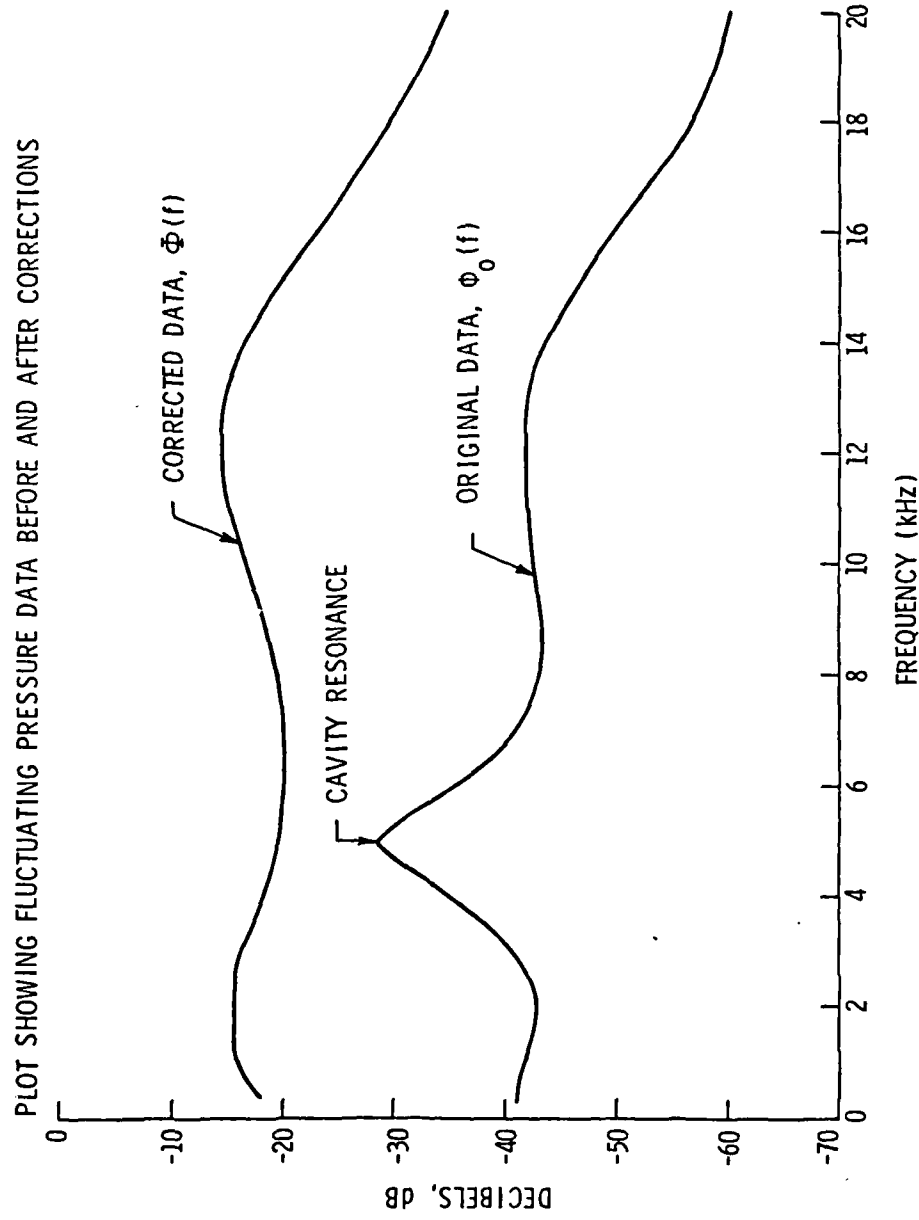


Figure 70. Plot showing typical measured energy spectrum before and after corrections for cavity resonance, frequency response, and gain.

APPENDIX D
DATA TABULATIONS

Tables

1. Theoretical Pressure Distributions	
a) Hemispherical Nose	4
b) Schiebe Nose	5
c) DTNSRDC Nose	6
2. Measured Pressure Distributions - Hemispherical Nose	7 - 14
3. Limited Cavitation Data	
a) Hemispherical Nose	15 - 16
b) Schiebe Nose	17 - 18
c) DTNSRDC Nose	19 - 20

Table 4. Douglas Neumann Pressure Distribution

Model: Hemispherical Nose

 $C_p(U-B)$ - Unblocked case $C_p(B)$ - With blockage (2.0-in. diameter model in 12.0-in. diameter tunnel)

$\frac{S}{D}$	$C_p(U-B)$	$C_p(B)$	$\frac{S}{D}$	$C_p(U-B)$	$C_p(B)$
0.00000	0.99997	0.99997	0.12058	0.87653	0.87338
0.00180	0.99993	0.99993	0.12588	0.86611	0.86269
0.00270	0.99984	0.99983	0.13130	0.85417	0.85044
0.00372	0.99979	0.99979	0.13683	0.84239	0.83836
0.00485	0.99965	0.99964	0.14247	0.82965	0.82529
0.00609	0.99952	0.99951	0.14822	0.81646	0.81176
0.00744	0.99933	0.99931	0.15409	0.80193	0.79686
0.00891	0.99913	0.99910	0.16007	0.78733	0.78187
0.01049	0.99876	0.99873	0.16616	0.77166	0.76580
0.01218	0.99851	0.99847	0.17237	0.75492	0.74863
0.01398	0.99791	0.99785	0.17868	0.73756	0.73081
0.01590	0.99751	0.99745	0.18511	0.72001	0.71280
0.01793	0.99678	0.99670	0.19165	0.70053	0.69281
0.02007	0.99607	0.99597	0.19831	0.68086	0.67262
0.02233	0.99525	0.99513	0.20508	0.66047	0.65170
0.02470	0.99417	0.99402	0.21196	0.63877	0.62943
0.02718	0.99313	0.99296	0.21896	0.61698	0.60706
0.02978	0.99174	0.99153	0.22606	0.59335	0.58280
0.03248	0.99032	0.99008	0.23328	0.56974	0.55856
0.03530	0.98856	0.98827	0.24061	0.54450	0.53264
0.03823	0.98674	0.98640	0.24806	0.51838	0.50582
0.04128	0.98456	0.98417	0.25562	0.49182	0.47855
0.04444	0.98220	0.98175	0.26329	0.46446	0.45045
0.04771	0.97970	0.97919	0.27107	0.43631	0.42154
0.05110	0.97659	0.97599	0.27897	0.40631	0.39072
0.05459	0.97365	0.97298	0.28698	0.37670	0.36030
0.05820	0.97002	0.96926	0.29510	0.34613	0.32889
0.06192	0.96611	0.96525	0.30334	0.31440	0.29629
0.06576	0.96205	0.96109	0.31168	0.28166	0.26264
0.06971	0.95753	0.95645	0.32015	0.24870	0.22876
0.07377	0.95226	0.95105	0.32872	0.21530	0.19443
0.07794	0.94734	0.94600	0.33741	0.18047	0.15862
0.08223	0.94107	0.93957	0.34620	0.14557	0.12273
0.08663	0.93512	0.93347	0.35511	0.10971	0.08585
0.09114	0.92826	0.92643	0.36414	0.07391	0.04902
0.09576	0.92095	0.91894	0.37328	0.03678	0.01082
0.10050	0.91334	0.91114	0.38253	-0.00032	-0.02735
0.10535	0.90492	0.90249	0.39189	-0.03728	-0.06540
0.11032	0.89610	0.89345	0.40137	-0.07445	-0.10366
0.11539	0.88646	0.88357	0.41096	-0.11277	-0.14312

Table 4 (Continued). Douglas Neumann Pressure Distribution

Model: Hemispherical Nose

$\frac{S}{D}$	$C_p(U-B)$	$C_p(B)$	$\frac{S}{D}$	$C_p(U-B)$	$C_p(B)$
0.42065	-0.15072	-0.18221	2.17840	-0.02795	-0.07081
0.43047	-0.18842	-0.22104	2.32936	-0.02440	-0.06804
0.44039	-0.22623	-0.26001	2.48033	-0.02151	-0.06591
0.45043	-0.26427	-0.29921	2.63129	-0.01913	-0.06425
0.46059	-0.30103	-0.33711	2.78226	-0.01713	-0.06295
0.47085	-0.33892	-0.37618	2.93323	-0.01545	-0.06192
0.48124	-0.37483	-0.41324	3.08419	-0.01401	-0.06111
0.49173	-0.41080	-0.45035	3.23516	-0.01278	-0.06046
0.50233	-0.44645	-0.48716	3.38613	-0.01171	-0.05995
0.51305	-0.48143	-0.52329	3.53709	-0.01078	-0.05953
0.52388	-0.51364	-0.55657	3.68806	-0.00996	-0.05920
0.53482	-0.54578	-0.58980	3.83902	-0.00924	-0.05894
0.54588	-0.57683	-0.62192	3.98999	-0.00860	-0.05872
0.55704	-0.60565	-0.65175	4.14096	-0.00803	-0.05855
0.56832	-0.63430	-0.68143	4.29192	-0.00752	-0.05841
0.57972	-0.66008	-0.70815	4.44289	-0.00707	-0.05830
0.59122	-0.68383	-0.73279	4.59385	-0.00666	-0.05821
0.60284	-0.70453	-0.75431	4.74482	-0.00629	-0.05814
0.61457	-0.72476	-0.77536	4.89579	-0.00596	-0.05808
0.62641	-0.74119	-0.79250	5.04675	-0.00566	-0.05803
0.63837	-0.75386	-0.80576	5.19772	-0.00538	-0.05799
0.65045	-0.76438	-0.81683	5.34868	-0.00513	-0.05796
0.66263	-0.77174	-0.82465	5.49965	-0.00490	-0.05793
0.67492	-0.77490	-0.82814	5.65061	-0.00469	-0.05791
0.68733	-0.77295	-0.82638	5.80158	-0.00450	-0.05790
0.69986	-0.76767	-0.82119	5.95254	-0.00433	-0.05788
0.71249	-0.75749	-0.81095	6.10351	-0.00417	-0.05787
0.72524	-0.74027	-0.79344	6.25448	-0.00402	-0.05786
0.73810	-0.71633	-0.76901	6.40544	-0.00388	-0.05785
0.75107	-0.68378	-0.73569	6.55641	-0.00376	-0.05785
0.76416	-0.63933	-0.69010	6.70737	-0.00365	-0.05784
0.77735	-0.56851	-0.61730	6.85834	-0.00354	-0.05783
0.79392	-0.46877	-0.51470	7.00930	-0.00345	-0.05783
0.81877	-0.37320	-0.41648	7.16027	-0.00336	-0.05783
0.85604	-0.29922	-0.34062	7.31124	-0.00328	-0.05782
0.91196	-0.23259	-0.27248	7.46220	-0.00320	-0.05782
0.99583	-0.17370	-0.21254	7.61317	-0.00314	-0.05782
1.12163	-0.12378	-0.16215	7.78632	-0.00307	-0.05782
1.27260	-0.09007	-0.12861	8.03399	-0.00298	-0.05782
1.42356	-0.06931	-0.10836	8.40898	-0.00288	-0.05782
1.57453	-0.05535	-0.09507	8.95899	-0.00278	-0.05781
1.72550	-0.04540	-0.08588	9.78399	-0.00273	-0.05781
1.87646	-0.03803	-0.07929	11.03399	-0.00291	-0.05782
2.02743	-0.03238	-0.07444	12.90899	-0.00293	-0.05687

Table 5. Douglas Neumann Pressure Distribution

Model: Schiebe Nose

- $C_p(U-B)$ - Unblocked case
 $C_p(B)$ - With blockage (2.0-in. diameter model in 12.0-in. diameter tunnel)

$\frac{S}{D}$	$C_p(U-B)$	$C_p(B)$	$\frac{S}{D}$	$C_p(U-B)$	$C_p(B)$
0.00000	0.99822	0.99818	0.71442	-0.28579	-0.32423
0.03484	0.98817	0.98787	0.72604	-0.27997	-0.31838
0.05808	0.97618	0.97559	0.73766	-0.27454	-0.31291
0.08132	0.95957	0.95857	0.74927	-0.26806	-0.30637
0.10456	0.93722	0.93566	0.76088	-0.26251	-0.30079
0.12779	0.90804	0.90575	0.77250	-0.25708	-0.29532
0.15102	0.86947	0.86622	0.78412	-0.25123	-0.28942
0.17426	0.81823	0.81368	0.79573	-0.24581	-0.28397
0.19750	0.74912	0.74281	0.80735	-0.23993	-0.27803
0.22073	0.65238	0.64360	0.81896	-0.23394	-0.27200
0.24397	0.51249	0.50013	0.83058	-0.22804	-0.26603
0.26722	0.28868	0.27052	0.84220	-0.22251	-0.26045
0.29046	-0.06475	-0.09211	0.85381	-0.21622	-0.25410
0.31367	-0.50743	-0.54652	0.86543	-0.21019	-0.24800
0.33430	-0.73766	-0.78309	0.87704	-0.20554	-0.24332
0.35173	-0.75676	-0.80303	0.88866	-0.20026	-0.23800
0.37173	-0.70559	-0.75088	0.90028	-0.19486	-0.23255
0.39495	-0.66539	-0.71003	0.91189	-0.19058	-0.22825
0.41818	-0.61763	-0.66139	0.92351	-0.18664	-0.22430
0.44142	-0.56463	-0.60733	0.93512	-0.18302	-0.22069
0.46465	-0.52988	-0.57198	0.94674	-0.17957	-0.21724
0.48789	-0.50161	-0.54329	0.95835	-0.17629	-0.21397
0.51113	-0.47131	-0.51249	0.96997	-0.17317	-0.21087
0.52856	-0.44800	-0.48877	0.98159	-0.17036	-0.20809
0.54017	-0.43219	-0.47268	0.99320	-0.16681	-0.20454
0.55179	-0.41872	-0.45899	1.00481	-0.16322	-0.20094
0.56340	-0.40784	-0.44796	1.01643	-0.16008	-0.19781
0.57502	-0.39721	-0.43718	1.02805	-0.15739	-0.19515
0.58664	-0.38757	-0.42742	1.03966	-0.15395	-0.19171
0.59825	-0.37799	-0.41772	1.05128	-0.15046	-0.18822
0.60987	-0.36841	-0.40801	1.06289	-0.14741	-0.18518
0.62148	-0.35774	-0.39718	1.07451	-0.14447	-0.18225
0.63310	-0.34768	-0.38697	1.08613	-0.14154	-0.17933
0.64472	-0.33834	-0.37750	1.09774	-0.13801	-0.17579
0.65633	-0.32878	-0.36780	1.10936	-0.13571	-0.17353
0.66795	-0.31928	-0.35818	1.12097	-0.13346	-0.17131
0.67957	-0.30931	-0.34805	1.13259	-0.13021	-0.16805
0.69119	-0.30142	-0.34006	1.14420	-0.12761	-0.16547
0.70280	-0.29380	-0.33235	1.16163	-0.12465	-0.16257

Table 5 (Continued). Douglas Neumann Pressure Distribution

Model: Schiebe Nose

$\frac{S}{D}$	$C_p(U-B)$	$C_p(B)$	$\frac{S}{D}$	$C_p(U-B)$	$C_p(B)$
1.18486	-0.11956	-0.15752	3.56933	-0.01276	-0.06134
1.20809	-0.11487	-0.15289	3.63433	-0.01168	-0.06045
1.23132	-0.11075	-0.14883	3.69933	-0.01057	-0.05951
1.25455	-0.10666	-0.14480	3.76433	-0.00959	-0.05871
1.27778	-0.10262	-0.14082	3.82932	-0.00872	-0.05803
1.30812	-0.09783	-0.13613	3.89433	-0.00799	-0.05748
1.35935	-0.09058	-0.12906	3.95933	-0.00761	-0.05728
1.42435	-0.08251	-0.12125	4.02433	-0.00792	-0.05781
1.48934	-0.07546	-0.11447	4.08932	-0.00864	-0.05897
1.55434	-0.06929	-0.10860	4.15432	-0.01004	-0.06042
1.61934	-0.06387	-0.10349	4.21932	-0.01132	-0.06196
1.68434	-0.05902	-0.09896	4.29955	-0.01160	-0.06247
1.74934	-0.05458	-0.09483	4.43278	-0.00977	-0.06090
1.81434	-0.05037	-0.09095	4.60377	-0.00803	-0.05948
1.87934	-0.04655	-0.08745	4.77477	-0.00726	-0.05906
1.94434	-0.04319	-0.08441	4.94576	-0.00666	-0.05879
2.00934	-0.04013	-0.08169	5.11676	-0.00619	-0.05861
2.07434	-0.03741	-0.07929	5.28775	-0.00578	-0.05848
2.13934	-0.03494	-0.07715	5.45874	-0.00543	-0.05839
2.20434	-0.03269	-0.07524	5.62973	-0.00512	-0.05831
2.26934	-0.03068	-0.07356	5.80073	-0.00485	-0.05826
2.22323	-0.02901	-0.07223	5.97172	-0.00461	-0.05822
2.39934	-0.02768	-0.07124	6.14271	-0.00440	-0.05819
2.46434	-0.02636	-0.07025	6.31370	-0.00421	-0.05816
2.52934	-0.02481	-0.06901	6.48470	-0.00403	-0.05814
2.59434	-0.02308	-0.06758	6.65569	-0.00388	-0.05813
2.65934	-0.02155	-0.06634	6.82668	-0.00374	-0.05812
2.72433	-0.02018	-0.06526	6.99768	-0.00361	-0.05811
2.78934	-0.01917	-0.06455	7.16867	-0.00350	-0.05810
2.85434	-0.01849	-0.06418	7.33966	-0.00340	-0.05809
2.91934	-0.01774	-0.06372	7.51066	-0.00330	-0.05809
2.98434	-0.01696	-0.06321	7.68165	-0.00322	-0.05808
3.04933	-0.01630	-0.06284	7.83356	-0.00315	-0.05808
3.11433	-0.01606	-0.06289	8.04996	-0.00307	-0.05808
3.17933	-0.01614	-0.06327	8.42496	-0.00295	-0.05807
3.24433	-0.01632	-0.06374	8.97496	-0.00284	-0.05807
3.30933	-0.01638	-0.06409	9.79997	-0.00277	-0.05806
3.37433	-0.01577	-0.06372	11.04996	-0.00294	-0.05808
3.43933	-0.01484	-0.06300	12.92496	-0.00295	-0.05713
3.50433	-0.01383	-0.06220			

Table 6. Douglas Neumann Pressure Distribution

Model: DTNSRDC Nose

 $C_p(U-B)$ - Unblocked case $C_p(B)$ - With blockage (2.0-in. diameter model in 12.0-in. diameter tunnel)

$\frac{S}{D}$	$C_p(U-B)$	$C_p(B)$	$\frac{S}{D}$	$C_p(U-B)$	$C_p(B)$
0.00000	0.98951	0.98924	0.61089	-0.49967	-0.54559
0.11250	0.91834	0.91621	0.62903	-0.48591	-0.53167
0.16250	0.84382	0.83971	0.64773	-0.47246	-0.51808
0.18750	0.78294	0.77721	0.66699	-0.45756	-0.50299
0.21250	0.68969	0.68146	0.68676	-0.44211	-0.48735
0.23250	0.56630	0.55474	0.70704	-0.42608	-0.47109
0.24750	0.39739	0.38127	0.72782	-0.40790	-0.45262
0.25666	0.18783	0.16606	0.74905	-0.38725	-0.43159
0.25915	0.07500	0.05019	0.77071	-0.36383	-0.40771
0.26068	-0.00894	-0.03602	0.79277	-0.33344	-0.37661
0.26230	-0.06702	-0.09567	0.81797	-0.28574	-0.32767
0.26437	-0.13921	-0.16983	0.86371	-0.21908	-0.25932
0.26688	-0.22754	-0.26055	0.96662	-0.15135	-0.19036
0.26985	-0.31616	-0.35160	1.16612	-0.09328	-0.13210
0.27330	-0.40690	-0.44483	1.42261	-0.06042	-0.10013
0.27724	-0.50197	-0.54252	1.67910	-0.04304	-0.08402
0.28173	-0.58774	-0.63069	1.93559	-0.03243	-0.07475
0.28680	-0.66507	-0.71021	2.19208	-0.02542	-0.06908
0.29252	-0.72986	-0.77686	2.44857	-0.02053	-0.06546
0.29896	-0.78040	-0.82891	2.70506	-0.01696	-0.06309
0.30622	-0.81435	-0.86393	2.96155	-0.01429	-0.06151
0.31438	-0.83136	-0.88158	3.28216	-0.01178	-0.06022
0.32358	-0.83628	-0.88684	3.66689	-0.00960	-0.05931
0.33391	-0.82911	-0.87970	3.98751	-0.00825	-0.05886
0.34553	-0.81259	-0.86295	4.30812	-0.00718	-0.05857
0.35856	-0.79078	-0.84081	4.69285	-0.00619	-0.05836
0.37313	-0.76460	-0.81419	5.01346	-0.00554	-0.05825
0.38939	-0.73598	-0.78508	5.33407	-0.00500	-0.05818
0.40747	-0.70588	-0.75446	5.71880	-0.00448	-0.05813
0.42476	-0.68074	-0.72893	6.03941	-0.00412	-0.05810
0.43806	-0.66179	-0.70969	6.36002	-0.00383	-0.05809
0.44936	-0.64694	-0.69460	6.74476	-0.00354	-0.05808
0.46119	-0.63342	-0.68090	7.06537	-0.00334	-0.05807
0.47358	-0.61883	-0.66610	7.30439	-0.00322	-0.05806
0.48652	-0.60469	-0.65176	7.54017	-0.00311	-0.05806
0.50004	-0.59106	-0.63796	7.79017	-0.00301	-0.05806
0.51412	-0.57834	-0.62510	8.06516	-0.00292	-0.05805
0.52879	-0.56481	-0.61141	8.44016	-0.00283	-0.05805
0.54404	-0.55157	-0.59801	8.99016	-0.00274	-0.05805
0.55989	-0.53924	-0.58556	9.81517	-0.00270	-0.05805
0.57630	-0.52570	-0.57188	11.06516	-0.00289	-0.05806
0.59330	-0.51264	-0.55868	12.94016	-0.00292	-0.05711

Table 7. Measured Pressure Distribution

Model: 2.0-in. Diameter Hemispherical Nose

 $U_\infty = 20.0$ fps

$\frac{X}{D}$	C_P	S_d^*	$\overline{S_d}(\%)^{**}$
0.000	1.000	0.000	0.000
0.280	-0.621	0.002	0.331
0.335	-0.737	0.004	0.604
0.390	-0.776	0.005	0.586
0.430	-0.725	0.004	0.521
0.465	-0.639	0.004	0.560
0.480	-0.621	0.005	0.725
0.500	-0.605	0.004	0.581
0.515	-0.602	0.005	0.755
0.530	-0.594	0.005	0.780
0.545	-0.598	0.004	0.663
0.560	-0.588	0.004	0.613
0.575	-0.496	0.002	0.465
0.625	-0.178	0.001	0.561
0.675	-0.197	0.002	0.781
0.725	-0.178	0.001	0.561
0.775	-0.164	0.000	0.116
0.825	-0.149	0.001	0.764

* Standard deviation

** Relative standard deviation

Table 8. Measured Pressure Distribution

Model: 2.0-in. Diameter Hemispherical Nose

 $U_\infty = 30.0$ fps

$\frac{x}{D}$	C_p	S_d^*	$\overline{S_d}(\%)^{**}$
0.000	1.000	0.000	0.000
0.280	-0.622	0.001	0.179
0.335	-0.739	0.004	0.541
0.390	-0.782	0.003	0.358
0.430	-0.741	0.003	0.338
0.465	-0.653	0.002	0.349
0.480	-0.635	0.002	0.321
0.500	-0.616	0.001	0.227
0.515	-0.614	0.001	0.252
0.530	-0.606	0.003	0.495
0.545	-0.599	0.001	0.241
0.560	-0.385	0.001	0.199
0.575	-0.216	0.001	0.302
0.625	-0.231	0.001	0.436
0.675	-0.211	0.001	0.606
0.725	-0.185	0.001	0.274
0.775	-0.167	0.001	0.633
0.825	-0.149	0.001	0.459

* Standard deviation

** Relative standard deviation

Table 9. Measured Pressure Distribution

Model: 2.0-in. Diameter Hemispherical Nose

 $U_\infty = 40.0$ fps

$\frac{X}{D}$	C_p	S_d^*	$\overline{S_d}(\%)^{**}$
0.000	1.000	0.000	0.000
0.280	-0.623	0.001	0.126
0.335	-0.740	0.001	0.119
0.390	-0.788	0.001	0.100
0.430	-0.749	0.002	0.221
0.465	-0.662	0.001	0.133
0.480	-0.641	0.001	0.175
0.500	-0.621	0.001	0.182
0.515	-0.618	0.001	0.179
0.530	-0.608	0.001	0.156
0.545	-0.459	0.002	0.326
0.560	-0.226	0.001	0.300
0.575	-0.249	0.001	0.481
0.625	-0.243	0.001	0.247
0.675	-0.213	0.001	0.353
0.725	-0.185	0.001	0.329
0.775	-0.165	0.000	0.299
0.825	-0.147	0.000	0.274

^{*}Standard deviation^{**}Relative standard deviation

Table 10. Measured Pressure Distribution

Model: 2.0-in. Diameter Hemispherical Nose

 $U_\infty = 50.0$ fps

$\frac{X}{D}$	C_P	S_d^*	$\overline{S_d}(\%)^{**}$
0.000	1.000	0.000	0.000
0.280	-0.616	0.002	0.267
0.335	-0.733	0.002	0.299
0.390	-0.782	0.002	0.205
0.430	-0.747	0.002	0.214
0.465	-0.663	0.002	0.262
0.480	-0.642	0.002	0.253
0.500	-0.619	0.001	0.229
0.515	-0.616	0.001	0.194
0.530	-0.583	0.001	0.229
0.545	-0.307	0.001	0.399
0.560	-0.240	0.001	0.357
0.575	-0.270	0.001	0.192
0.625	-0.245	0.001	0.220
0.675	-0.211	0.000	0.202
0.725	-0.181	0.000	0.231
0.775	-0.161	0.001	0.322
0.825	-0.143	0.000	0.308

*Standard deviation

**Relative standard deviation

Table 11. Measured Pressure Distribution

Model: 2.0-in. Diameter Hemispherical Nose

 $U_\infty = 60.0$ fps

$\frac{X}{D}$	C_p	S_d^*	$\overline{S_d}(\%)^{**}$
0.000	1.000	0.000	0.000
0.280	-0.611	0.001	0.192
0.335	-0.730	0.001	0.151
0.390	-0.780	0.001	0.164
0.430	-0.748	0.002	0.211
0.465	-0.663	0.001	0.189
0.480	-0.641	0.001	0.193
0.500	-0.619	0.001	0.092
0.515	-0.615	0.001	0.187
0.530	-0.512	0.003	0.504
0.545	-0.268	0.001	0.287
0.560	-0.264	0.001	0.266
0.575	-0.279	0.001	0.237
0.625	-0.244	0.001	0.251
0.675	-0.208	0.000	0.097
0.725	-0.179	0.000	0.155
0.775	-0.159	0.000	0.117
0.825	-0.140	0.000	0.258

*Standard deviation

**Relative standard deviation

Table 12. Measured Pressure Distribution

Model: 2.0-in. Diameter Hemispherical Nose

 $U_\infty = 70.0$ fps

$\frac{x}{D}$	C_p	s_d^*	$\bar{s}_d(\%)^{**}$
0.000	1.000	0.000	0.000
0.280	-0.608	0.000	0.062
0.335	-0.727	0.001	0.156
0.390	-0.779	0.001	0.122
0.430	-0.749	0.001	0.116
0.465	-0.667	0.001	0.166
0.480	-0.642	0.001	0.195
0.500	-0.618	0.001	0.169
0.515	-0.612	0.001	0.18?
0.530	-0.408	0.003	0.670
0.545	-0.279	0.001	0.408
0.560	-0.279	0.001	0.238
0.575	-0.283	0.001	0.260
0.625	-0.243	0.000	0.155
0.675	-0.204	0.000	0.223
0.725	-0.175	0.000	0.158
0.775	-0.156	0.000	0.177
0.825	-0.138	0.000	0.148

* Standard deviation

** Relative standard deviation

Table 13. Measured Pressure Distribution

Model: 2.0-in. Diameter Hemispherical Nose With Boundary Layer Trip

 $U_\infty = 30.0$ fps

$\frac{X}{D}$	C_p	S_d^*	$\overline{S_d}(\%)^{**}$
0.000	1.000	0.000	0.000
0.280	-0.621	0.001	0.116
0.335	-0.737	0.001	0.113
0.390	-0.786	0.004	0.491
0.430	-0.740	0.001	0.097
0.465	-0.662	0.001	0.199
0.480	-0.642	0.004	0.659
0.500	-0.617	0.002	0.167
0.515	-0.607	0.002	0.370
0.530	-0.539	0.001	0.256
0.545	-0.441	0.002	0.352
0.560	-0.305	0.001	0.407
0.575	-0.221	0.001	0.290
0.625	-0.252	0.002	0.652
0.675	-0.218	0.001	0.416
0.725	-0.188	0.001	0.545
0.775	-0.169	0.000	0.143
0.825	-0.151	0.001	0.429

* Standard deviation

** Relative standard deviation

Table 14. Measured Pressure Distribution

Model: 2.0-in. Diameter Hemispherical Nose With Boundary Layer Trip

 $U_\infty = 40.0 \text{ fps}$

$\frac{x}{D}$	C_p	s_d^*	$\bar{s}_d(\%)^{**}$
0.000	1.000	0.000	0.000
0.280	-0.622	0.002	0.398
0.335	-0.739	0.001	0.201
0.390	-0.794	0.002	0.204
0.430	-0.766	0.002	0.216
0.465	-0.685	0.001	0.215
0.480	-0.632	0.001	0.142
0.500	-0.539	0.001	0.148
0.515	-0.483	0.001	0.178
0.530	-0.426	0.001	0.274
0.545	-0.384	0.001	0.287
0.560	-0.349	0.001	0.203
0.575	-0.322	0.001	0.303
0.625	-0.266	0.001	0.269
0.675	-0.224	0.001	0.247
0.725	-0.191	0.002	1.233
0.775	-0.169	0.001	0.328
0.825	-0.150	0.001	0.440

*Standard deviation

**Relative standard deviation

Table 15. Limited Cavitation Data

U_{∞} (fps)	Type:	Bubble-Ring			Band			Transient					
		σ_d	σ_d (Avg.)	S_d	$\overline{S_d}(\%)$	σ_d	σ_d (Avg.)	S_d	$\overline{S_d}(\%)$	σ_d	σ_d (Avg.)	S_d	$\overline{S_d}(\%)$
70.0	0.632	0.632	0.000	0.00	0.612	0.611	0.001	0.23	N.O.	—	—	—	—
	0.632	0.632	0.000	0.00	0.612	0.612	0.001	0.23	N.O.	—	—	—	—
	0.632	0.632	0.002	0.28	0.608	0.607	0.001	0.20	N.O.	—	—	—	—
60.0	0.632	0.630	0.002	0.28	0.608	0.607	0.001	0.20	N.O.	—	—	—	—
	0.631	0.631	0.002	0.28	0.608	0.607	0.001	0.20	N.O.	—	—	—	—
	0.628	0.628	0.002	0.28	0.608	0.607	0.001	0.20	N.O.	—	—	—	—
50.0	0.622	0.622	0.001	0.13	0.601	0.603	0.001	0.20	N.O.	—	—	—	—
	0.623	0.623	0.001	0.13	0.601	0.603	0.001	0.20	N.O.	—	—	—	—
	0.621	0.621	0.001	0.13	0.601	0.604	0.001	0.20	N.O.	—	—	—	—
40.0	0.622	0.616	0.005	0.73	0.592	0.593	0.001	0.21	0.635	0.644	0.009	1.32	0.652
	0.616	0.616	0.005	0.73	0.595	0.595	0.001	0.21	0.635	0.644	0.009	1.32	0.652
	0.611	0.611	0.005	0.73	0.593	0.593	0.001	0.21	0.635	0.644	0.009	1.32	0.652
30.0	N.O.*	—	—	—	0.584	0.582	0.002	0.29	0.652	0.682	0.030	4.33	0.711
	—	—	—	—	0.580	0.583	0.002	0.29	0.652	0.682	0.030	4.33	0.711
	—	—	—	—	0.562	0.561	0.001	0.18	0.787	0.757	0.034	4.47	0.775
20.0	N.O.	—	—	—	0.560	0.560	0.001	0.18	0.787	0.757	0.034	4.47	0.710
	—	—	—	—	0.560	0.560	0.001	0.18	0.787	0.757	0.034	4.47	0.710
	—	—	—	—	0.560	0.560	0.001	0.18	0.787	0.757	0.034	4.47	0.710

* None Observed

Table 16. Limited Cavitation Data

Hemispherical Nose ($\alpha = 11.0$ ppm, Temp. = 79°F)

U_{∞} (fps)	Type: Bubble-Ring			Band			Transient					
	σ_d	σ_d (Avg.)	S_d	$\overline{S_d}(\%)$	σ_d	σ_d (Avg.)	S_d	$\overline{S_d}(\%)$	σ_d	σ_d (Avg.)	S_d	$\overline{S_d}(\%)$
70.0	0.625	0.629	0.003	0.48	0.611	0.610	0.002	0.28	N.O.	—	—	—
	0.629	—	—	—	0.608	—	—	—	—	—	—	—
	0.632	—	—	—	0.612	—	—	—	—	—	—	—
60.0	0.627	0.627	0.000	0.00	0.606	0.606	0.002	0.34	N.O.	—	—	—
	0.627	—	—	—	0.608	—	—	—	—	—	—	—
	0.627	—	—	—	0.603	—	—	—	—	—	—	—
50.0	0.628	0.624	0.006	0.95	0.600	0.600	0.002	0.27	0.656	0.651	0.004	0.61
	0.616	—	—	—	0.598	—	—	—	0.651	—	—	—
	0.629	—	—	—	0.602	—	—	—	0.646	—	—	—
40.0	0.610	0.610	0.002	0.34	0.594	0.591	0.004	0.60	0.740	0.715	0.018	2.57
	0.612	—	—	—	0.586	—	—	—	0.710	—	—	—
	0.607	—	—	—	0.593	—	—	—	0.696	—	—	—
30.0	N.O.*	—	—	—	0.587	0.581	0.006	1.04	0.765	0.789	0.024	3.04
	—	—	—	—	0.584	—	—	—	0.813	—	—	—
	—	—	—	—	0.573	—	—	—	—	—	—	—
20.0	N.O.	—	—	—	N.O.	—	—	—	—	—	—	—
	—	—	—	—	—	—	—	—	—	—	—	—
	—	—	—	—	—	—	—	—	—	—	—	—

* None Observed

Table 17. Limited Cavitation Data
DTNSRDC Nose ($\alpha = 3.0$ ppm, Temp. = 79°F)

U (fps)	Type: Developed				Fixed-Patch			
	σ_d	σ_d (Avg.)	S_d	$\overline{S_d}(\%)$	σ_d	σ_d (Avg.)	S_d	$\overline{S_d}(\%)$
70.0	0.532	0.528	0.003	0.59	0.677	0.683	0.022	3.23
	0.525				0.713			
	0.526				0.660			
60.0	0.491	0.486	0.005	1.05	0.656	0.664	0.016	2.44
	0.479				0.650			
	0.488				0.687			
50.0	0.454	0.453	0.004	0.93	0.637	0.613	0.032	6.08
	0.457				0.641			
	0.447				0.560			
40.0	0.284	0.339	0.045	13.23	0.511	0.503	0.035	6.98
	0.340				0.457			
	0.394				0.542			
30.0	0.346	0.336	0.008	2.26	0.416	0.467	0.041	8.75
	0.328				0.516			
	0.333				0.468			
25.0	0.302	0.313	0.008	2.65	N.O.*	—	—	—
	0.315							
	0.322							

* None Observed

Table 17 (Continued). Limited Cavitation Data
 DTNSRDC Nose ($\alpha = 3.0$ ppm, Temp. = 79°F)

U_∞ (fps)	σ_d	Type: Band		Transient			
		σ_d (Avg.)	S_d	\bar{S}_d (%)	σ_d	σ_d (Avg.)	S_d
70.0	N.O.	—	—	—	N.O.	—	—
60.0	N.O.	—	—	—	N.O.	—	—
50.0	N.O.	—	—	—	N.O.	—	—
40.0	N.O.	—	—	—	0.627 0.640	0.634	0.007 1.03
30.0	0.329 0.343	0.336	0.007	2.08	0.725 0.725	0.688	0.038 5.45
25.0	0.340 0.331	0.337	0.004	1.26	0.645 0.679	0.662	0.017 2.57

Table 18. Limited Cavitation Data
 DTNSRDC Nose ($\alpha = 8.0$ ppm, Temp. = 79°F)

U_{∞} (fps)	Type: Developed			Fixed-Patch				
	σ_d	σ_d (Avg.)	S_d	$\overline{S_d}(\%)$	σ_d	σ_d (Avg.)	S_d	$\overline{S_d}(\%)$
70.0	No data	—	—	—	0.564	0.560	0.007	1.27
					0.550			
					0.566			
60.0	0.489	0.493	0.004	0.75	0.558	0.550	0.007	1.27
	0.493				0.551			
	0.498				0.541			
50.0	0.454	0.454	0.002	0.45	0.514	0.522	0.007	1.25
	0.452				0.523			
	0.457				0.530			
40.0	0.432	0.429	0.003	0.79	N.O.*	—	—	—
	0.430							
	0.424							
30.0	0.344	0.362	0.013	3.55	N.O.	—	—	—
	0.373							
	0.369							
25.0	0.300	0.297	0.005	1.77	N.O.	—	—	—
	0.290							
	0.302							

*None Observed

Table 18 (Continued). Limited Cavitation Data
 DTNSRDC Nose ($\alpha = 8.0$ ppm, Temp. = 79°F)

U_{∞} (fps)	σ_d	σ_d (Avg.)	S_d	$\overline{S_d}$ (%)	Transient			
					σ_d	σ_d (Avg.)	S_d	$\overline{S_d}$ (%)
70.0	N.O.	—	—	—	0.625 0.597 0.591	0.604	0.015	2.45
60.0	N.O.	—	—	—	0.600 0.606 0.611	0.606	0.005	0.74
50.0	N.O.	—	—	—	0.683 0.709 0.717	0.703	0.015	2.07
40.0	N.O.	—	—	—	0.700 0.750 0.775	0.742	0.031	4.20
30.0	N.O.	—	—	—	0.730 0.760	0.745	0.015	2.01
25.0	0.325 0.310 0.300	0.312	0.010	3.30	0.709 0.756 0.803	0.047	6.22	

Schliebe Nose ($\alpha = 3.0$ ppm, Temp. = 78°F)

U_{∞} (fps)	Type:	Developed			Fixed-Patch			Transient			
		σ_d	σ_d (Avg.)	S_d	$\overline{S_d}(\%)$	σ_d	σ_d (Avg.)	S_d	$\overline{S_d}(\%)$	σ_d	σ_d (Avg.)
70.0	0.346	0.345	0.005	1.30	0.437	0.449	0.010	2.27	N.O.	—	—
	0.350	—	—	—	0.462	—	—	—	—	—	—
	0.339	—	—	—	0.449	—	—	—	—	—	—
60.0	0.339	0.322	0.018	5.44	0.452	0.420	0.040	9.46	N.O.	—	—
	0.304	—	—	—	0.444	—	—	—	—	—	—
	—	—	—	—	0.364	—	—	—	—	—	—
50.0	0.296	0.298	0.002	0.67	0.338	0.352	0.010	2.88	0.484	0.462	0.021
	0.300	—	—	—	0.359	—	—	—	0.469	—	4.63
	—	—	—	—	0.360	—	—	—	0.433	—	—
40.0	0.286	0.281	0.004	1.27	N.O.*	—	—	—	0.517	0.542	0.061
	0.279	—	—	—	—	—	—	—	0.625	—	11.18
	0.278	—	—	—	—	—	—	—	0.483	—	—
30.0	0.251	0.253	0.002	0.93	N.O.	—	—	—	0.518	0.497	0.022
	0.251	—	—	—	—	—	—	—	0.475	—	4.33
	0.256	—	—	—	—	—	—	—	—	—	—

* None Observed

Table 20. Limited Cavitation Data

Schiebe Nose ($\alpha = 9.0$ ppm, Temp. = 78°F)

U_{∞} (fps)	Type: Developed			Fixed-Patch			Transient					
	σ_d	σ_d (Avg.)	S_d	$\overline{S_d}(\%)$	σ_d	σ_d (Avg.)	S_d	$\overline{S_d}(\%)$	σ_d	σ_d (Avg.)	S_d	$\overline{S_d}(\%)$
70.0	0.351	0.346	0.004	1.03	0.386	0.389	0.004	0.97	0.495	0.498	0.005	1.08
	0.344				0.386				0.507			
	0.343				0.394				0.495			
60.0	0.310	0.321	0.008	2.51	N.O.*	—	—	—	0.469	0.480	0.012	2.54
	0.329								0.497			
	0.324								0.474			
50.0	0.306	0.300	0.005	1.81	N.O.	—	—	—	0.588	0.607	0.022	4.42
	0.293								0.653			
	0.302								0.599			
40.0	0.272	0.278	0.004	1.51	N.O.	—	—	—	0.630	0.621	0.010	1.67
	0.279								0.628			
	0.282								0.607			
30.0	0.251	0.250	0.002	0.76	N.O.	—	—	—	0.540	0.604	0.047	7.75
	0.251								0.620			
	0.247								0.651			

* None Observed

DISTRIBUTION LIST FOR UNCLASSIFIED TM 81-60, by J. A. Carroll, dated
13 February 1981.

Commander
Naval Sea Systems Command
Department of the Navy
Washington, DC 20362
Attn: Library
Code NSEA-09G32
(Copy Nos. 1 and 2)

Naval Sea Systems Command
Attn: T. E. Peirce
Code NSEA-63R3
(Copy No. 3)

Naval Sea Systems Command
Attn: A. R. Paladino
Code NSEA-05H1
(Copy No. 4)

Naval Sea Systems Command
Attn: F. B. Peterson
Code NSEA-52P
(Copy No. 5)

Commander
David W. Taylor Naval Ship R&D Center
Department of the Navy
Bethesda, MD 20084
Attn: Library
Code 522
(Copy No. 6)

David W. Taylor Naval Ship R&D Center
Attn: T. E. Brockett
Code 1544
(Copy No. 7)

David W. Taylor Naval Ship R&D Center
Attn: W. B. Morgan
Code 154
(Copy No. 8)

David W. Taylor Naval Ship R&D Center
Attn: M. M. Sevik
Code 19
(Copy No. 9)

David W. Taylor Naval Ship R&D Center
Attn: J. H. McCarthy
Code 154
(Copy No. 10)

David W. Taylor Naval Ship R&D Center
Attn: T. T. Huang
Code 1552
(Copy No. 11)

Commanding Officer
Naval Underwater Systems Center
Newport, RI 02840
Attn: Library
Code 54
(Copy No. 12)

Commanding Officer
Naval Ocean Systems Center
San Diego, CA 92152
Attn: Library
(Copy No. 13)

Commander
Naval Surface Weapons Center
Silver Spring, MD 20910
Attn: Library
(Copy No. 14)

Naval Surface Weapons Center
Attn: J. L. Baldwin
Code WA-42
(Copy No. 15)

Naval Surface Weapons Center
Attn: C. W. Smith
(Copy No. 16)

Defense Technical Information Center
5010 Duke Street
Cameron Station
Alexandria, VA 22314
(Copy Nos. 17 through 22)

Naval Research Laboratory
Washington, DC 20390
Attn: Library
(Copy No. 23)

Office of Naval Research
Department of the Navy
800 N. Quincy Street
Arlington, VA 22217
Attn: Director
(Copy No. 24)

DISTRIBUTION LIST FOR UNCLASSIFIED TM 81-60, by J. A. Carroll, dated
13 February 1981.

Naval Postgraduate School
The Presidio
Monterey, CA 93940
Attn: Library
(Copy No. 25)

California Institute of Technology
Division of Engineering for
Applied Sciences
Pasadena, CA 91109
Attn: Dr. A. J. Acosta
(Copy No. 26)

California Institute of Technology
Attn: C. Brennen
(Copy No. 27)

California Institute of Technology
Attn: M. S. Plesset
(Copy No. 28)

F. G. Hammit
The University of Michigan
Department of Mechanical Engineering
Ann Arbor, MI 48109
(Copy No. 29)

Professor P. Leehey
Dept. of Ocean Engineering - Room 5-222
Massachusetts Institute of Technology
77 Massachusetts Avenue
Cambridge, MA 02139
(Copy No. 31)

Dr. George F. Wislicenus
351 Golf Court (Oakmont)
Santa Rosa, CA 95405
(Copy No. 31)

Dr. R. E. A. Arndt
St. Anthony Falls Hydraulic Laboratory
University of Minnesota
Mississippi River at 3rd Ave., S.E.
Minneapolis, MN 55414
(Copy No. 32)

Iowa Institute of Hydraulic Research
The University of Iowa
Iowa City, Iowa 52240
Attn: Director
(Copy No. 33)

Dr. C. S. Martin
Professor of Civil Engineering
Georgia Institute of Technology
Atlanta, GA 30332
(Copy No. 34)

Netherlands Ship Model Basin
Haagsteeg 2
P. O. Box 28
67 AA Wageningen
The Netherlands
Attn: J. van der Meulen
(Copy No. 35)

Netherlands Ship Model Basin
Attn: G. Kuiper
(Copy No. 36)

Carl-Anders Johnsson
Statens Skeppsprovningsanstalt
Box 24001
S-400 22 Goteborg
Sweden
(Copy No. 37)

HSVA GmbH
Bramfelder Strasse 164
200 Hamburg 60
Postfach 600 929
Federal Republic of Germany
Attn: Dr. E. Weitendorf
(Copy No. 38)

Director
Forschungsbeauftragter für Hydroakustik
8012 Ottobrunn B Munchen
Waldbarkstr. 41
Munich
Germany
(Copy No. 39)

Institute of High Speed Mechanics
Tohoku University
Sendai
Japan
Attn: Director
(Copy No. 40)

Dr. V. H. Arakeri
Department of Mechanical Engineering
Indian Institute of Science
Bangalore 560 012
India
(Copy No. 41)

DISTRIBUTION LIST FOR UNCLASSIFIED TM 81-60, by J. A. Carroll, dated
13 February 1981.

Jack Hoyt
Naval Undersea R & D Center
Pasadena Annex
3203 E. Foothill Boulevard
Pasadena, CA 91109
(Copy No. 42)

J. M. Robertson
125 Talbot Laboratory
University of Illinois
Urbana, IL 61801
(Copy No. 43)

Robert Waid
Lockheed Aircraft Corp.
Division No. 81-73, Bldg. 538
P. O. Box 504
Sunnyvale, CA 94088
(Copy No. 44)

James A. Carroll
7276 Bourbon Lane
La Palma, CA 90623
(Copy No. 45)

I. S. Pearsall
Head of Fluid Mechanics Division
National Engineering Laboratory
East Kilbride
Glasgow, SCOTLAND G75 0QU
(Copy No. 46)

A. P. Keller
Lehrstuhl für Wasserbau und
Wassermengenwirtschaft
Versuchsanstalt für Wasserbau
Technische Universität München
Oskar v. Miller-Institut
D-8111 Obernach, Post Walchensee
West Germany
(Copy No. 47)

S. P. Hutton
Dept. of Mechanical Engineering
The University
Southampton, SO9, 5NH
England
(Copy No. 48)

T. Sasajima
Resistance and Propulsion Research Lab
Nagasaki Tech. Inst.
Mitshubishi Heavy Ind., Ltd.
1-1 Akunoura-Machi
Nagasaki 950-91
JAPAN
(Copy No. 49)

Y. Kodama
Ship Research Institute
Ministry of Transport
38-1, 6-chome, Shinkawa, Mitaka
Tokyo, JAPAN
(Copy No. 50)

D. M. Oldenziel
Delft Hydraulics Laboratory
P. O. Box 177
2600 MH Delft
The Netherlands
(Copy No. 51)

The Pennsylvania State University
Applied Research Laboratory
Post Office Box 30
State College, PA 16801
Attn: GTWT Files
(Copy No. 52)

Applied Research Laboratory
Attn: J. W. Holl
(Copy Nos. 53 through 56)

Applied Research Laboratory
Attn: M. L. Billet
(Copy No. 57)

Applied Research Laboratory
Attn: D. R. Stinebring
(Copy No. 58)

Applied Research Laboratory
Attn: R. S. Moyer
(Copy No. 59)

Applied Research Laboratory
Attn: A. L. Treaster
(Copy No. 60)

Applied Research Laboratory
Attn: B. R. Parkin
(Copy No. 61)

Applied Research Laboratory
Attn: R. E. Henderson
(Copy No. 62)

Applied Research Laboratory
Attn: W. S. Gearhart
(Copy No. 63)

DISTRIBUTION LIST FOR UNCLASSIFIED TM 81-60, by J. A. Carroll, dated
13 February 1981.

Applied Research Laboratory
Attn: D. E. Thompson
(Copy No. 64)

Applied Research Laboratory
Attn: M. T. Pigott
(Copy No. 65)